Opto-thermal Energy Transport with Selective Metamaterials and Solar Thermal Characterization of Selective Metafilm Absorbers

by

Hassan Alshehri

A Dissertation Presented in Partial Fulfillment
of the Requirements for the Degree
Doctor of Philosophy

Approved June 2018 by the
Graduate Supervisory Committee:

Liping Wang, Chair
Patrick Phelan
Konrad Rykaczewski
Robert Wang
Hongbin Yu

ARIZONA STATE UNIVERSITY

August 2018

ABSTRACT

The objective of this dissertation is to study the use of metamaterials as narrow-band and broadband selective absorbers for opto-thermal and solar thermal energy conversion. Narrow-band selective absorbers have applications such as plasmonic sensing and cancer treatment, while one of the main applications of selective metamaterials with broadband absorption is efficiently converting solar energy into heat as solar absorbers.

This dissertation first discusses the use of gold nanowires as narrow-band selective metamaterial absorbers. An investigation into plasmonic localized heating indicated that film-coupled gold nanoparticles exhibit tunable selective absorption based on the size of the nanoparticles. By using anodized aluminum oxide templates, aluminum nanodisc narrow-band absorbers were fabricated. A metrology instrument to measure the reflectance and transmittance of micro-scale samples was also developed and used to measure the reflectance of the aluminum nanodisc absorbers (220 μm diameter area). Tuning of the resonance wavelengths of these absorbers can be achieved through changing their geometry. Broadband absorption can be achieved by using a combination of geometries for these metamaterials which would facilitate their use as solar absorbers.

Recently, solar energy harvesting has become a topic of considerable research investigation due to it being an environmentally conscious alternative to fossil fuels. The next section discusses the steady-state temperature measurement of a lab-scale multilayer solar absorber, named metafilm. A lab-scale experimental setup is developed to characterize the solar thermal performance of selective solar absorbers. Under a concentration factor of 20.3 suns, a steady-state temperature of ~500^{o}C was achieved for the metafilm compared to 375^{o}C for a commercial black absorber under the same

conditions. Thermal durability testing showed that the metafilm could withstand up to 700^{o}C in vacuum conditions and up to 400^{o}C in atmospheric conditions with little degradation of its optical and radiative properties. Moreover, cost analysis of the metafilm found it to cost significantly less ($2.22 per m^2) than commercial solar coatings ($5.41-100 per m^2).

Finally, this dissertation concludes with recommendations for further studies like using these selective metamaterials and metafilms as absorbers and emitters and using the aluminum nanodiscs on glass as selective filters for photovoltaic cells to enhance solar thermophotovoltaic energy conversion.

ACKNOWLEDGMENTS

It would not have been possible to write this doctoral thesis without the help and support of the kind people around me, to only some of whom it is possible to give particular mention here.

This thesis would not have been possible without the help, support, and patience of my PhD advisor and chairman of my committee, Prof. Liping Wang. The good advice and support of my committee members, Profs. Patrick Phelan, Konrad Rykaczewski, Robert Wang, and Hongbin Yu, has been invaluable, for which I am extremely grateful.

I would not have been able to pursue a career in academia if it weren't for the valuable advice of my parents and close family members who supported me in whatever career I chose but also encouraged me to pursue an academic career.

I would also like to thank my colleagues and friends at Arizona State University for their support and friendship. We had many fruitful discussions both academically and on a personal level. I would especially like to thank Dr. Hao Wang, Dr. Yue Yang, Dr. Ray Chang, Sydney Taylor, Payam Sabbaghi, Xiaoyan Ying, Dr. Linshuang Long, Dr. Qing Ni, Ryan McBurney, Dr. Sami Alelyani, Turki Alajmi, Dr. Abdullah Almajed, Faisal Alfaisal, and Dr. Fraaz Tahir.

Finally, I would like to thank King Saud University and the Saudi Arabian Cultural Mission for their financial support with the Master's and PhD scholarships.

TABLE OF CONTENTS

Page

CHAPTER Page

LIST OF TABLES

Table Page

LIST OF FIGURES

Figure Page

Figure Page

CHAPTER 1 INTRODUCTION

1.1 Overview of Selective Absorbers for Solar Energy Harvesting

Renewable energy technologies, such as solar energy, are becoming increasingly important and widespread in today's world as more governments adopt these technologies as an alternative to fossil fuels. Solar energy can be harvested through one of two main methods: by using solar thermal absorbers to convert the solar energy to heat or by using solar photovoltaic cells to convert the solar energy to electricity. Solar thermal absorbers are efficient at absorbing solar energy without losing a significant amount of energy as thermal loss. This is achieved through the spectral selectivity of the absorbers. An ideal spectrally selective solar thermal absorber has unity absorptance in the solar spectrum (visible and near-infrared, NIR, range) and zero-emittance in the infrared range (IR) where most of the thermal loss occurs. Concentrating solar power (CSP) systems require solar thermal absorbers to be operated at elevated temperatures (greater than 400^{o}C [1-4]). Therefore, the solar thermal absorbers used in these systems must sustain those temperatures without damage. Thus, highly efficient solar spectrally selective absorbers with high thermal stability at elevated temperatures are necessary for high energy density CSP systems.

1.2 Metamaterials as Solar Thermal Absorbers

Spectrally selective solar thermal absorbers can be separated into two groups: natural coatings and metamaterials. Examples of natural coatings include black paint [5, 6], Pyromark 2500 [7-9], composites [10-12], and cermets [13-18]. Some of these materials possess intrinsic selective optical properties, even if they are not highly tunable. Pyromark

2500 is the most common in CSP systems which, though highly absorbing and thermally stable at elevated temperatures, still loses a significant amount of heat through emission in the IR range[8, 9]. Metamaterials (or man-made materials) have been developed as solar thermal absorbers due to their spectral tunability which allows them to approach ideal absorbers. These metamaterials are usually based on micro- or nano-structures, such as gratings [19-25], nanoparticles [26-30], photonic crystals [31-34], and multilayers [35-38].

A variety of fast and inexpensive techniques exist to apply nanoparticles (including spherical nanoparticles, nanowires, and nanodiscs) to films This can be used to achieve spectrally selective absorption making them an attractive option for large scale narrow-band absorbers or broadband solar absorbers. A layer of monodispersed nanoparticles, through self-assembly, can be applied to a film by several methods such as utilizing long-range attractive interactions or capillary forces between the nanoparticles [39-42]. Nanodiscs can also be added to films in an easy and relatively inexpensive way, through the use of an intermediate anodized aluminum oxide (AAO) layer. Multilayered films also use a variety of resonance mechanisms to achieve selective absorption based on their geometry. For example, an asymmetric Fabry-Perot has a tunable absorption enhancement that depends on the cavity thickness [43]. This work seeks to develop techniques to characterize both the radiative properties and the solar thermal performance of the aforementioned metamaterial solar absorbers.

1.3 Solar Thermal Characterization of Metamaterial Solar Absorbers

The stagnation temperature of a solar thermal collector is the steady-state temperature when there is no fluid flowing through the collector. The stagnation temperature indicates the maximum temperature an absorber can achieve, and therefore, is

a measure of its potential for solar thermal energy harvesting. In practice, the stagnation temperature mainly serves a safety purpose: the collector should be able to withstand this temperature and operators of the CSP plant need to be aware of it, especially during installation and plant shutdown times. According to Duffie and Beckman, the stagnation temperature of a single cover flat-plate collector ranges from 150^{o}C to 300^{o}C (nonselective to highly selective coatings) [44]. Standard EN12975, developed for solar thermal collector testing, includes guidelines for measuring the stagnation temperature of collectors, including flat plate collectors and evacuated tube collectors, under 1000 W/m^2 [45]. Dupeyrat *et al*. applied the standard to a flat-plate photovoltaic-thermal collector and reported a stagnation temperature of 142^{o}C [46]. Harrison and Cruickshank derived an approximation equation that can be used to estimate the stagnation temperature [47]. They found that, using the approximation equation under Standard EN12975 conditions, the stagnation temperature was 177^{o}C for mid-performance flat-plate collectors and 350^{o}C for evacuated tube collectors. Moreover, Köhl *et al.* reported modelled stagnation temperatures of a solar absorber coating for a flat-plate collector as functions of its optical properties [48]. The previous works along with the standard were mainly focused on measuring the stagnation temperature of full-sized solar collectors for safety reasons. However, a rapid method of testing small absorber samples to compare their performance under different solar concentrations has not, to the best of our knowledge, been developed.

1.4 Primary Objective of Dissertation

The primary objective of this dissertation is to study the use of metamaterials as narrow-band and broadband selective absorbers for opto-thermal and solar thermal energy conversion. The dissertation is organized as follows; Chapter 2 investigates plasmonic

localized heating in film coupled nanowire selective absorbing metamaterials. Chapter 3 discusses how spectrally selective absorbers such as nanoparticles and nanodiscs can be easily fabricated to make an absorber with selective narrow-band radiative properties. The chapter also discusses a measurement technique developed to study the reflectance and transmittance in the visible wavelength range for microscale samples. This chapter also includes the measurement results of the fabricated nanodiscs which demonstrate the narrowband selectivity of these nanoparticle-based metamaterials as well as show their broadband absorption potential. Chapter 5 presents a lab-scale measurement technique for assessing the performance of solar thermal absorbers. The final chapter of this dissertation is a summary as well as a discussion of recommendations for further studies like using these selective metamaterials and metafilms as absorbers and emitters and using the aluminum nanodiscs on glass as selective filters for photovoltaic cells to enhance solar thermophotovoltaic energy conversion.

CHAPTER 2 PLASMONIC LOCALIZED HEATING OF FILM-COUPLED GOLD NANOWIRES

2.1 Introduction to Plasmonic Localized Heating

The spot size of an optically focused light is constrained by the Abbe diffraction limit, which in turn limits the hot spot size that can be generated by the focused light or laser [49]. This hot spot is too large for some applications such as nanoscale patterning [50], photothermal therapy [51-53], and super high areal density data recording [54, 55]. However, through the excitation of plasmonic resonances in certain metamaterials, the diffraction limit can be overcome to obtain hot spots on the order of tens of nanometers. Cao *et al.* utilized the local temperature rise that results from plasmonic modes in metallic nanostructures to grow semiconductor nanowires and carbon nanotubes [56]. Sotiriou *et al.* used the localized thermal heating effect induced by the plasmonic coupling of silica coated gold and Fe_2O_3 nanoparticles to kill cancer cells [57]. The localized heating effect in the previous two applications was due to the excitation of surface plasmon resonance. Challener *et al.* proposed a method for localized heating in a heat assisted magnetic data recording system [58]. The method utilized localized surface plasmons and it efficiently enhanced data storage density. Apart from surface plasmon resonance and localized surface plasmon resonance, applying magnetic polariton (MP) to achieve plasmonic localized heating is not well understood.

The unique behavior of MP excitation has enabled it to be used in some applications such as energy harvesting [26, 59-61] and sensing [62]. Several metamaterial structures were employed to excite MP. These structures include periodic strips coupled to a metallic

film [63], slit arrays [64], and deep gratings [43]. Moreover, MP excitation has also been found and numerically investigated in film-coupled nanoparticles [26].

Exciting plasmonic resonance modes through utilizing nanowires, which can be easily applied to films, is a fast and inexpensive way of achieving spectrally tunable localized heating. A layer of monodispersed nanoparticles, through self-assembly, can be applied to a film by several methods such as utilizing long-range attractive interactions or capillary forces between the nanoparticles [39-42]. However, neither the excitation of MP between film-coupled horizontally aligned nanowire arrays nor the plasmonic localized heating through this MP excitation has been investigated extensively yet.

In this work, we investigate the optical properties of a film-coupled horizontally aligned gold nanowire (AuNW) array metamaterial as well its thermal behavior. An inductor-capacitor (*LC*) circuit model is used to predict the MP resonance wavelength and compare with the numerical results for varied geometrical parameters. Moreover, a detailed study of the local steady state and transient temperature profiles due to the resonant light absorption of MP will be presented to demonstrate plasmonic localized heating at the nanometer scale.

The structure of interest is shown in Figure 2.1 The film-coupled nanowire metamaterial structure consists of an array of horizontally aligned gold nanowires (AuNWs) that are periodically dispersed on a gold film (Au film) with an ultrathin polymer spacer in between. This structure rests on a silicon substrate which does not affect the radiative properties due to the optically opaque Au film. The AuNWs have a diameter *d* and periodicity *p*, the thickness of the gold film and the polymer spacer are *h* and *t*,

respectively. The structure is assumed to be uniform and infinitely long along the axial direction of the AuNWs.

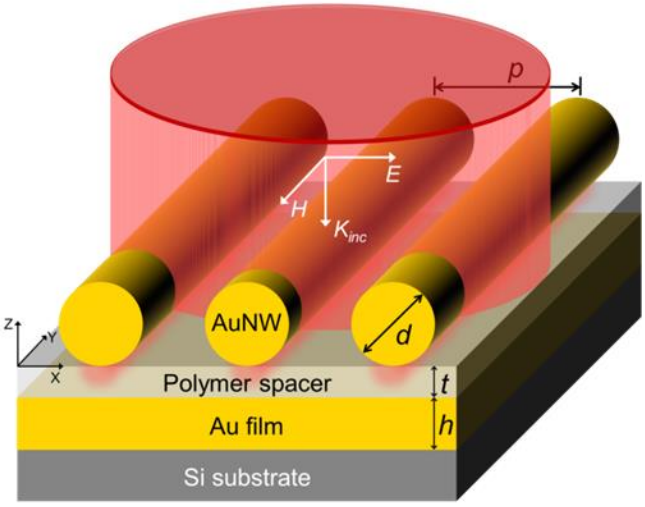

Figure 2.1 Schematic of the nanowire based metamaterial.

2.2 Radiative Properties of Film-Coupled Gold Nanowires

A continuous broadband electromagnetic plane wave was incident on the structure with a spectral range from 500 nm to 1000 nm. The plane of incidence is the plane formed by the surface normal and the incident wavevector K_{inc} and depending on the orientation of the electric and magnetic fields with respect to the plane of incidence, the wave is either called a transverse electric (TE) wave or a transverse magnetic (TM) wave. Simulation of the optical response of the structure was performed through the use of the numerical finite element based solver, High Frequency Structural Simulator (HFSS). The optical constants for gold and silicon were taken from Johnson and Christy [65], and Palik [66], respectively. For the lossless polymer spacer, the refractive index n was taken as 1.5 [67]. However, the dielectric response of a gold nanowire might vary from the bulk response as the size becomes sufficiently small to induce size effect due to boundary scattering and/or quantum

effect due to modification of the electronic band structure. The following equation from Li *et al*. can be used to estimate the modified dielectric function [68].

$$\varepsilon(\omega) = \varepsilon_{bulk}(\omega) + \frac{\omega_p^2}{\omega^2 + i\Gamma_\infty \omega} - \frac{\omega_p^2}{\omega^2 + i\Gamma(t)\omega} \tag{2.1}$$

Here, ε_{bulk} is the frequency-dependent bulk dielectric function, ω is the angular frequency of the incident light, ω_p is the plasma frequency, and Γ is the size-dependent damping constant which is equal to $\Gamma_\infty + A_0 \nu_F / t$. For gold, ω_p is $2\pi \times 2.195 \times 10^{15}$ Hz, the bulk damping constant Γ_∞ is 11×10^{13} Hz, the Fermi velocity ν_F is 1.4×10^6 m/s. The thickness of the material is t, and the constant A_0 for simple Drude theory with isotropic scattering is equal to 1.

Figure 2.2(a) shows that the real part of the dielectric function of a gold nanowire does not change significantly as the size decreases from 1000 nm to 5 nm. However, the imaginary part of the dielectric function as shown in Figure 2.2(b) changes drastically from the bulk when the nanowire size is below 100 nm. Since, in our simulations, the diameter for the gold nanowire is 250 nm, it is reasonable to use the dielectric function of bulk gold for the gold nanowires without considering the size effect on the dielectric response.

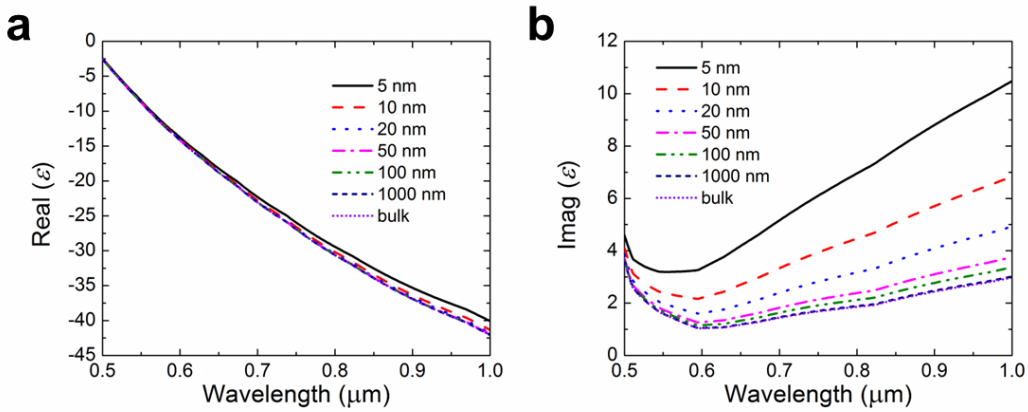

Figure 2.2. Comparison of the real and imaginary parts of the dielectric function of an Au film.

The optical behavior of the structure is now studied. When setting up the optical simulation in the HFSS, a unit cell of the structure was modeled and boundary conditions were applied to simulate the array. A master/slave periodic boundary condition was applied in the x and y directions of the simulation domain for normal incidence. Radiation boundary conditions were assigned to the top and bottom simulation domain surfaces along the y direction. HFSS solves in the frequency domain, therefore in order to simulate a broadband incident plane wave from 500 to 1000 nm, a frequency sweep was implemented from 300 to 600 THz with a spectral resolution of 5 THz in order to ensure good trade-off between simulation time and accuracy after comparing with simulations of smaller step sizes. The magnitude of the incident electric field on the structure E_0 was 1 V/m and the respective magnetic field H_0 magnitude was 0.0026 A/m. Since one of the radiation boundary conditions was set as a frequency selective surface, it was possible to use these boundary conditions to calculate the scattering parameters S11 and S21. These parameters were then used to find the spectral reflectance R and transmittance T. Reflectance was taken

as $|S11|^2$ where the subscript resembles the ratio of the reflected energy to the total incident energy on the structure. On the other hand, transmittance was equal to $|S21|^2$, which represents the ratio of the transmitted energy to the total incident energy on the structure. Furthermore, spectral absorptance was found through $A = 1 - R - T$. HFSS uses an adaptive meshing technique where it refines the mesh automatically until certain criteria are met. In our case, we used a difference in the scattering parameters no greater than 0.001 in their magnitudes as the criteria and a minimum of four converged adaptive runs to avoid false convergence. Figure 2.3 shows the spectral optical properties, namely reflectance *R*, transmittance *T*, and absorptance *A*, of the considered structure in response to TE and TM waves under normal incidence. It can be seen that the structure is basically highly reflective for TE waves at wavelengths longer than 600 nm, while a reflectance dip appears for TM waves, leading to a strong selective absorption peak around the wavelength of 750 nm. Note that, the structure is opaque for both polarizations due to the 250 nm gold film.

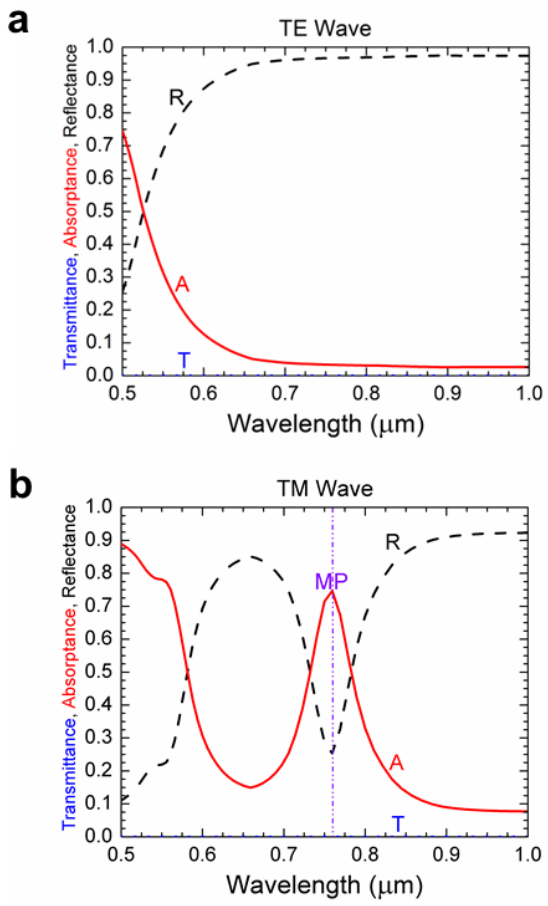

Figure 2.3. Spectral optical properties at normal incidence for (a) TE waves and (b) TM waves.

2.3 Elucidation of Magnetic Polariton Effect

To explain the underlying mechanism for the excitation of MP, the electromagnetic field distribution is presented in Figure 2.4(a) at the resonance wavelength of 760 nm. The plot is a cross-sectional view of the metamaterial structure and the axes represent the dimensions of the structure. The color of the contour indicates the strength of the normalized magnetic field $\log|H/H_0|$ inside the structure and the arrows represent the strength and direction of the electric field *E*. A red ellipse is drawn around the spacer with

the arrows showing the direction of current density *J* inside the polymer spacer between the AuNW and Au film. It can be seen from Figure 2.4(a) that the magnetic field is strongly enhanced inside the current loop and a confinement of the electromagnetic energy can also be observed. This resonance behavior only occurs in the case of TM incidence since the magnetic field must be parallel to the AuNWs in order to excite an in-plane resonant current loop within the structure. This type of magnetic response has been found and studied in other grating structures where it was determined as MP [23, 63, 69]. However, MP resonance has not been studied in film-coupled nanowires yet.

Figure 2.4(b) shows the electrical field along the top surface of the Au film. This will be used to determine parameters in the inductor- capacitor (*LC)* circuit model that will be discussed next. Since a resonance current loop is excited within the structure at MP resonance, an *LC* circuit model is used to analogize the structure to an electric circuit, as well as predict the resonance wavelength by zeroing the total impedance of the electric circuit. This model was previously used to successfully predict the MP resonance wavelength in film coupled structures consisting of 1D gratings [69] and 2D patches [24]. These structures have one feature in common: the top gratings are basically a rectangular or parallelogram shape in contrast to the nanowire structure proposed in this paper. We modified the *LC* circuit model in order to account for this difference in structure. Through this modification, the film-coupled AuNW structure can be treated as an effective film-coupled grating structure based on the electromagnetic field distribution shown in Figure 2.4. A simplified schematic view is plotted in Figure 2.5(a) to help explain the *LC* circuit model which is shown in Figure 2.5(b). The dimensions of the metamaterial structure are as follows: the AuNW radius *R* is 125 nm, the polymer spacer thickness *t* is 10 nm, and the

period *p* is 400 nm. Based on the electric field distribution as well as the material properties, the effective inductor and capacitor components in the circuit can be defined. This was accomplished through approximating the AuNW as a plate with an effective thickness h_{eff} and a gap distance d_{gap} away from the polymer spacer. The mutual inductances between the effective AuNW and Au film can be calculated from $L_{m,NW} = L_{m,film} = \mu_0 w(t + d_{gap} - 0.5h_{eff})/(2l)$, where μ_0 is the permeability of free space, w is the width of the effective plate, and l is the length of the structure in the y-direction which can be cancelled out through the calculations. Note that the effect of drifting electrons is not neglected as it contributes to the kinetic inductance for both the AuNW and the Au film, which are defined as $L_{k,NW}$ and $L_{k,film}$, respectively. The kinetic inductances can be calculated from $L_{k,NW} = L_{k,film} = -w/(\omega^2 h_{eff} l \varepsilon_0 \varepsilon'_m)$, where h_{eff} is the height of the effective plate, ω is the angular frequency of the incident light, and ε'_m is the real part of the dielectric function of gold. Moreover, the effective plate and the Au film separated by the polymer spacer can be treated as a parallel plate capacitor with capacitance $C_{spacer} = c_1 \varepsilon_{d,spacer} \varepsilon_0 wl/t$, where c_1 is a coefficient that accounts for non-uniform charge distribution at the metal surface (taken as 0.2 for our calculations [70]), and $\varepsilon_{d,spacer}$ is the dielectric function of the polymer spacer. Furthermore, capacitance due to the air gap should also be considered as $C_{gap} = c_1 \varepsilon_{d,air} \varepsilon_0 wl/(d_{gap} - 0.5h_{eff})$, where $\varepsilon_{d,air}$ is the dielectric function of air.

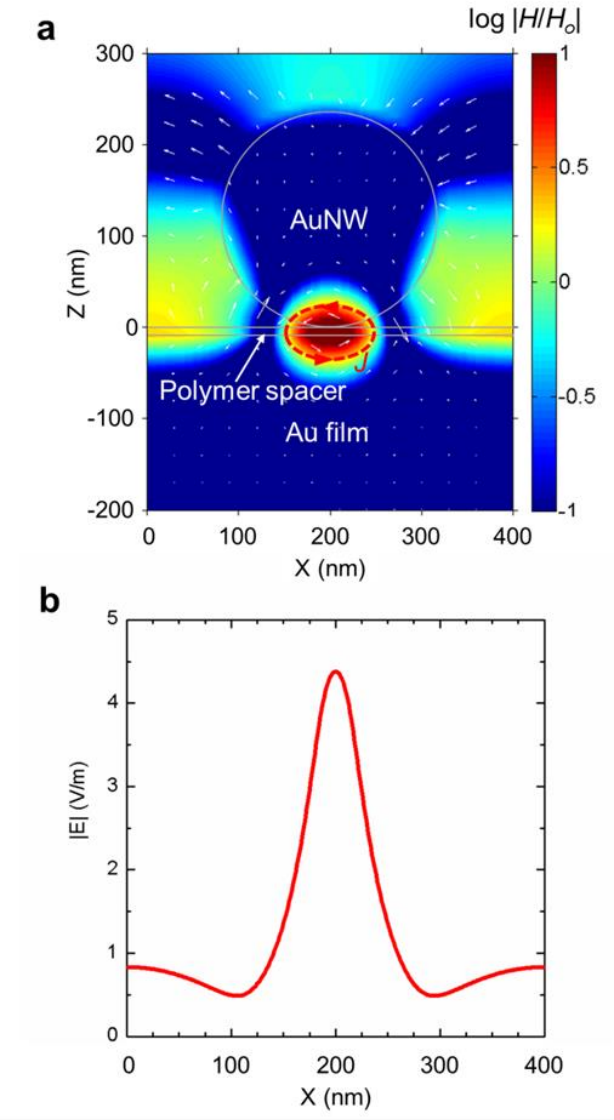

Figure 2.4. (a) Electromagnetic field distribution when MP resonance is excited at λ = 760 nm. (b) Electric field along the top surface of the Au film in the x-direction.

Determining the geometric parameters of the effective Au plate (w, d_{gap}, and h_{eff}) will now be discussed. The excited current loop at MP resonance is simplified as an ellipse. The long axis of the ellipse is $a = a_i R$, where a_i is the long axis coefficient and R is the radius of the AuNW. The short axis of the ellipse is $b = (t/2) + b_i R$, where b_i is the short axis

coefficient. The long and short axis coefficients are based on the distribution of the electric field in the structure shown in Figure 2.4(b). The long axis coefficient a_i is determined as 188/250 = 0.75, as the electric field decayed to 0 at x = 94 nm, which is the edge of the current loop. The short axis coefficient b_i is obtained based on the approximation that the current penetrates into the Au film by two penetration depths. The penetration depth $\delta = \lambda / (4\pi k)$ is found to be 13.28 nm, where k is the extinction coefficient [65]. Therefore, b_i is equal to 26.56/125 = 0.212. The effective width is determined as the distance between the two intersection points between the ellipse and circle. Next, the distance between the plate and the polymer spacer d_{gap} is found through $w = 2\sqrt{R^2 - (R - d_{gap})^2}$, which is based on the geometric relations as seen from Figure 2.5(a). Furthermore, the height of the effective plate is then found through $h_{eff} = 0.5(b_i R)$ which is equal to one penetration depth δ. By collecting the previous parameters together, the total impedance can be expressed by equation (2.2), where, C_{tot} is the total capacitance of C_{spacer} and C_{gap}, calculated via equation (2.3).

$$Z_{\text{tot}}(\omega) = 2(L_{m,\text{NW}} + L_{k,\text{NW}}) - \frac{2}{\omega^2 C_{\text{tot}}} \tag{2.2}$$

where

$$\frac{1}{C_{\text{tot}}} = \frac{1}{C_{\text{spacer}}} + \frac{1}{C_{\text{gap}}} \tag{2.3}$$

MP resonance occurs when the total impedance Z_{tot} is zero. Therefore, the MP resonance wavelength λ_0 can be calculated by equation (2.4), where c_0 is the speed of light.

$$\lambda_0 = 2\pi c_0 \sqrt{(L_{m,\text{NW}} + L_{k,\text{NW}}) C_{\text{tot}}} \tag{2.4}$$

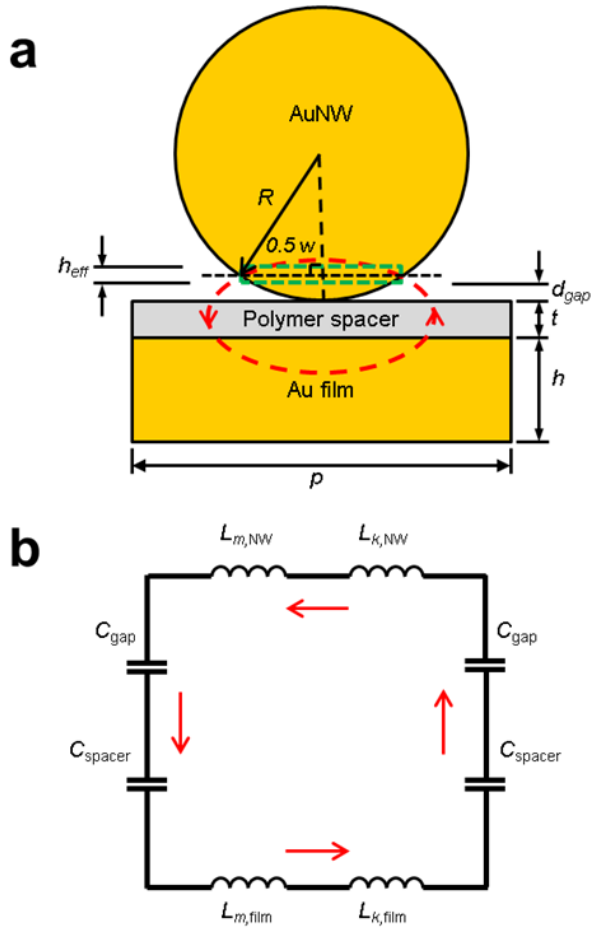

Figure 2.5. Schematic view of a unit cell of the film-coupled AuNW array; the dashed green rectangle represents the effective plate and the dashed red ellipse represents the MP excited current density loop. (b) Analogous LC circuit model.

2.4 Parametric Study

The predicted MP resonance wavelengths for different geometries are now compared in Figure 2.6 with the ones obtained from HFSS. This is done to verify that the *LC* model follows the same trends as the HFSS results. Parts (a) and (b) of Figure 2.6 show the effects on the absorptance of the metamaterial structure by varying the AuNW diameters and spacer thicknesses, respectively. Figure 2.6(a) shows that the absorption

peak redshifts as with increased nanowire diameter. On the other hand, it is observed from Figure 2.6(b) that as the spacer thickness increases, the spectral absorptance blueshifts. Parts (c) and (d) of Figure 2.6 show the absorption peak (MP resonance) wavelengths as a function of AuNW diameter and spacer thickness, respectively. The non-varying dimensions in both plots are the basic dimensions used throughout this chapter. Both plots compare the MP resonance wavelength predicted by the *LC* circuit model with that obtained from the HFSS simulations. It can be seen from the two comparison plots that the *LC* circuit model predictions agree well with the HFSS results with a maximum relative error of 5%. Figure 2.6 demonstrates the spectral tunability of the absorptance peak of the proposed film-coupled AuNW array metamaterial structure, which allows for a wider field of applications.

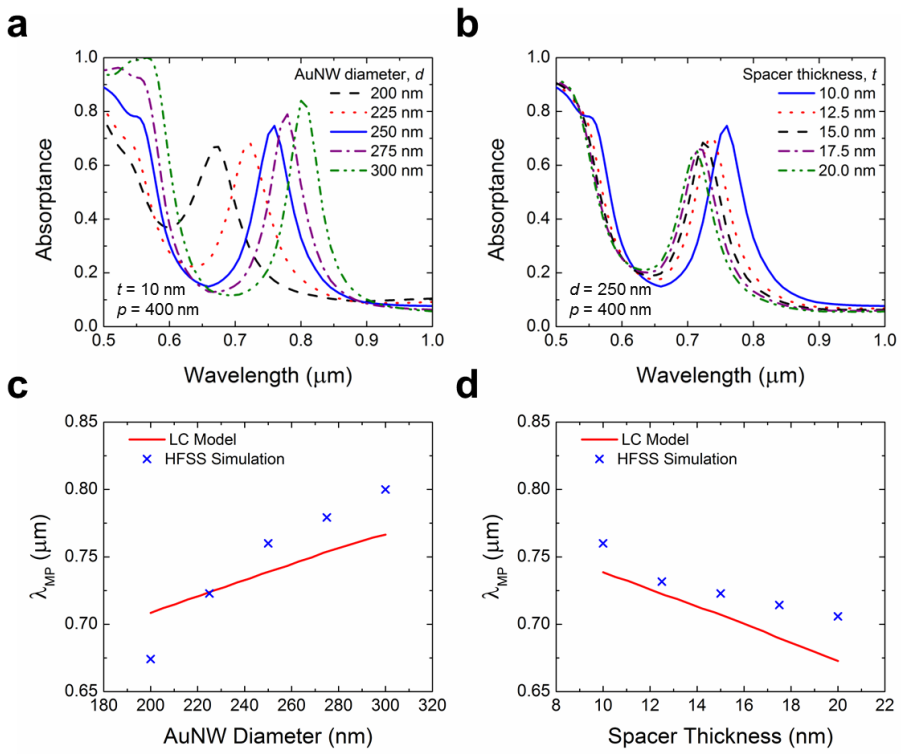

Figure 2.6. (a) and (b): Geometric effects on the normal absorptance of the film-coupled AuNW metamaterial. (c) and (d): Comparison of the MP wavelength results obtained from HFSS vs the ones obtained from the LC circuit model.

The geometric dependence of the MP resonance wavelength observed in Figure 2.6 can be understood by the *LC* circuit model. When the AuNWs' diameter increases, the MP resonance peaks redshift because of increasing L_m, L_k, and C_{tot} which leads to a larger resonance wavelength based on equation (2.3). However, increasing the spacer thickness leads to a smaller spacer capacitance C_{spacer} resulting in a smaller MP resonance wavelength or blueshift in Figure 2.6.

2.5 Thermal Analysis

In order to study the thermal response of the metamaterial structure, the solution of the HFSS simulation under MP excitation was transferred into ANSYS thermal solver. After importing the heat generation into the thermal solver, thermal boundary conditions are applied to the structure. These boundary conditions are shown in Figure 2.7. Perfectly insulated boundary conditions were used for the surfaces of the AuNW, polymer spacer, Au film, and Si substrate along the *x* and *y* directions, considering no heat flux across these surfaces. Constant temperature boundary conditions of 22^{o}C were used for the top surface of the top air volume and for the bottom surface of the Si substrate. Furthermore, a convection boundary condition, with a convection coefficient of 10 W/m^2-K, was applied to the surfaces that are in direct contact with the air volume, namely, the top surfaces of the AuNW and the polymer spacer. Furthermore, the thermal conductivities of the materials used in the thermal simulation were taken as constant values: 315 W/m-K, 148 W/m-K [71], 0.026 W/m-K [72], and 0.215 W/m-K [73], for gold, silicon, air, and the polymer spacer, respectively.

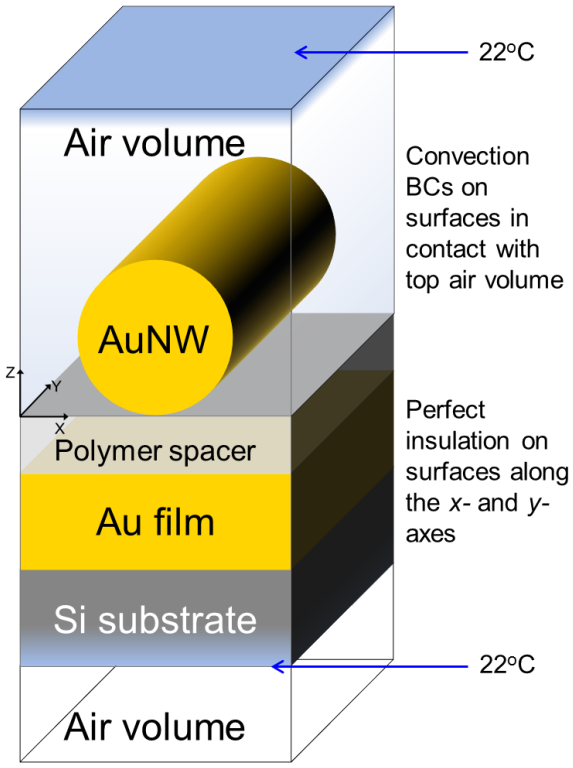

Figure 2.7. Thermal boundary conditions of the film-coupled AuNW metamaterial.

Figure 2.8 shows the effect of the mesh quality in ANSYS thermal on the steady-state temperature results across the center of the polymer spacer. It can be seen that a course mesh suffices for the simulation of the structure, as can be seen from part d of the figure. Note that the coarse mesh had 721,958 elements, the medium mesh had 1,143,709 elements, and the fine mesh had 2,242,972 elements.

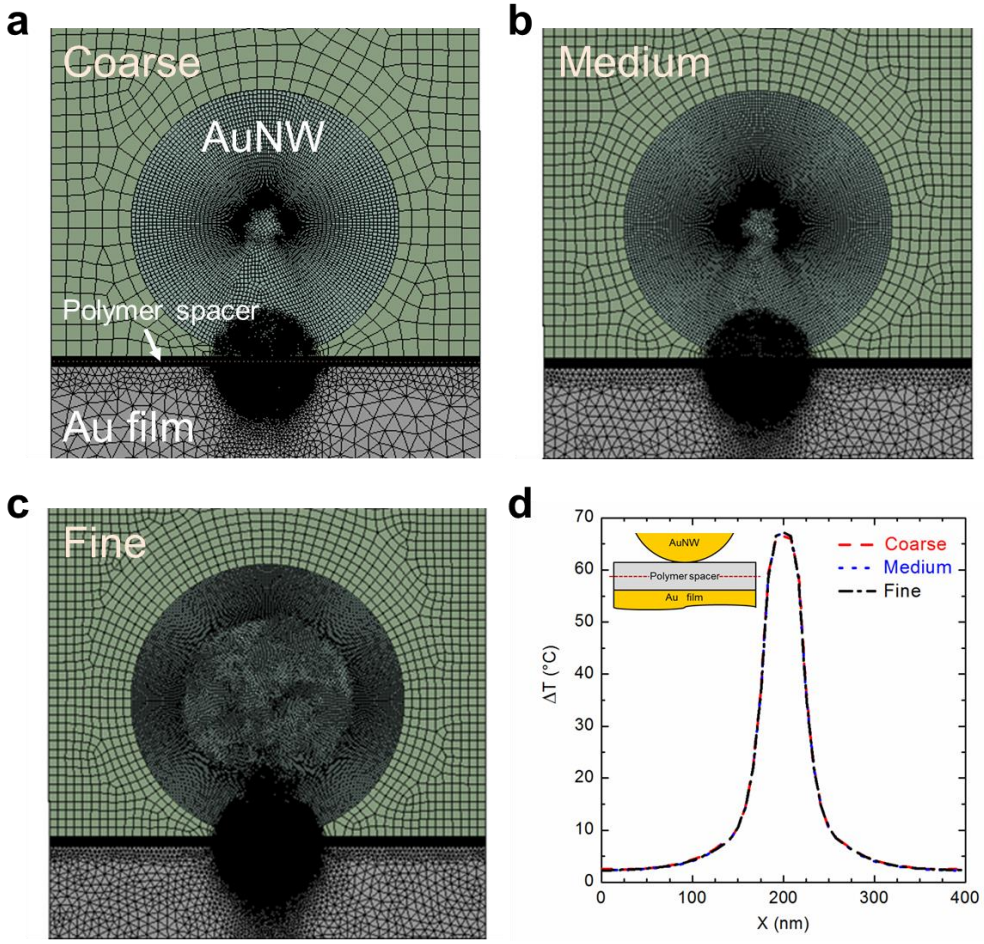

Figure 2.8. (a), (b) & (c): Mesh quality comparison between coarse (721,958 elements), medium (1,143,709 elements), and fine (2,242,972 elements) meshes. (d): Steady-state temperature (ΔT) comparison of the different meshes across the center of the polymer spacer.

Figure 2.9(a) shows the contour of the internal heat generation. The axes represent the physical dimensions of the structure and the contour represents the amount of heat generation. It can be observed that the heat generation is greatly enhanced in the bottom of the AuNW and the top of the Au film. The absorbed energy can now dissipate to the rest of the structure through conduction and convection. Moreover, this heat generation

confinement matches the confinement that is observed in the electromagnetic field distribution in Figure 2.3(a) but with only the metallic material absorbing the energy. To demonstrate localized heating, the steady state temperature distribution was obtained and is shown in Figure 2.9(b). The axes represent the physical dimensions of the structure and the contour represents the steady state temperature. For an incident power of 0.2 mW over a 400 nm × 400 nm domain, the steady state temperature of the hot spot in the polymer spacer increased to an average of 145°C at the top of the polymer spacer where it coincides with the AuNW. This enhancement is confined in a region that is approximately 33 nm wide as can be seen from the zoomed-in steady state temperature in Figure 2.9(b). This verifies, numerically, that this structure can be used to overcome the diffraction limit of light which is on the scale of a few hundred nanometers. The total heat flux contour throughout the metamaterial structure was also obtained to help understand the heat transport process as can be seen from Figure 2.9(c). The axes represent the physical dimensions of the structure and the contour represents the total heat flux. It can be observed that the majority of the heat flux is directed from the heat generation regions towards the bottom of the metamaterial structure. This means that conduction heat transfer is dominating rather than convection, which will be verified next.

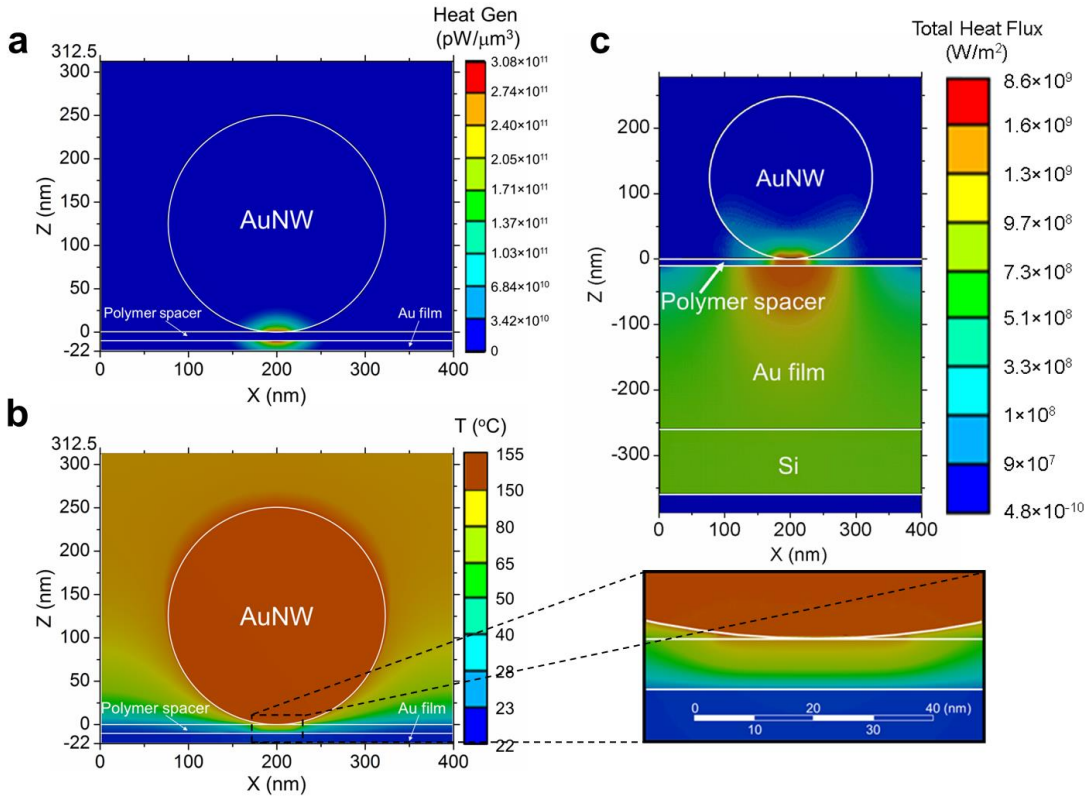

Figure 2.9. Contours when MP resonance is excited λ = 760 nm for (a) internal heat generation, (b) steady-state temperature distribution for 0.2 mW incident power, and (c) steady-state heat flux.

To check for the convection heat transfer effect, multiple convection heat transfer coefficients, h_{conv} (5 W/m^2-K to 50 W/m^2-K), were used for the surfaces in contact with air, namely, the outer surface of the nanowires and the top surface of the polymer spacer. Figure 2.10 shows the steady state temperature rise (ΔT) at three temperature probes in the polymer spacer. The x-axis represents the convection heat transfer coefficient and the y-axis represents ΔT from the ambient temperature (22°C). The inset of Figure 2.10 shows the location of the probes that were used for the plot. The top and bottom probes are 0.5 nm deep into the polymer spacer from its top and bottom surfaces, respectively.

Meanwhile, the center path is located halfway into the polymer spacer. Moreover, the three probes were placed at the center of the structure with respect to the x-direction. It can be seen from Figure 2.10 that convection heat transfer did not have a significant effect on the steady state temperature. To understand why convection heat transfer was not significant, a comparison was made between the thermal resistance for convection, $R_{conv} = 1/(h_{conv}A)$ and conduction across the polymer spacer, $R_{cond} = t/(kA)$, where h_{conv} is the convection heat transfer coefficient, A is the cross sectional area that heat crosses, t is the thickness of the polymer spacer, and k is the conductive heat transfer coefficient. It was found that convective thermal resistance was six orders of magnitude higher than the conductive thermal resistance. This means that heat would transfer through conduction much more readily than through convection. To check for the radiation heat transfer effect, an emissivity of 1 was used for the radiating bodies. Radiation heat transfer was found to be insignificant as the steady state temperature did not change when applying radiation boundary conditions for a black body, which represents the maximum radiated power. To verify this, first, the radiation thermal resistances for the AuNW and the polymer spacer were calculated by $R_{rad} = 1/(h_{rad}A)$. The temperatures of the AuNW and the polymer spacer were taken as uniform with a value equal to the maximum temperature of the structure. This resulted in the minimum radiation thermal resistance and was used in order to be able to make a comparison with the conduction thermal resistance across the polymer spacer. It was found that radiation thermal resistance from the AuNW was five orders of magnitude larger than the conductive thermal resistance, and for the polymer spacer, it was six orders of magnitude larger. This indicates that conduction is the dominant mode of heat transfer in the structure and radiation heat transfer is insignificant in this case.

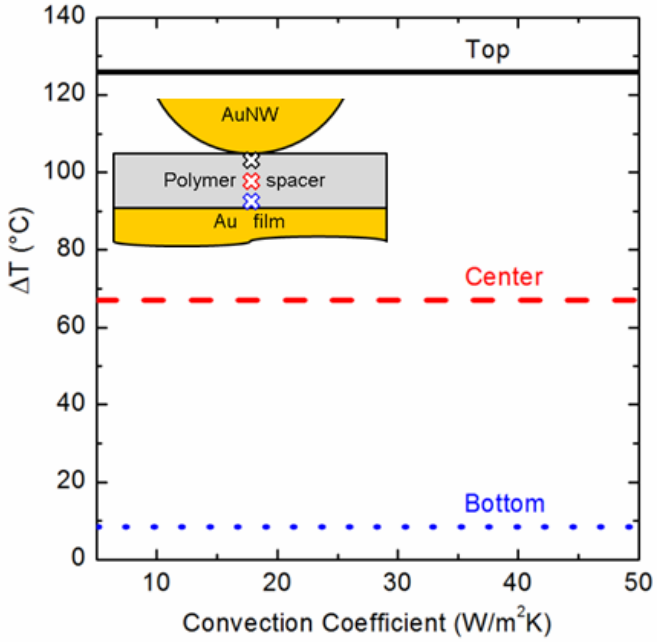

Figure 2.10. Convection effect on the steady state temperature rise (ΔT) of the film-coupled AuNW metamaterial at different probes across the polymer spacer. Ambient temperature is 22°C.

Figure 2.11(a) shows the ΔT profile along three paths that cross the polymer spacer at different depths. The y-axis represents ΔT from the ambient temperature (22°C). The inset of Figure 2.11(a) shows the three paths that were used for the plot. The top and bottom paths are 0.5 nm deep into the polymer spacer from its top and bottom surfaces, respectively. Meanwhile, the center path is located halfway into the polymer spacer. Figure 2.11(a) provides us with a more accurate way of knowing the width of the localized hot spot, which is determined to be ~33 nm with an average ΔT of 123°C. Note that the full width at half maximum (FWHM) in the polymer spacer is 50 nm along the x-direction. The FWHM is defined as the width (in the polymer spacer, along the x-direction) at which ΔT

is half its maximum value. Moreover, to determine the amount of incident power required to heat up the structure to various temperatures, the effect of the incident power on the steady state temperature is also studied and is shown in Figure 2.11(b). The plot shows the steady state temperature as a function of incident power. The temperature probes used for this plot are the same ones used for Figure 2.10. Moreover, the depth of the structure in the y-direction was fixed at 400 nm to determine the amount of incident power in milliwatts, which in the simulations was varied from 0.02 mW to 0.2 mW. Note that the temperature of the top of the polymer spacer is significantly affected by the incident power, while the temperature of the bottom of the polymer spacer does not change significantly when increasing the incident power. This is because the Au film is highly conductive, which leads to the temperature of the bottom of the polymer spacer to remain at the same temperature as the Au film. On the other hand, the temperature of the top of the polymer spacer increases because a larger heat flux induces a larger temperature difference between the top and bottom surfaces of the polymer spacer.

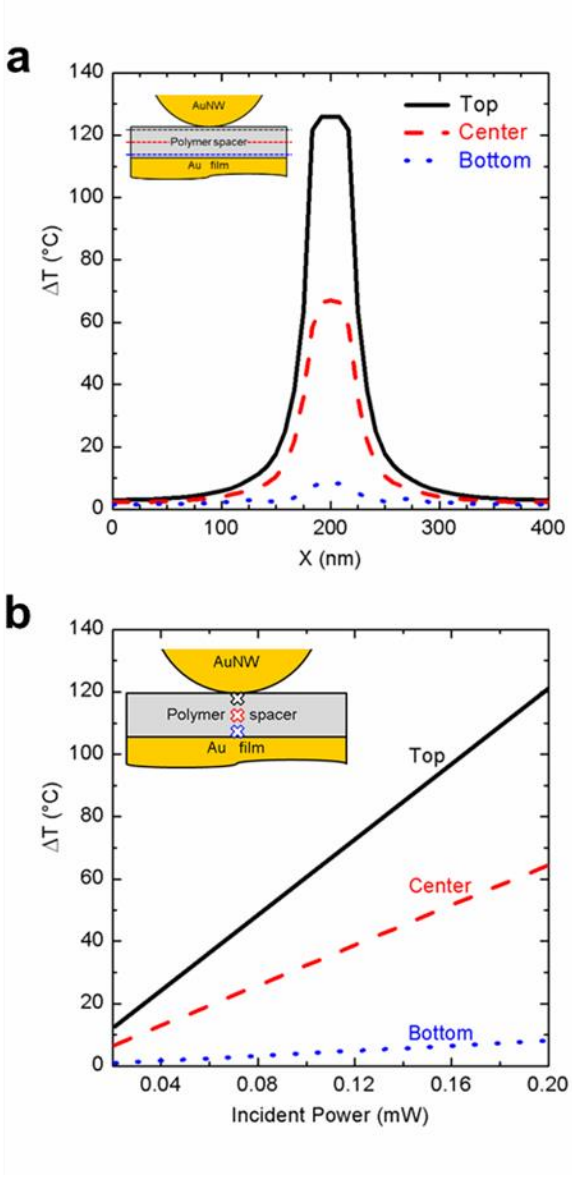

Figure 2.11. Steady-state temperature rise (ΔT) at MP resonance (λ = 760 nm) as a function of: (a) distance across the polymer spacer in the x-direction along different paths, and (b) incident power for different temperature probes. The insets show the location of the paths or probes. Ambient temperature is 22^{o}C.

The transient temperature results for the continuous light source are shown in Figure 2.12. Note that ANSYS thermal solver uses adaptive time-stepping and the chosen initial time step was 3 ns, the minimum time step was 0.3 ns, and the maximum time step

was 30 ns. To study how ΔT and the width of the hot spot develop with increasing time, ΔT along the center path of the polymer spacer is plotted in Figure 2.12(a) at different time steps. The width of the localized hot spot along the center path is determined to be ~16 nm with a ΔT of ~66.5°C after ~0.6 μs. Moreover, a vertical path across the Au film, the polymer spacer, and the AuNW is used in Figure 2.12(b) to show ΔT change across the different components of the structure, with increasing time. It can be seen from Figure 2.12(b) that ΔT across the Au film remains constant with increasing time. In the polymer spacer region, a sharp increase in ΔT is observed and this increase becomes even sharper with increasing time. However, the temperature across the AuNW is also relatively constant, but in this case, it changes with time. The cause of the constant temperature in the components made from gold is that gold has a high thermal conductivity which leads to a more uniform temperature profile. Note that, within the polymer spacer along the z-direction, the steady state ΔT reduces to half its maximum value at a distance of 5 nm from the top of the polymer spacer. Furthermore, to determine when the structure reaches steady state, the transient temperature response for three temperature probes was studied and the results are presented in Figure 2.12(c). The temperature probes used here are the same ones used in Figure 2.10. Moreover, sufficient time was given for the temperature to stabilize and the system to reach steady state. The time scale used for the transient response was 0.6 μs. The x-axis in the plot represents the time in μs while the y-axis represents ΔT at the probes. It can be seen from Figure 2.12(c) that the temperatures of the three probes stabilize at around ~0.36 μs which is when the relative change in ΔT slows down to below 1%. This means that the system reaches steady state within ~0.36 μs.

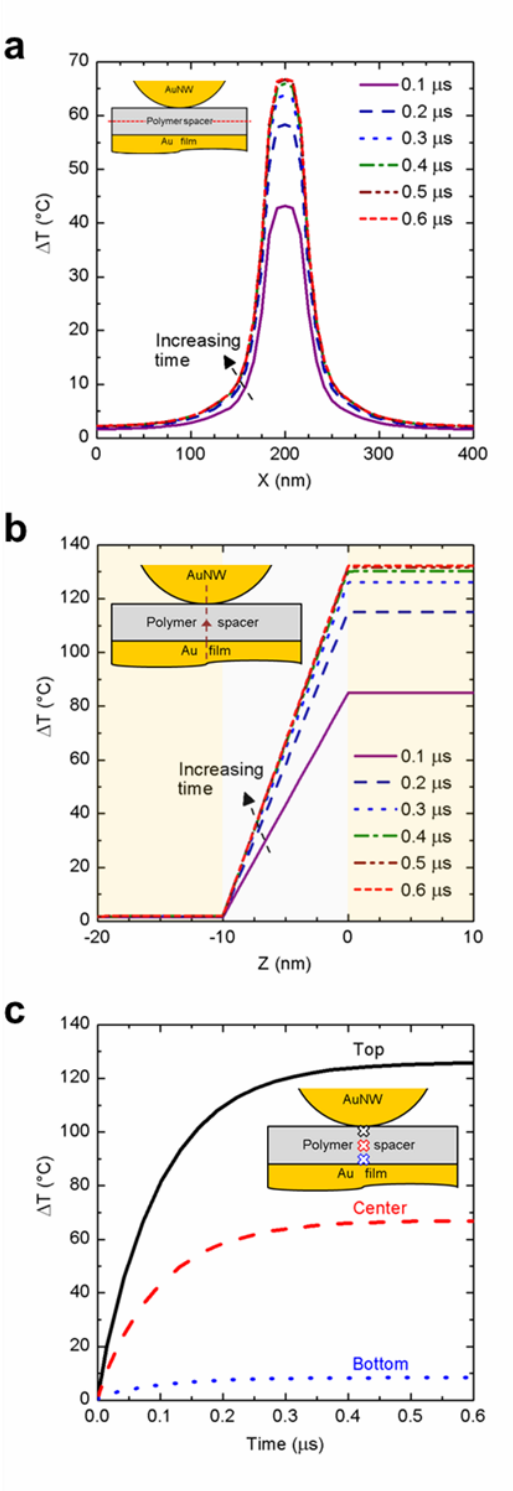

Figure 2.12. Transient temperature response when MP resonance is excited inside the film-coupled Au nanowires at λ = 760 nm for different paths and probes: (a) Center path

across the polymer spacer. (b) Vertical path across the Au film, the polymer spacer, and the AuNW. (c) Temperature probes in the polymer spacer. The insets show the location of the paths or probes. Ambient temperature is 22^{o}C.

Plasmonic localized heating at the nanoscale was demonstrated through numerically investigating a film-coupled AuNW array metamaterial. HFSS simulations showed that the structure exhibits selective absorption at MP resonance, which, with the chosen structure dimensions, was at a wavelength of 760 nm. Moreover, the ANSYS thermal solver simulations indicated a steady state average temperature of 145°C in a hot spot of ~33 nm, where the electromagnetic energy was confined, demonstrating nanoscale plasmonic localized heating. In the polymer spacer, the FWHM was 50 nm along the x-direction, and ΔT dropped to half its maximum value at a distance of 5 nm from the top of the spacer along the z-direction. Furthermore, transient temperature profiles showed that the system reaches steady state within ~0.36 μs. The findings of this work may facilitate applications in the fields of energy harvesting (by using multi-sized nanowires to enable broadband absorption), data storage (high speed, high density storage), and biotherapy (killing cancer cells without harming nearby healthy cells).

CHAPTER 3 FABRICATION AND CHARACTERIZATION OF NANOPARTICLE METAMATERIAL

Spectrally selective nanoparticle-based metamaterial absorbers such as film-coupled gold nanoparticles and film-coupled nanodiscs can be easily fabricated to make absorbers with selective narrow-band radiative properties. The selectivity of these metamaterial absorbers and their ease of fabrication allows for them to be fabricated in different geometries to also be used as broadband absorbers by exciting multiple resonances. Figure 3.1 shows a schematic of the nanoparticle-based metamaterials that were fabricated. The structures are a film-coupled gold nanoparticle absorber, and an aluminum nanodisc absorber, with and without a middle dielectric layer. Aluminum was used as the nanodisc material since it is an inexpensive material that has more distinct selective absorption compared to gold. Gold has higher absorption below λ = 600 nm due to the bandgap transition which would result in a lower reflectance in that range [74]. On the other hand, aluminum has a reflectance of more than 85% throughout in the visible and near-infrared range [66].

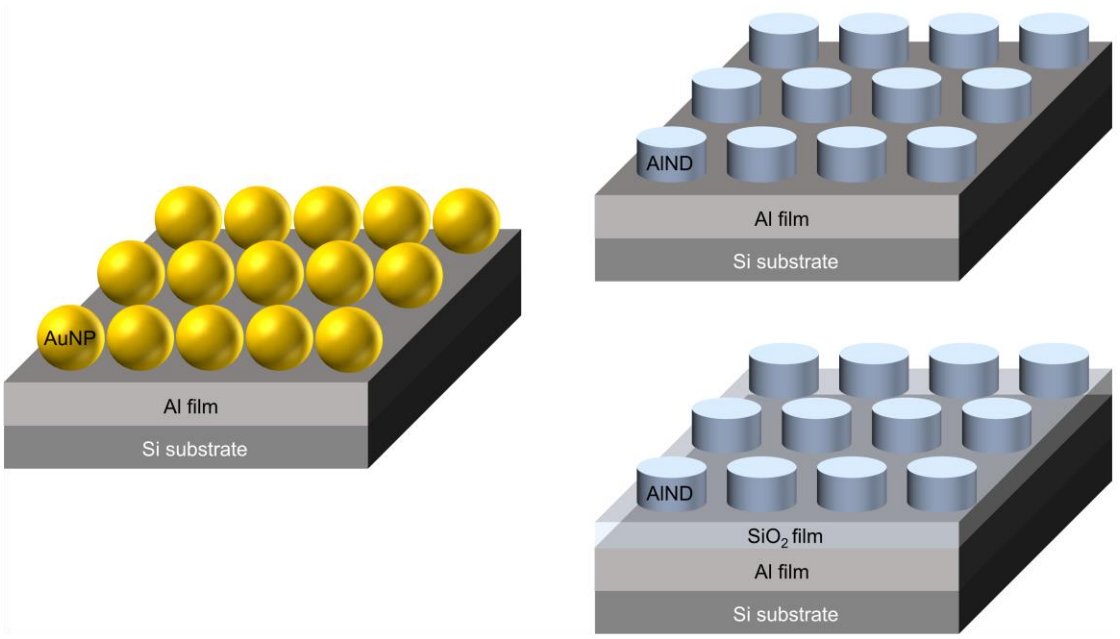

Figure 3.1. Nanoparticle-based metamaterial absorbers to be fabricated.

3.1 Fabrication of Film-Coupled Gold Nanoparticle Metamaterial Absorbers

A variety of fast and inexpensive techniques exist to apply nanoparticles to films. This can be used to achieve spectrally selective absorption making them an attractive option for large scale narrow-band absorbers or broadband solar absorbers. A layer of monodispersed nanoparticles, through self-assembly, can be applied to a film by several methods such as utilizing long-range attractive interactions or capillary forces between the nanoparticles [18-21]. Spin-coating was found to be most accessible to achieve a single-layer of tightly packed film-coupled gold nanoparticles.

A pipette was used to extract colloidal nanoparticles (Cytodiagnostics, G-250-20) from a bottle. The nanoparticles were 250 nm in diameter and had a concentration of 7.1×10^{8} particles/mL. The aluminum-coated silicon wafer that was used as the substrate was first cleaned by diluted (DI) water, then ultrasonicated in acetone, and lastly went through an oxygen plasma cleaning (Blue Lantern, Nano BL1) process to remove organic

materials from the surface to allow for better spreading of the nanoparticles across the wafer when spin-coating. The nanoparticle colloidal suspension was then applied to the aluminum-coated silicon wafer. A spin-coater was used to spread the gold nanoparticle colloidal suspension across the wafer. The spin-coating technique went through several iterations until a single-layer of tightly packed gold nanoparticles was obtained. The spin speed for the spin coater was set at approximately 3000 RPM for one minute and thirty seconds. Moreover, multiple trials with different concentrations of the colloidal suspension were attempted to obtain tightly packed nanoparticles. Figure 3.2 shows a schematic of the fabrication process.

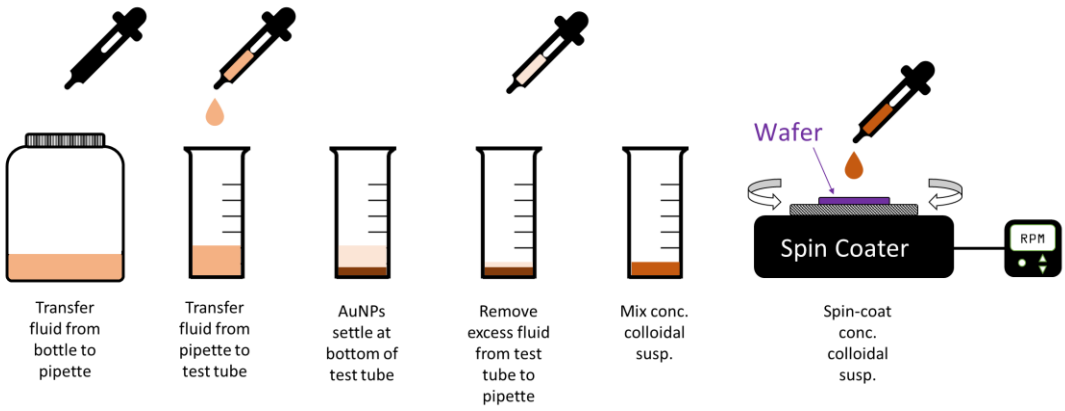

Figure 3.2. Fabrication of film-coupled gold nanoparticle metamaterial absorber.

Figure 3.3(a) shows an SEM image of a single unconcentrated drop of the colloidal gold nanoparticle suspension spread across the aluminum silicon wafer. It can be seen that the nanoparticles are not tightly packed, which means that the effect of the gold nanoparticles would not be strong and the measured reflectance would be instead mainly from the aluminum substrate.

To improve the packing of the nanoparticles, we increased the concentration of the colloidal suspension drops applied to the wafer. Parts b, c, and d of Figure 3.3 show SEM images of concentrated colloidal suspensions. The concentration increase was achieved by dropping a drop of the colloidal suspension into a small test tube. The colloidal suspension was then left in a fume hood until the nanoparticles settled at the bottom of the test tube. A pipette was then used to remove most of the colloidal liquid, leaving only a small amount that was then mixed with the nanoparticles. To achieve further concentration, more drops were added, and the process was repeated. Note that for the 15 concentrated drops, the spin coating time was extended to two minutes since the drop was very viscous and difficult to spread.

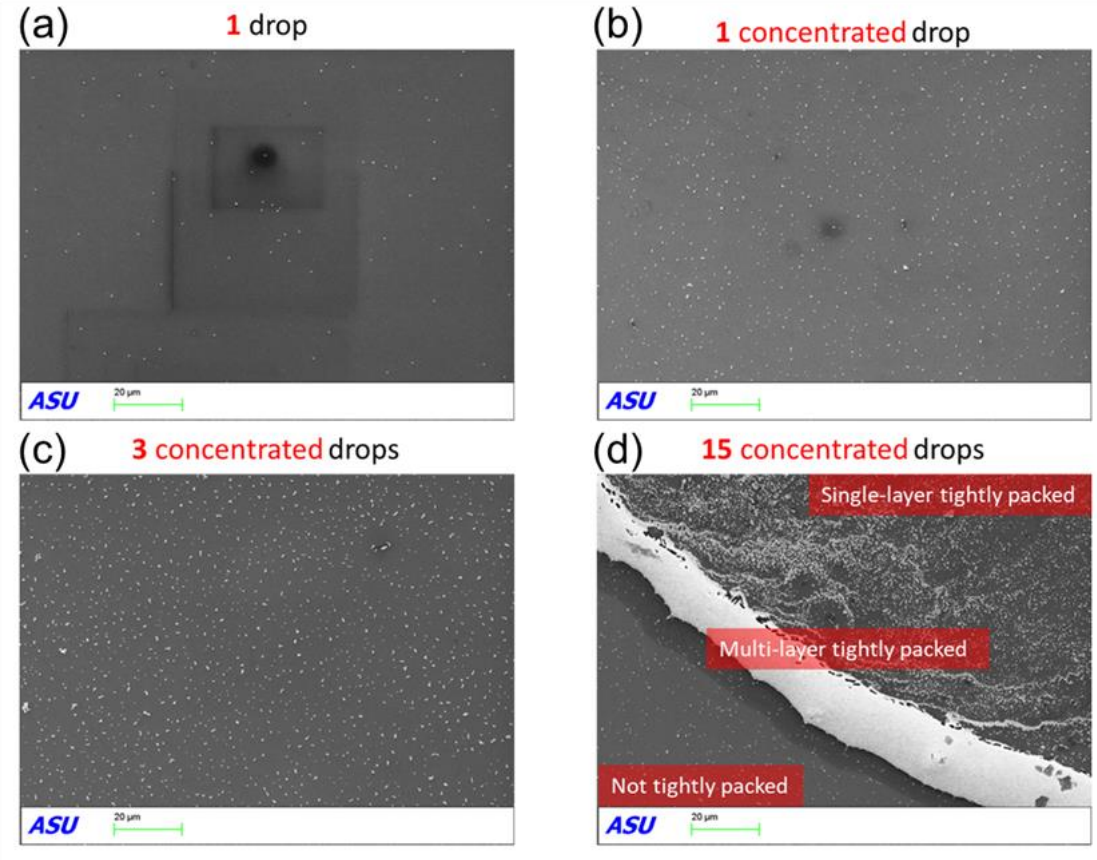

Figure 3.3. SEM images of AuNPs on Al-coated Si wafer.

Figure 3.4 and Figure 3.5 show two locations of the sample with 15 concentrated drops at different scales. In both figures, it can be seen that a single-layer of tightly packed gold nanoparticles was obtained. The single-layer tightly packed nanoparticles cover at least a 100 μm diameter circle in both figures. However, most of the tightly packed nanoparticles had self-assembled in multi-layers. Therefore, the spin-coating technique could be further improved to obtain a larger area of single-layer tightly packed gold nanoparticles with more of the nanoparticles more tightly packed.

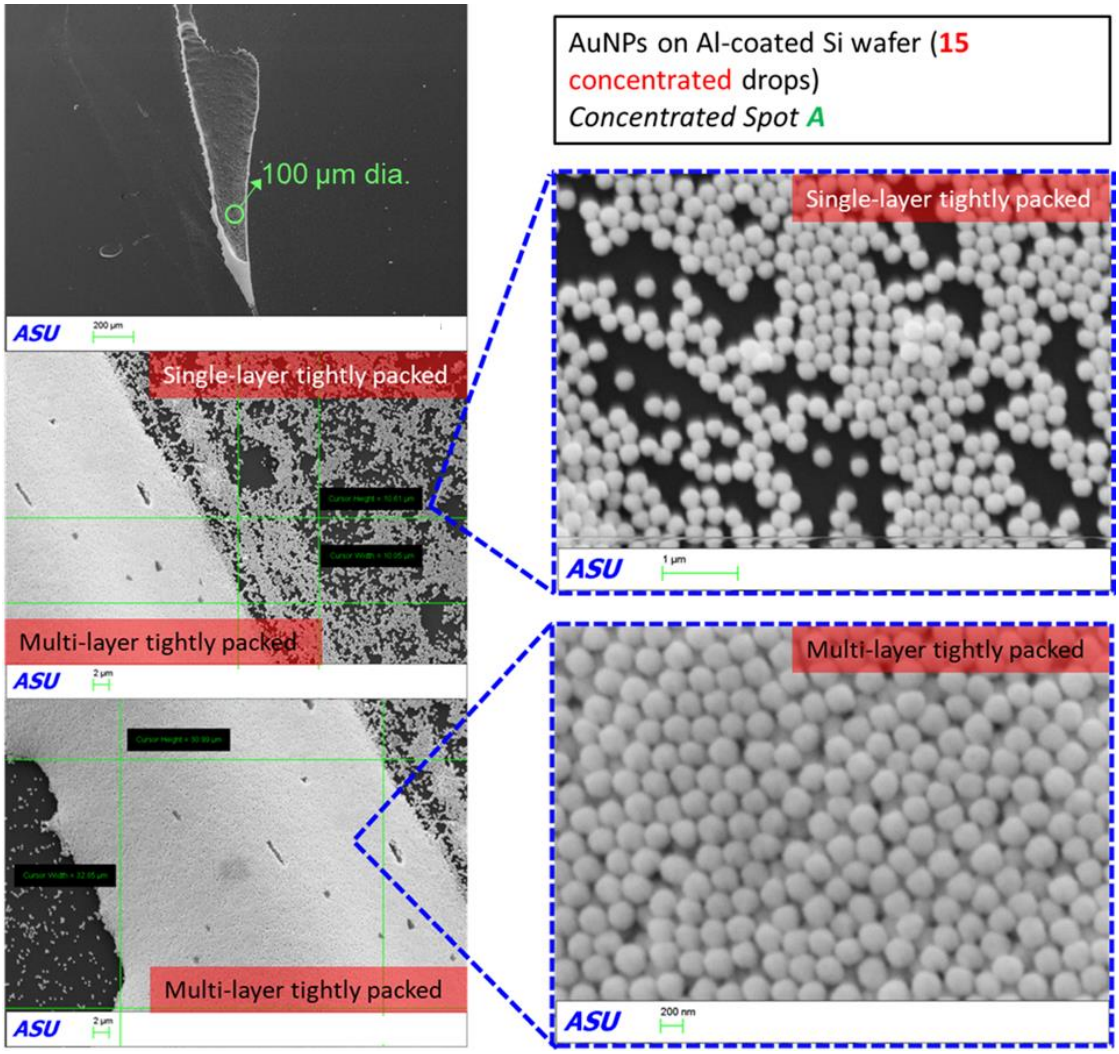

Figure 3.4. SEM images of AuNPs on Al-coated Si wafer (15 drops, spot A).

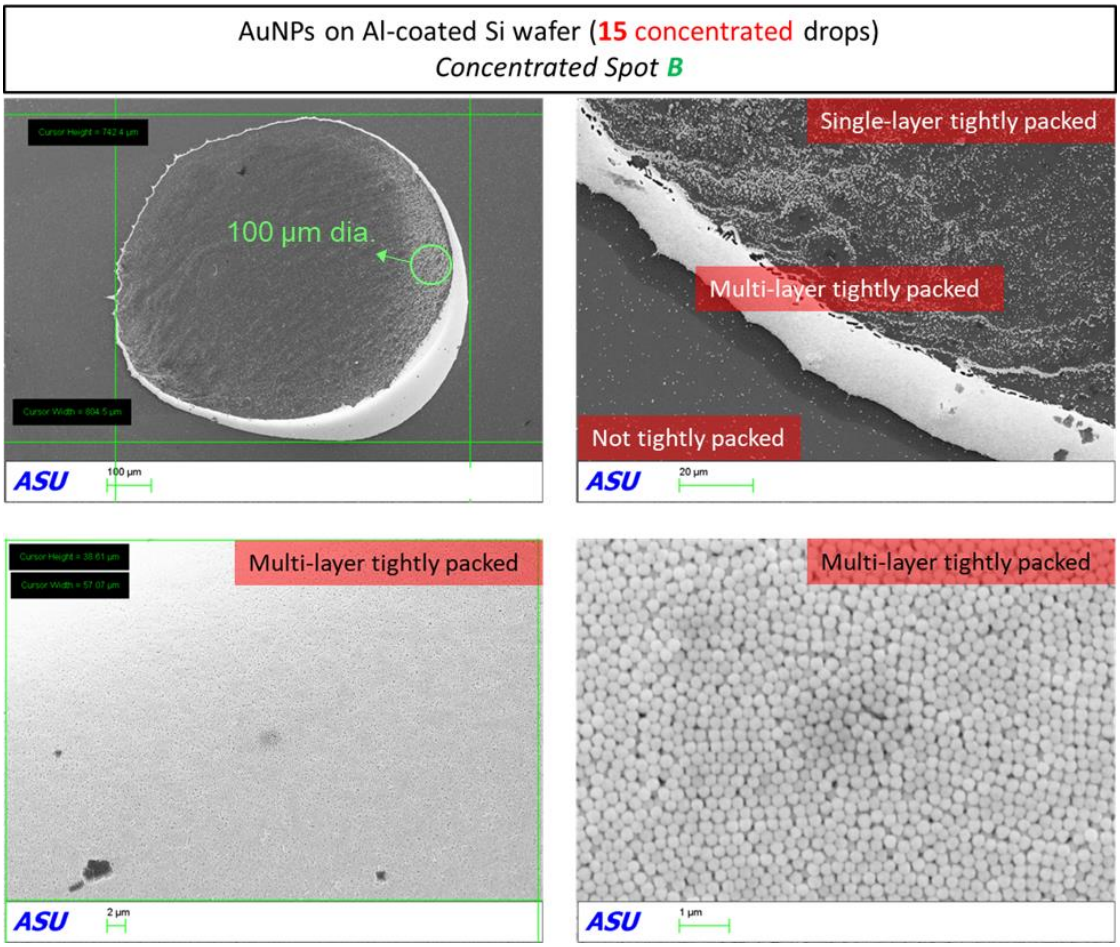

Figure 3.5. SEM images of AuNPs on Al-coated Si wafer (15 drops, spot B).

Figure 3.6 shows the FTIR measured reflectance of the concentrated drops. It can be seen that the plots have a noticeable broad decrease in the reflectance around ~850 nm with the 3 concentrated drops sample having a larger reflectance dip than the 1 concentrated drop sample. However, for the 15 concentrated drops sample, the reflectance dip is the least noticeable of the three samples. The reason could be due to the non-uniformity of the gold nanoparticle spread across the wafer in the 15 concentrated drops sample, as opposed to the other two samples which have a less tightly packed but more uniform distribution of the nanoparticles. Therefore, the FTIR cannot accurately measure the reflectance of the film-coupled nanoparticles since they would be concentrated in a spot that is on the order

of microns, which is much smaller than what the FTIR can measure in the visible range (order of millimeters).

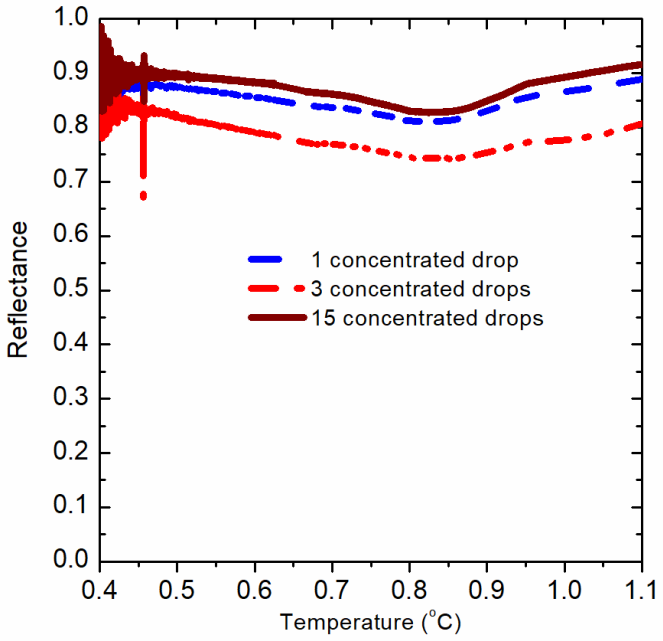

Figure 3.6. Reflectance of the concentrated drops (gold nanoparticles on an aluminum-coated silicon wafer) measured by an FTIR.

From the previous results, it can be seen that the film-coupled gold nanoparticles are not the best candidate for experimentally demonstrating narrow-band and broadband reflectance, mainly for two reasons: the samples could not consistently be packed in a single layer in a repeatable robust way, and the spacing between the nanoparticles could not be controlled as the nanoparticles are either far apart or tightly packed. Therefore, another approach was used to make an alternative nanoparticle-based metamaterial absorber. Utilizing anodized aluminum oxide (AAO) templates, an aluminum nanodisc

(AlND) metamaterial absorber was fabricated that allowed for more control over the geometry of the structure.

3.2 Fabrication of Aluminum Nanodisc Metamaterial Absorbers

Ultrathin anodized aluminum oxide (AAO) templates have been previously used to fabricate periodic nanostructures in a fast and inexpensive way [75-77]. In this chapter, we will discuss using the AAO templates in the fabrication of aluminum nanodisc (AlND) metamaterial absorbers. The templates shipped from the manufacturer (TopMembranes UT450-370-700) on a PMMA layer to protect the templates since they are ultrathin (700 nm) and therefore fragile. The diameter of the pores of the templates were approximately 390 nm (370 nm - 410 nm) and the period was 450 nm. The templates were transferred onto an aluminum coated silicon substrate. The transfer process consisted of several steps that are shown in Figure 3.7. First, three beakers with acetone were prepared. The acetone is needed to remove the PMMA from the templates and facilitate the transfer of the templates onto the substrate. A flashlight is also required to illuminate the template in the beaker. Placing the beaker on a dark background helps make the template more visible. The templates were then cut with scissors into small pieces to reduce the number of wrinkles that result after the transfer is completed. Next, the templates were placed into the first acetone beaker and left there for three to ten minutes for the template to separate from the PMMA. Some of the PMMA dissolved in the acetone and the remaining PMMA was removed from the beaker. Next, the substrate was used to fish the template out of the acetone. The substrate should be removed from the acetone slowly and preferably at a 45-degree angle. The sample was then left to dry. Once dried, the sample was placed into the second acetone beaker to remove any residual PMMA. After three to ten minutes, the

sample was removed, dried, and placed into the third acetone beaker. After another three to ten minutes, the sample was removed and left to dry. This concluded the template transfer process onto the substrate.

Next, aluminum was deposited, via e-beam deposition, onto the sample (Lesker PVD75 Electron Beam Evaporator). Aluminum pellets (99.99% purity) were evaporated at a rate of 2.5 Å/s and a base pressure of $1x10^{-6}$ Torr. The substrate the AlNDs were deposited on was a double side polished silicon wafer that was 38m microns thick and had a resistivity of 10-25 ohms-cm. During deposition, the aluminum filled the pores of the template until the required aluminum disc height was reached. Finally, Kapton tape was used to strip the template from the sample. The template came off easily, leaving behind the AlNDs on the aluminum substrate. Images of the fabrication process are shown in Figure 3.8. Figure 3.9(a) shows images of the template before the aluminum deposition, after the deposition, and the AlNDs after removing the template samples. Figure 3.9(b) shows SEM images of the template and Figure 3.9(c) shows images of the AlNDs on an aluminum coated silicon substrate. It can be seen from Figure 3.9(b), that the template is relatively uniform with the pores being approximately 390 nm in diameter with a ±5% variance. However, there are some holes that have combined to form flower like shapes that would affect the reflectance of the sample. Additional images of the fabricated samples can be found in Appendix B.

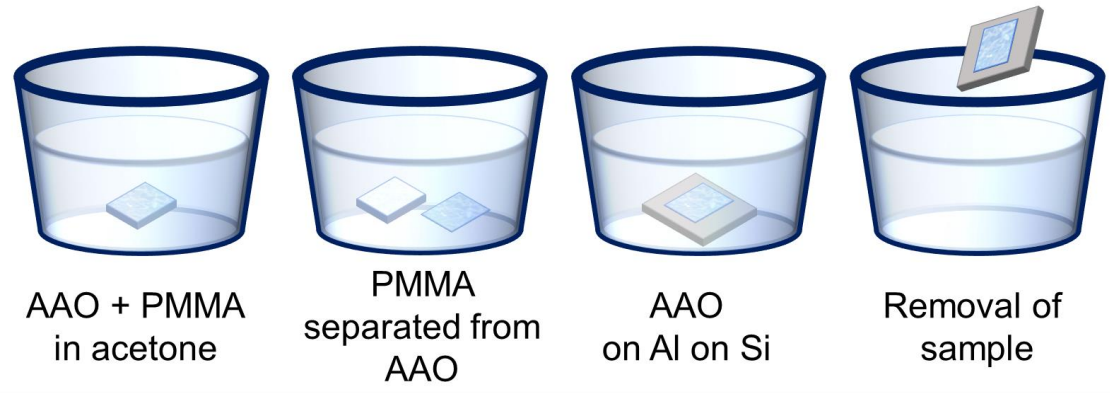

Figure 3.7. Schematic of the AAO template transfer process.

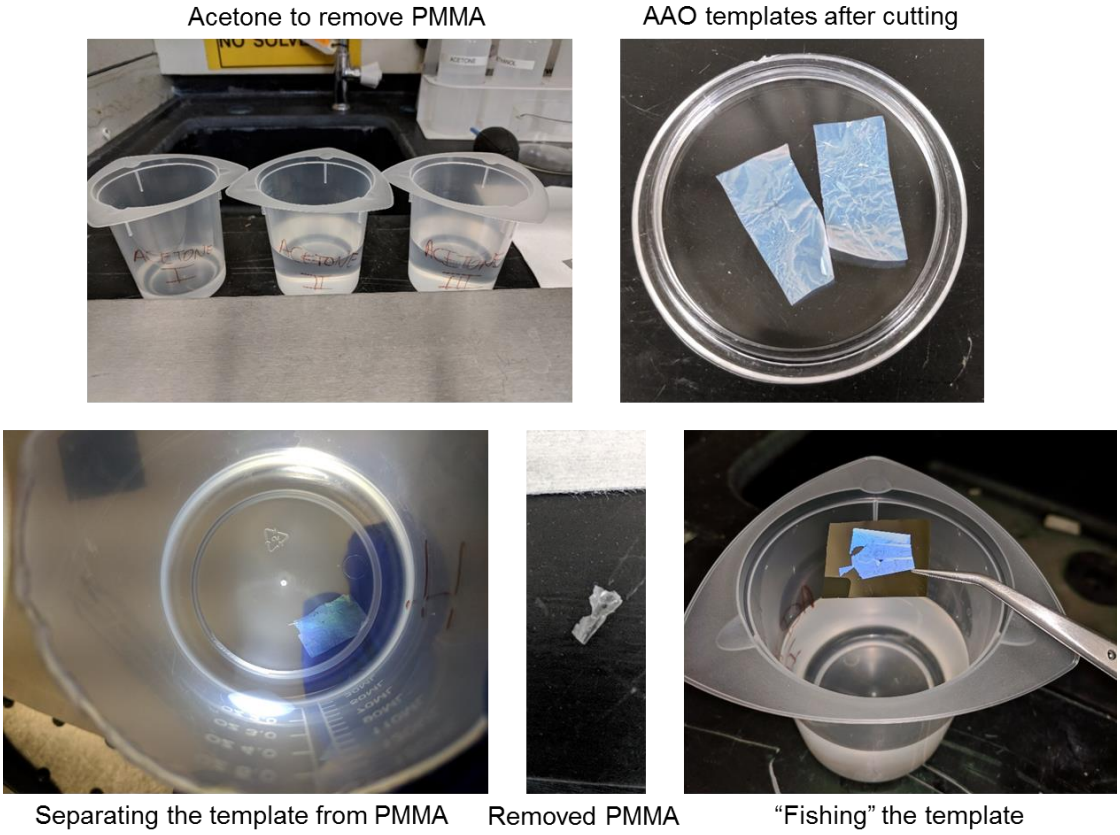

Figure 3.8. Images of the AAO template transfer process.

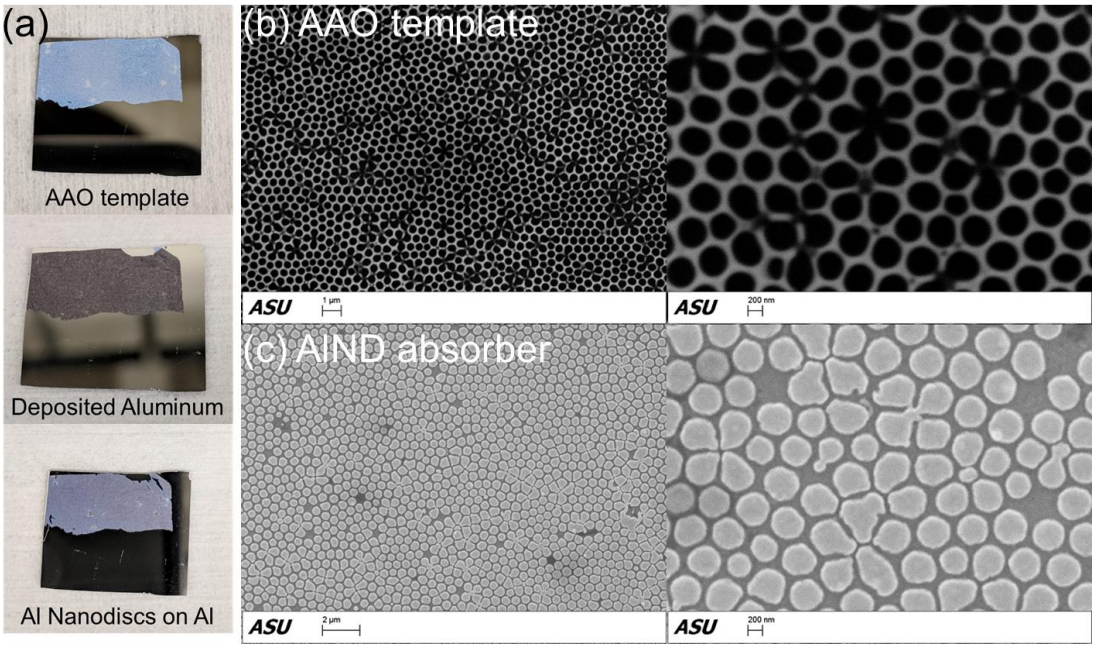

Figure 3.9. (a) Camera images, (b) SEM images of the AAO template before aluminum deposition, and (c) SEM images of the AlND metamaterial absorber.

Adding a dielectric layer in between the AlNDs and the aluminum substrate would lead to the excitation of additional resonance wavelengths in the dielectric gap between the AlNDs and the Al substrate. This would lead to more broadband absorption. SiO_2 was used as the dielectric layer and adding it led to an energy confinement in the dielectric SiO_2 in addition to the original confinement of energy between the AlNDs. 50 nm of SiO_2 was deposited using remote plasma chemical vapor deposition (RPCVD, PlasmaQuest RPCVD 333) with a chuck temperature of 300 °C, a chiller temperature of 40 °C, and a rate of 0.86 Å/s. Figure(a) shows camera images of the AlND/SiO_2/Al sample and Figure(b) shows SEM images of the sample. Additional images are shown in Appendix B. It can be seen from the camera images that the fabrication technique is not as effective when dealing with a sample with a dielectric SiO_2 film. The resulting sample has many discontinuities. Treatment methods such as hydrophobic and hydrophilic treatments were used to improve

the wettability of the surface to acetone but this did not enhance the contact between the AAO template and the dielectric SiO_2 film.

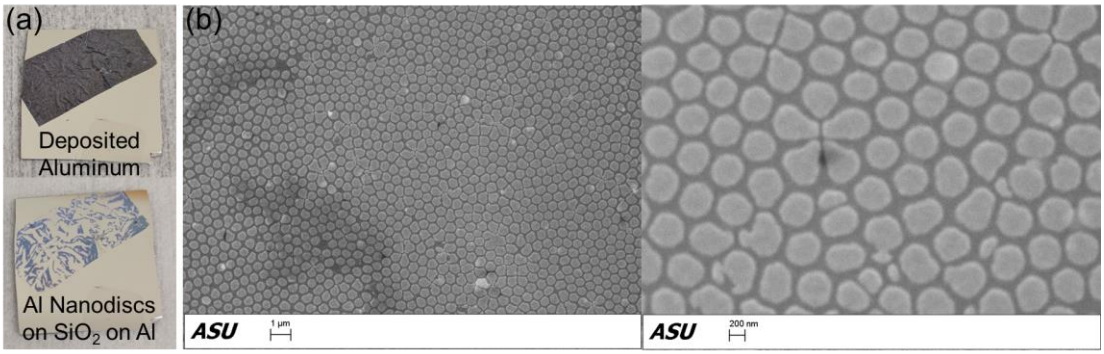

Figure 3.10. (a) Camera images and (b) SEM images of the AlND/SiO2/Al metamaterial absorber.

3.3 Micro-Scale Optical Reflectance and Transmittance (MORT) Microscope

From the previous section, we can see that the fabrication process of the AlNDs resulted in samples that have wrinkles in them resulting in discontinuities in the AlNDs. This meant that if an FTIR bench were to be used to measure the reflectance of the AlNDs, the measured results would not accurately represent the nanodisc behavior, since the reflectance of the defects and discontinuities is also captured. An FTIR microscope can measure micro-scale samples, however, it can only measure in the infrared range. Therefore, a new instrument, named the microscale reflectance and transmittance (MORT) microscope was developed to measure the reflectance (and transmittance) of micro-scale samples in the visible range. Figure 3.11 shows a schematic of the MORT microscope showing both its operating modes: (a) reflectance mode, for semi-transparent and opaque samples and (b) transmittance mode, for semi-transparent samples. Figure 3.12 shows an image of the setup. In reflectance mode, light from a broadband tungsten-halogen lamp

(Thorlabs SLS201) goes through the light source leg of a bifurcated fiber bundle (Thorlabs RP28) into a collimator (Thorlabs F220 SMA-A) that collimates the diverging light exiting the fiber. The collimated light then gets split into two parts via a 50:50 beam splitter (Thorlabs BS013), with half of it going down towards the sample. The collimated light that is directed towards the sample goes through an objective and is focused onto the sample. The reflected light then goes back into the objective and half of it goes through the beam splitter to a CMOS camera (Thorlabs) at the top of the MORT microscope. The other half is directed back into the original collimator and is focused into the fiber. The light then goes through the spectrometer leg of the bifurcated fiber and into a CCD spectrometer (Thorlabs CCS200). The spectrometer finally sends the reflected signal on a wavelength basis to a computer via USB. In transmittance mode, the CCD spectrometer is not connected to the bifurcated fiber, but is rather connected to another fiber (which is connected to a collimator, Thorlabs F260 SMA-A connected to a LA1540-ML lens) that is positioned below the sample.

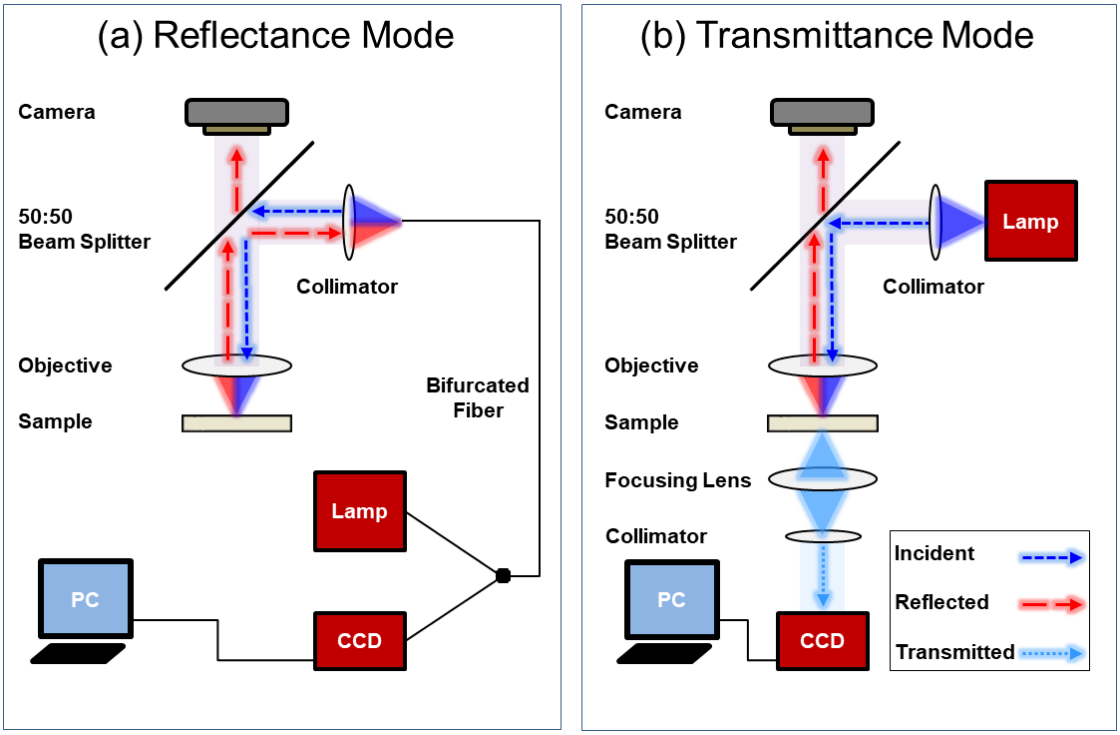

Figure 3.11. Schematic of the microscale optical reflectance and transmittance (MORT) microscope.

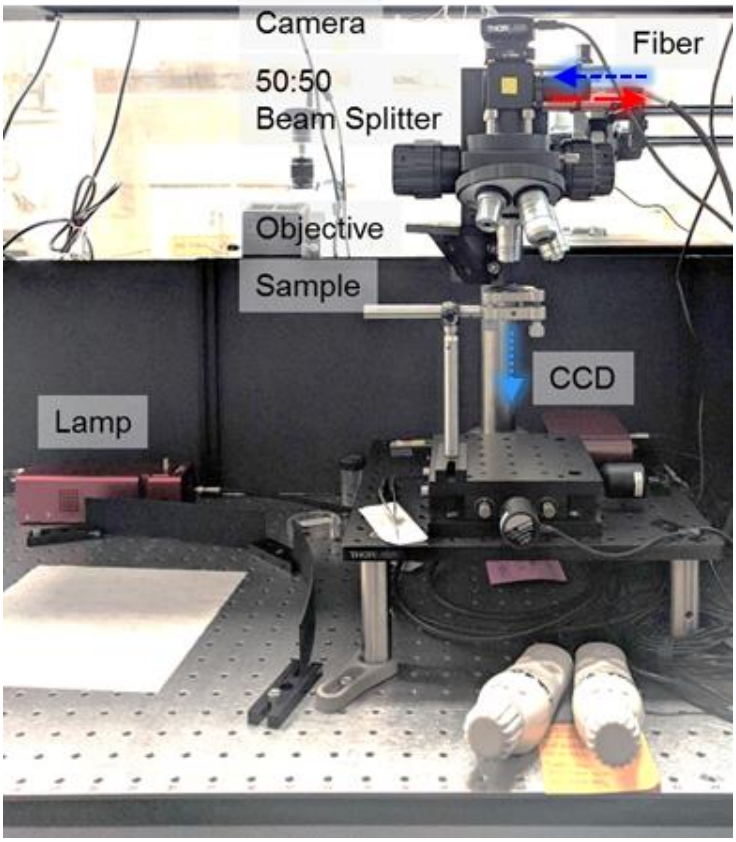

Figure 3.12. Image of the MORT microscope.

To test the reflectance mode of the MORT microscope, an undoped silicon sample was used and its reflectance was compared with the reflectance measured by an FTIR. First, a clean aluminum mirror was used as a reference for the reflectance measurement of the undoped silicon. The aluminum mirror was placed on the mirror mount sample holder. Light was then focused on the mirror using the MORT objective. Next, the mirror was replaced with the silicon sample and the reflected signal was measured. The reflectance of the silicon sample was then calculated by taking the ratio of the reflected signal from the silicon sample to the reflected signal from the aluminum mirror. The results were compared with the FTIR transmittance measurements for the same sample. The reflectance measured

by the MORT microscope is shown in Figure 3.13 along with the reflectance measured by the FTIR bench. It can be seen that the two measurements agree well.

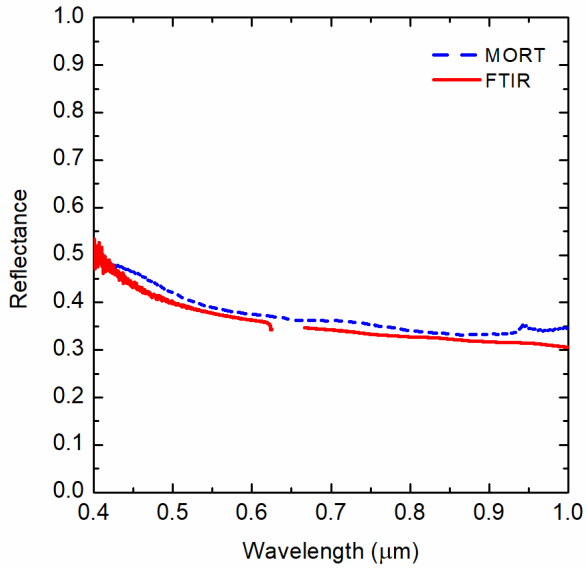

Figure 3.13. Reflectance of undoped silicon.

To test the transmittance mode of the MORT microscope, silicon carbide (SiC) was used as a reference sample. A SiC sample (Xiamen Powerway Advanced Material Co., Ltd., resistivity > 1×10^5 ohm-cm, surface roughness < 0.5 nm) was first placed on a thin black disc with an aperture in the center. The disc was placed on the mirror mount sample holder. Light was then focused on the clean SiC sample using the MORT objective. Next, the SiC sample was removed and the signal going through the hole was measured. The transmittance of the SiC sample was then calculated by taking the ratio of the transmitted signal through the SiC sample to the transmitted signal going through the aperture. The results were compared with the FTIR transmittance measurements for the same sample. The transmittance of SiC is shown in Figure 3.14, where the blue dashed line is the

transmittance from the MORT microscope and the red solid line is the FTIR measured reflectance and the results are in agreement.

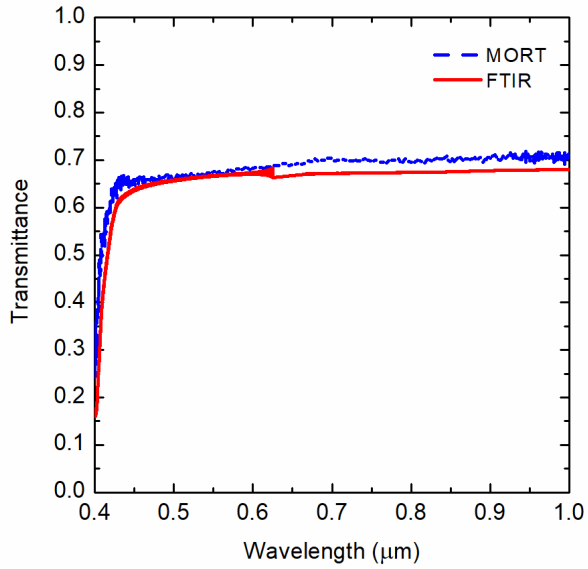

Figure 3.14. Comparison of transmittance of a SiC sample between MORT vs FTIR.

The spot size that the MORT microscope can measure was determined using an image from its CMOS camera. The image was imported into a MATLAB code to find the full width at half maximum of the pixel intensities. As can be seen from Figure 3.15, the maximum pixel intensity is 199. The image shown is for a 10X objective and the number of pixels that represent the full width at half maximum is ~1108, with each pixel equal to 3.6 μm. This means that the spot size is 1108 pixels × 3.6 μm/pixel /10X magnification = 400 μm. If the objective used is changed to 4X or 20X, the spot sizes would change to 998 μm or 200 μm, respectively.

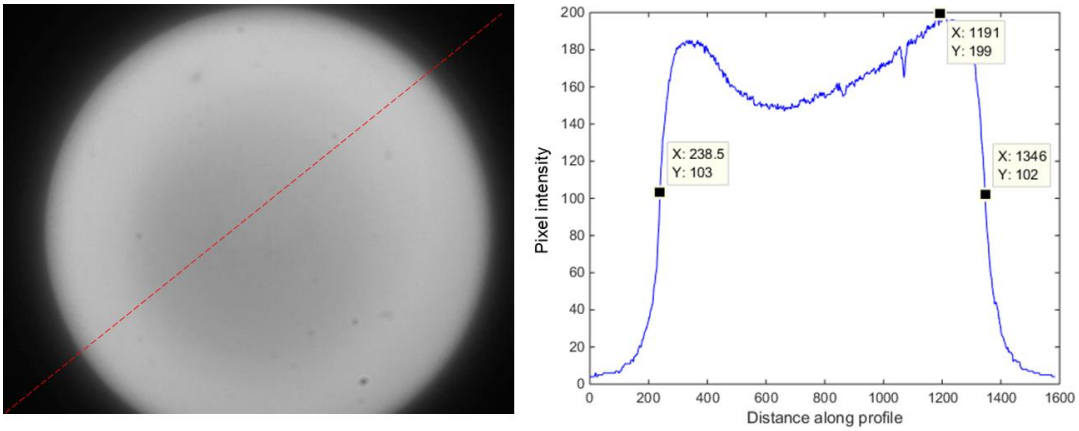

Figure 3.15. MORT beam spot determination.

3.4 Measured Radiative Properties of the Aluminum Nanodisc Absorbers

Figure 3.16(a) shows the measured spectral reflectance of the fabricated AlNDs with different heights. It can be seen that the reflectance dip red-shifts when increasing the AlND height. Another reflectance dip appears in the blue-wavelength range for AlNDs of 130 nm height. Figure 3.16(b) shows the images taken by the MORT microscope for different AlND heights. The colors of the images correspond to the wavelengths that are reflected the most by the AlNDs. The 50 nm AlNDs show a bright red color indicating its high reflectance, especially in the red-wavelength range. The 87 nm AlNDs show a darker red color indicating overall less reflected light with more of the reflected light occurring in the red-wavelength range. The 130 nm AlNDs show a green color indicating the reflectance peak occurring in the green-wavelength range. Therefore, we can see that adding the AlNDs to the aluminum substrate resulted in tunable narrow-band selective absorption and using a combination of these AlNDs with different heights would result in a broadband absorber that is easy and inexpensive to fabricate.

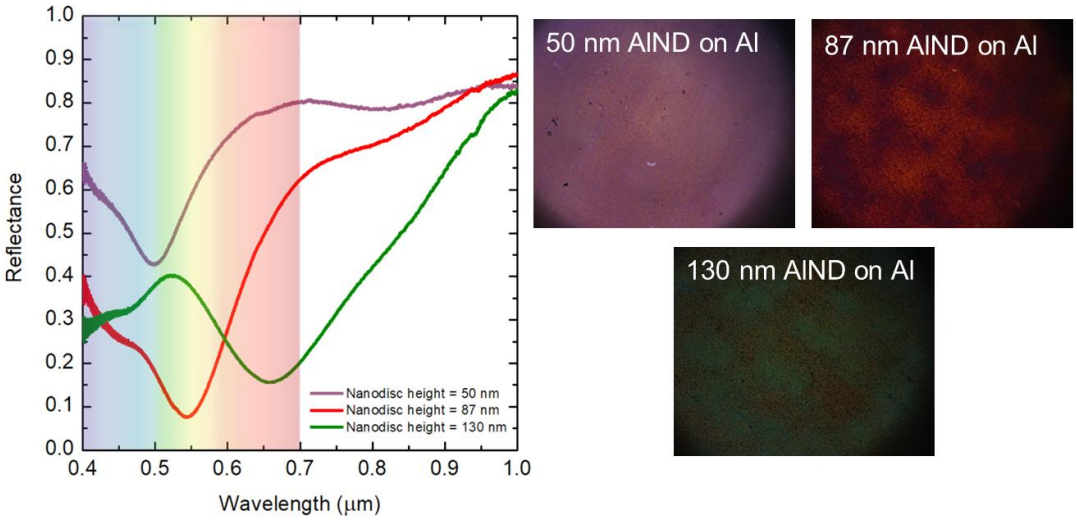

Figure 3.16. Measured reflectance of the AlND absorbers.

3.5 Simulated Radiative Properties of the Aluminum Nanodisc Absorbers

ANSYS HFSS software was used to simulate the AlNDs. An incident plane wave is incident on the structure with a wavelength from 400 nm to 1000 nm. Radiation boundary conditions are applied to the top and bottom surfaces of the air volume that surrounds the structure and master/slave boundary conditions surround a unit cell of the periodic structure. Reflectance of the structure is obtained by squaring the magnitude of the S11 parameter which represents the amount of the incident light that is reflected off the structure. The frequency that HFSS bases the mesh on is the maximum frequency of the spectral sweep, which is 750 THz in these simulations. The criterion for convergence in these simulations is based on the delta-S parameter. The delta-S parameter is the difference between the magnitude of the S11 parameters of the initial mesh and the refined mesh, at each frequency. A maximum delta-S of 0.005 was used for a minimum of four consecutive converged mesh refinement passes. Figure 3.17(a) shows the simulated spectral reflectance of the AlNDs for the different samples with different heights: 50 nm, 87 nm, and 130 nm.

The simulated results show that the reflectance dips that were observed in the measured reflectance results are present. However, these dips do not exactly match the measured results. Another difference between the simulated and measured results is the drop in the reflectance in the lower wavelengths region. Reasons for the differences between the simulated and measured results will be described in the following section.

To elucidate the cause of the reflectance dips, the electromagnetic (EM) fields at the dip wavelengths for different AlND heights were plotted, as shown in Figure 3.17(b). It can be seen that the magnetic field is confined in the gap between the AlNDs and a current loop is visible. This type of magnetic resonance response is characteristic of magnetic polariton (MP). It can also be seen that as the AlND height increases, the amount of confined energy in the gap between the AlNDs increases. The bottom right contour plot of Figure 3.17(b) shows the EM field at the 1st reflectance dip of the 130 nm AlND. From the EM field, it can be seen that the magnetic field is not confined in the gap but rather on top of the AlNDs which is a surface plasmon polariton (SPP) behavior.

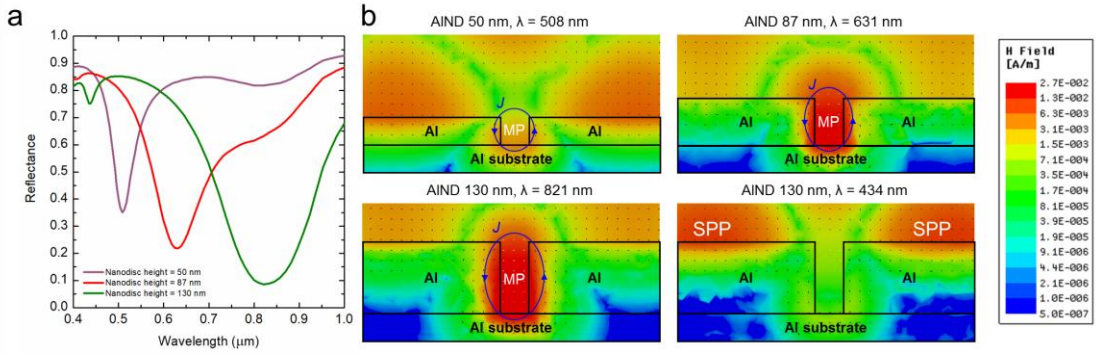

Figure 3.17. (a) Simulated reflectance of the AlND (b) EM fields at resonance wavelengths.

3.6 Factors Resulting in Difference Between Measured and Simulated Results

There are a number of factors that resulted in a difference between the simulated and measured reflectance results. These factors include: geometrical parameters such as the AlND diameter and height, the diffuse surface of the AlND absorber, and the incidence angle effect due to the MORT microscope objective's cone angle. Mainly, the discrepancy is a result of the samples being diffuse structures.

Since the AAO templates are not perfectly uniform, the resulting AlNDs will not have perfect discs with a fixed diameter. Therefore, to simulate the AlNDs, imaging software (FIJI) was used to find the filling factor of the AlNDs and calculate the average nanodisc diameter for each sample. The average diameter was different for each sample since the AAO templates do not exactly match their specified diameter but are rather within approximately ±5% of it. Figure 3.18 shows how the FIJI software was used to find the filling factor for one of the samples (130 nm AlND on Al). The average AlND diameters after this analysis were found to be 377 nm, 360 nm, and 405 nm for the AlND with heights 50 nm, 87 nm, and 130 nm, respectively.

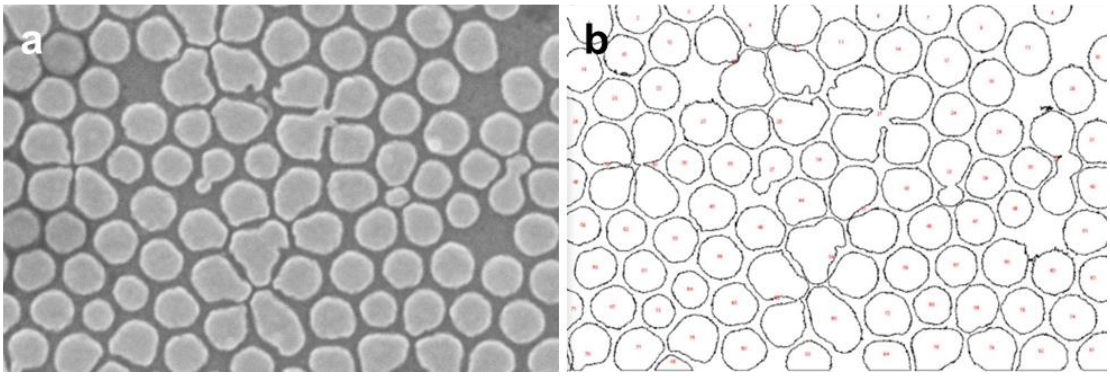

Figure 3.18. (a) SEM image of the 87 nm thick AlND sample. (b) Processed image from FIJI software to find the filling factor.

Another factor that is causing a difference between the simulated and measured reflectance results of the AlND absorbers is the thickness of the AlNDs. An atomic force microscope (AFM) was used to measure the actual thicknesses of the AlND. The tool was a Bruker Multimode-8 with a NCHV probe with a radius of curvature of 5 nm – 10 nm. The scan size was a 3 μm × 3 μm area with a scan rate of 1 Hz. Two scan areas were taken per sample and five AlNDs were measured per scan area and the average heights of the AlNDs were taken. The averaged heights were 61 nm for the “50” nm AlND sample, 96 nm for the “87” nm AlND sample, and 147 nm for the “130” nm AlND sample. This difference in AlND thickness would result in a difference in the resonance wavelength between the simulations and the measurements. Figure 3.19shows an AFM image of the “50” nm AlND on Al absorber. Appendix C shows additional images from the AFM measurement.

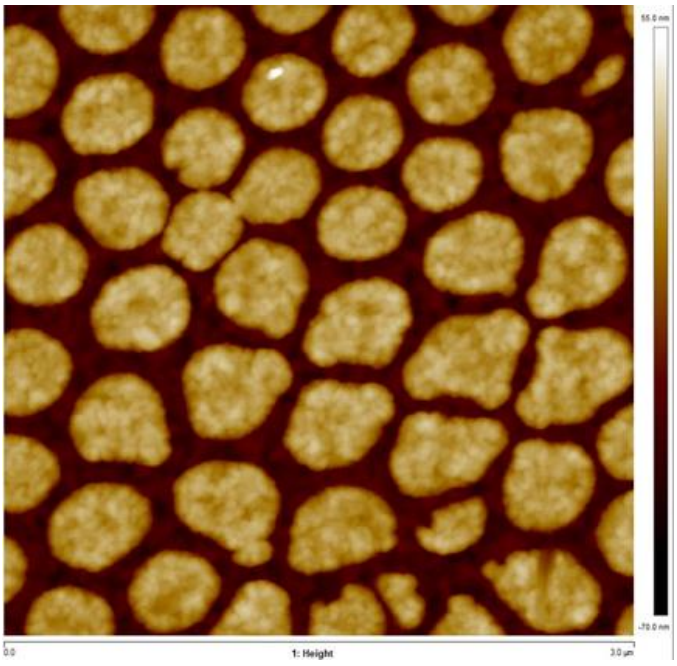

Figure 3.19. AFM image of the "50" nm AlND on Al absorber.

Since the AlND absorbers are diffuse structures, light is diffracted from the periodic structure. The angle at which the incident light is reflected due to diffraction is found using equation (3.1) , where θ_j is the j-th order angle of reflection, θ_i is the angle of incidence, λ is the wavelength, Δ is the period of the structure, and j is the order of diffraction. Figure 3.20 shows a plot of the angles of reflection for multiple incidence angles and for different diffraction orders. The y-axis represents the angle of reflection and the x-axis represents the angle of incidence. A value of j equal to zero represents specular reflectance. This reflectance is completely collected by the MORT microscope since any incident light on the sample will be reflected back into the objective at the same angle. However, for higher order diffraction, the reflected light is reflected at a different angle from the incidence angle according to equation (3.1). When $|j| \geq 1$ and the angle of reflection exceeds 90^o, the reflected light decays exponentially as an evanescent wave near the surface of the AlND periodic structure. It can be seen from Figure 3.20 for a j value of +1 and -1, the angle of reflection is between $\pm 40^o$ and $\pm 90^o$. However, the objective used by MORT is a 10X objective with a cone angle of 14.5^o. Therefore, the MORT microscope cannot collect the diffuse reflected light from the AlND absorbers leading to a drop in the measured reflectance.

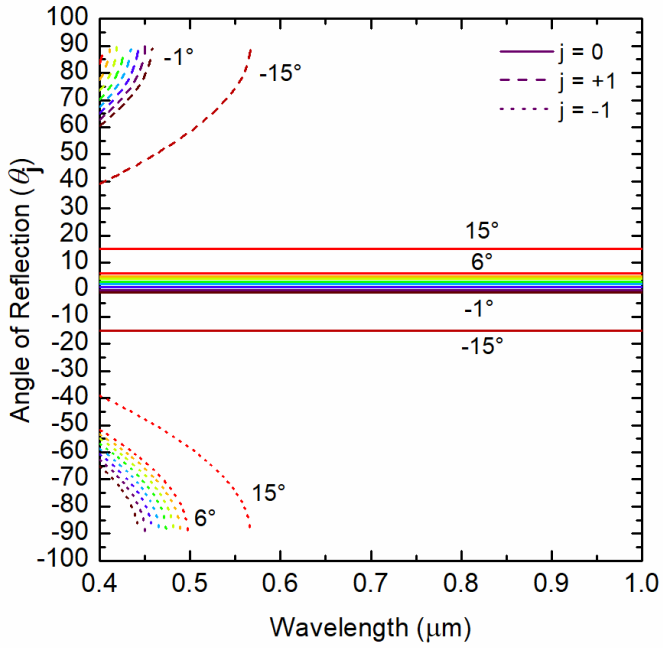

Figure 3.20. *j*-th order angle of reflection for multiple angles of incidence.

$$sin\,\theta_j = sin\,\theta_i + \frac{\lambda}{\Delta} j \tag{3.1}$$

A rigorous coupled-wave analysis (RCWA) was used to show the effect of the MORT microscope not being able to collect the higher-order reflectance waves. The sum of the reflectance waves is the hemispherical reflectance and the zeroth-order reflectance wave is the specular reflectance. The comparison example that RCWA was applied on was an aluminum 1D periodic grating. Figure 3.21 shows a comparison between the MORT measured reflectance of one of the AlND absorber samples (87 nm thick AlND), the RCWA calculated hemispherical reflectance, and the RCWA calculated specular reflectance, both of which had an incidence angle of zero degrees. It can be seen from Figure 3.21 that the zero-order reflectance in the blue-wavelength range is lower than the

hemispherical reflectance indicating that if the MORT microscope is mostly measuring specular or zero-order reflectance, then in the sub-period range for an incidence angle of zero degrees, the captured light would be significantly less than the hemispherical reflectance.

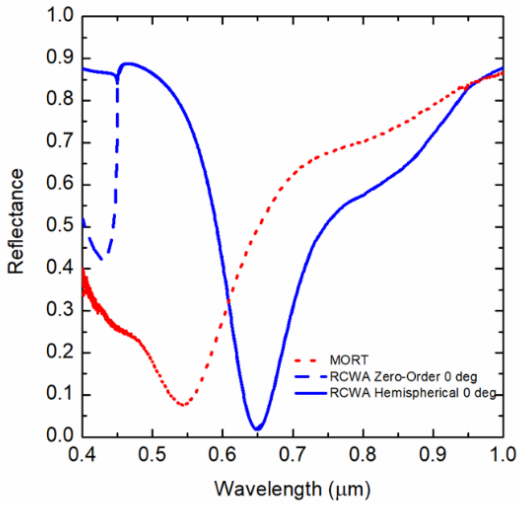

Figure 3.21. RCWA zero-order (specular) reflectance vs RCWA hemispherical reflectance.

The objective in MORT has a cone angle in which it can focus and collect light. This angle determines how much light can be captured as it is reflected off the sample being measured. Figure 3.22 shows the effect of the incidence angle on the SPP reflectance dip of a 1D grating periodic structure (again, using RCWA). The reflectance dip, which is in the shorter wavelength range, red-shifts as the incidence angle increases. This shift of reflectance dip with different wavelengths explains why the lowered reflectance, compared to the simulated hemispherical reflectance, extends beyond the sub-period wavelength range.

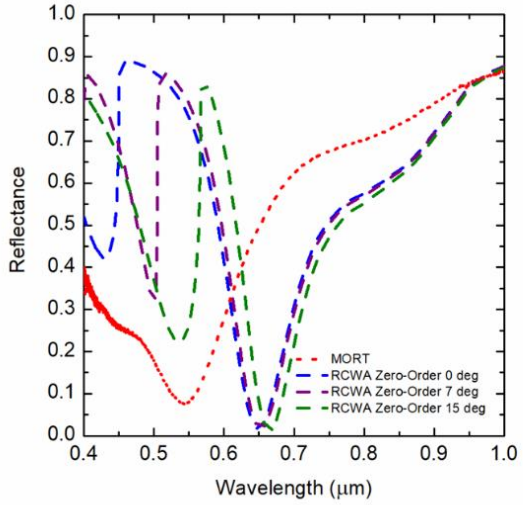

Figure 3.22. Incidence angle effect on the SPP resonance wavelength (87 nm AlNDs on Al).

To increase the absorption of the nanodiscs, dielectric layers have been used in multilayer structures to trap the incident light through multiple reflections [78, 79]. Combining the effects of the gap between the nanodiscs and the dielectric layer would lead to the structure exhibiting multiple reflectance dips resulting in multi-band absorbers. 50 nm thick SiO_2 was used as the dielectric layer and adding it led to an energy confinement in the dielectric SiO_2 in addition to the original confinement of energy between the AlNDs. Figure 3.23(a) shows the reflectance of the 50 nm AlND/ 100 nm SiO_2/ 200 nm opaque Al structure. It can be seen from the simulated reflectance of the structure that three reflectance dips exist. However, for the reflectance measured by MORT, only two reflectance dips are observed. To understand the cause of the three reflectance dips, the EM fields at the resonance dips are plotted in Figure 3.23(b). From the three EM plots, a confinement of

the EM field can be seen in the dielectric SiO_2 layer, while the confinement of energy in between the AlNDs is most apparent at 550 nm.

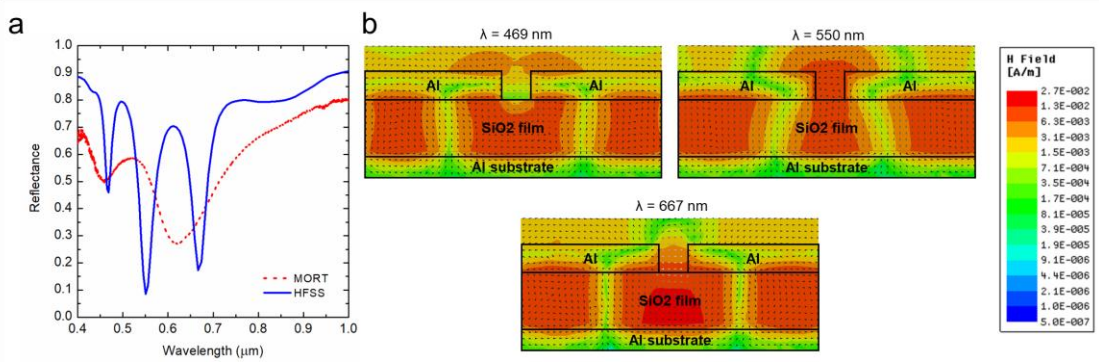

Figure 3.23. (a) Reflectance of the AlND/SiO2/Al structure (b) EM fields at resonance.

CHAPTER 4 SOLAR THERMAL CHARACTERIZATION OF SELECTIVE METAFILM ABSORBERS UNDER MULTIPLE SOLAR CONCENTRATIONS

In this chapter, the solar-to-thermal performance of solar thermal absorbers was characterized experimentally via a lab-scale experiment setup that measures the steady-state temperature of solar thermal absorbers. The setup can be used to evaluate the performance of small-sized solar thermal absorbers under different solar concentrations through their measured steady-state temperatures. This temperature is lower than the stagnation due to the small size of the samples which leads to parasitic thermal losses when measuring the temperature. Therefore, the temperatures obtained from this experiment are not equal to the stagnation temperature, but serve as indicators of the absorber's potential performance. The absorbers tested in this work are a metafilm and a black absorber (Acktar Metal Velvet [80]) which is used for comparison. The absorbers' radiative properties were measured and their total absorptance and total emittance values were calculated. Furthermore, a heat transfer analysis of the experiment and a potential application (using a heat transfer fluid to transport energy) were conducted and the absorbers' solar-to-thermal theoretical and experimental efficiencies were calculated. Durability of the metafilm under the high temperature demands of CSP applications was also tested through thermal cycling tests under vacuum and ambient conditions. Finally, an analysis of the metafilm material cost was performed and a comparison was made with commercial solar coatings on a unit area basis.

4.1 Radiative Properties of Metafilm and Black Thermal Absorbers

Figure 4.1(a) shows the working principle of a solar thermal system. Sunlight is incident on the absorber, where most of the light is absorbed and a fraction gets reflected.

As the absorber heats up, heat is conducted to a heat transfer fluid which carries the thermal energy to other locations for potential applications such as steam generation for power applications. The solar absorber (metafilm) that was used for the experiment consists of a Fabry-Perot cavity (W-SiO_2-W) with two anti-reflective coatings on top (Si_3N_4 and SiO_2). The metafilm can be fabricated on a silicon substrate or alternatively it can be applied to a stainless-steel substrate, making it flexible and durable. The metafilm's bottom three layers (W-SiO_2-W) were deposited by sputtering and the top two layers (Si_3N_4 and SiO_2) were deposited by remote plasma chemical vapor deposition. Figure 4.1(b) shows the metafilm's specular spectral directional reflectance for a wavelength range from 0.4 μm to 20 μm, characterized using a Fourier Transform Infrared spectrometer (FTIR from Thermo Scientific, iS50), compared with a black absorber and an ideal absorber. The heated label in the legend indicates that the absorber had tested with the solar thermal experiment and heated under 20.3 suns in vacuum. Also plotted is the metafilm's theoretical reflectance, which is based on the thicknesses obtained from a scanning electron microscope image (SEM) of the metafilm on silicon shown in the inset of Figure 4.1(b). Note that an SEM image of the metafilm on stainless steel was difficult to obtain due to the rough nature of the steel substrate. Moreover, the standard total solar irradiance spectrum (AM1.5) [81] and the blackbody emission spectrum (at 500^{o}C) are also plotted. It can be seen from the plot that the metafilm is selectively absorbing with a low reflectance in the solar spectrums (VIS and NIR ranges) and high reflectance in the mid-IR range, where most of the thermal radiative loss would occur. Since the absorber is opaque, its total absorptance is $A = 1 - R$. This leads to a total absorptance, α, of 0.910. A black absorber is used for comparison since most CSP plants utilize absorbers with broadband near-zero reflectance, such as

Pyromark 2500 which is similar to the black absorber in its radiative properties. From the figure, it can be seen that the black absorber does, in fact, have near-zero reflectance throughout the VIS, NIR, and mid-IR ranges, as reported by the manufacturer [80]. It is also observed that the reflectance of the unheated black absorber starts to increase past 10 μm, which agrees with the vendor's measurements [80]. However, for the heated black absorber, this effect is not observed and the black absorber retains its near-zero reflectance even past 10 μm. The calculated absorptance of the black absorber is 0.998. It can be seen from the plot that the metafilm is selectively absorbing with a low reflectance in the solar spectrum (VIS and NIR range) and high reflectance in the mid-IR range, where most of the thermal radiative loss would occur. An ideal absorber's reflectance is also plotted. An ideal absorber is one with zero reflectance (unity emittance) in the solar spectrum and unity reflectance (zero emittance) in the thermal emittance region. However, if the absorber is operating at a temperature where the two wavelength ranges overlap, then an optimum cutoff should be calculated where the solar spectrum intensity drops below the blackbody intensity. For a blackbody at 500^{o}C, this wavelength is 1.7 μm.

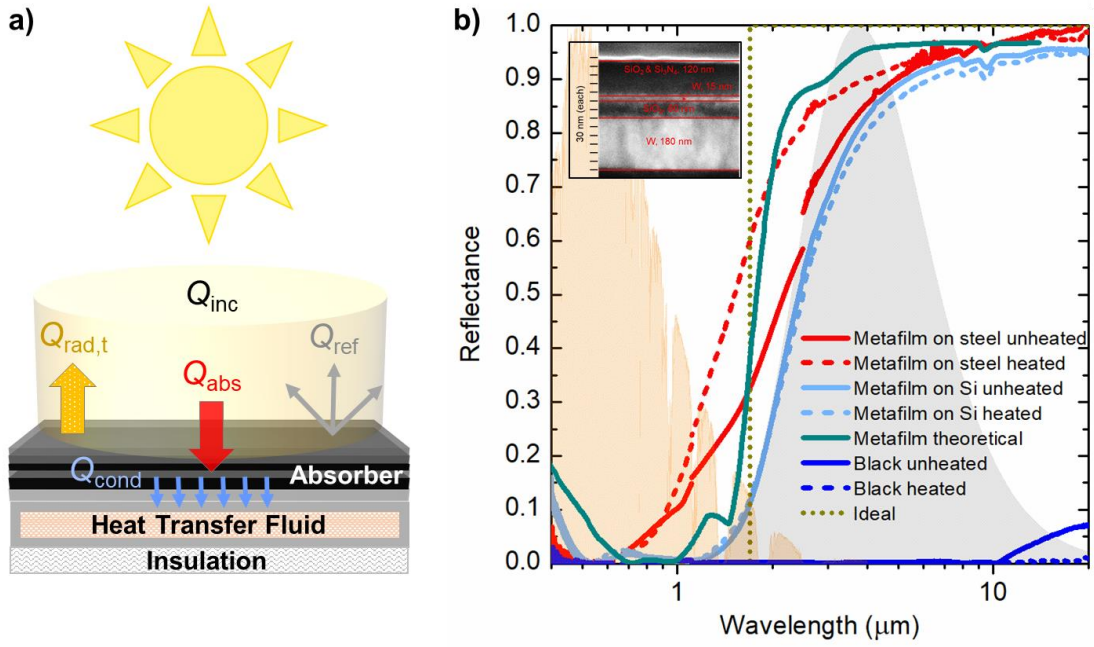

Figure 4.1. (a) Schematic to show the working principle of a solar thermal system. (b) Reflectance of the metafilm measured using an FTIR. The metafilm's theoretical reflectance, a black absorber's measured reflectance, and an ideal absorber's theoretical reflectance are also plotted for comparison. An SEM image of the metafilm on silicon is shown in the inset.

Hemispherical and diffuse reflectance measurements were also conducted for the metafilm and the black absorber using a tunable light source (Newport, TLS-250QU) and an integrating sphere (Labsphere, CSTM-R/T). As can be seen from Figure 4.2, the metafilm is highly specular and the black absorber is confirmed to have near-zero reflectance. Hemispherical and specular reflectance measurements were conducted for the back sides of the metafilm (stainless-steel) and the black absorber (aluminum). Moreover, the reflectance of the thermal paste that was used to attach the resistance temperature detectors (RTD) to the samples was also measured. However, since the thermal paste is not

flat, the specular reflectance measurement was not possible. Instead, only the hemispherical reflectance measurements were conducted for the thermal paste. The results are shown in figure. The IR-range hemispherical reflectance measurements were done to find the emittance of the samples. Note that the IR-range integrating sphere measurements were conducted through a different setup in collaboration with the Lawrence Berkeley National Laboratory.

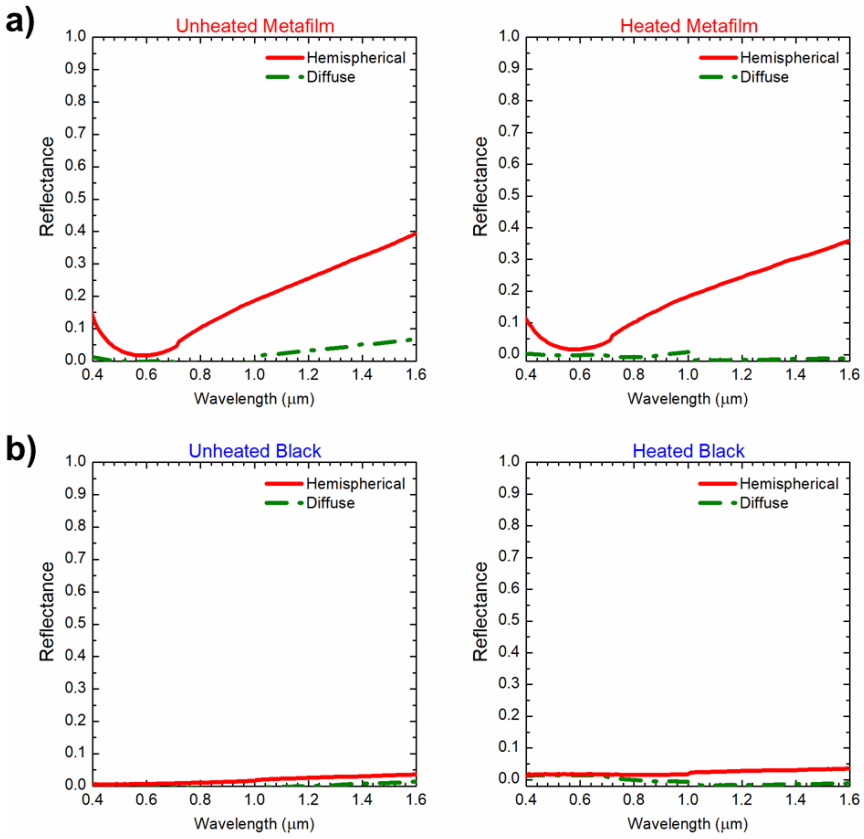

Figure 4.2. Hemispherical and diffuse measurements of the metafilm and black absorbers.

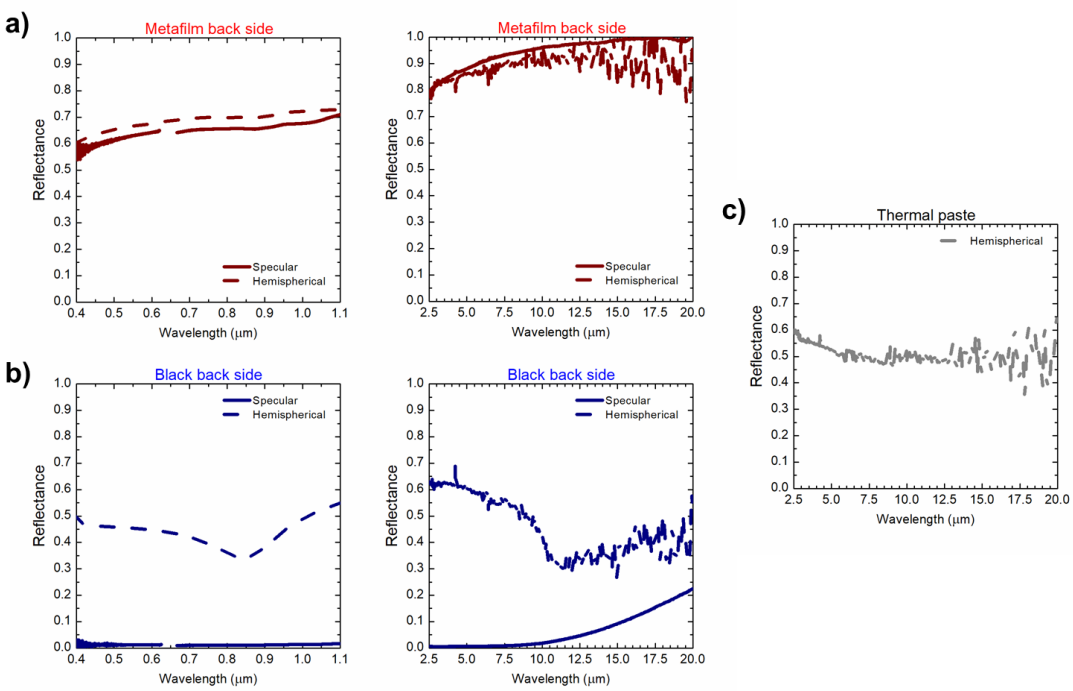

Figure 4.3. Specular and hemispherical measured reflectances of the (a) metafilm back side (stainless-steel), (b) the black absorber's back side (aluminum), and (c) the thermal paste.

4.2 Lab-Scale Solar Thermal Characterization Platform with Multiple Suns

The solar thermal experiment setup starts with a 1 KW xenon arc lamp (Newport 6271 in a Newport 66921 housing) that is used as a solar simulator. The lamp is connected to a power source (Newport, OPS-A1000) that is operated at a set power of 907 W. Light emitted from the lamp goes through neutral density filters (Newport UV fused silica metallic neutral density filters with transmittance values of 79.4%, 50.1%, 25.1%, and 10%) to control the concentration factor. Different combinations of these filters are used to achieve 1.5, 5.8, 10.0, and 20.3 suns and a fan is used to cool down the filters to reduce their temperature and minimize coating deterioration. An AM1.5 (Newport, 81094) filter

is then used to simulate solar conditions. The absorber holder along with a focusing setup is placed in a vacuum chamber (Kurt J. Lesker). The light goes through the vacuum chamber and is focused to a ~10 mm diameter spot. Additionally, an iris (Thorlabs, ID36) is used to ensure the 10 mm diameter beam spot. The absorber, which is an approximately 0.5" × 0.5" square, is attached to an RTD (Omega, F2020-100-B-100) via thermally conductive paste (Aremco, Pyro-Duct 597-A). The RTD is then connected to a temperature monitor (MYPIN, TA4) to measure the absorber's temperature. Figure 4.4 shows an image of the experiment setup. A power sensor (Thorlabs, S310C) was used to measure the intensity of the light incident on the absorber. The thermal power sensor is used with a power meter (Thorlabs, PM100D). Moreover, the ambient temperature is monitored by a thermocouple (Omega, 5TC-TT-K-30-36) placed inside the vacuum chamber that is connected to an additional temperature monitor (Vichy, VC99). The absorber steady-state temperatures were measured under a vacuum pressure of $\leq 4\times10\text{-}4$ Torr and under multiple concentration factors. Vacuum was attained by a turbo vacuum pump (Agilent, TPS-compact). Note that the RTD has a temperature limit of 500^{o}C which limited the experiment from going beyond 20.3 suns. Moreover, the black absorber has a temperature limit of 400^{o}C in the short-term and 350^{o}C in the long-term. The absorber was only subjected to temperatures higher than 350^{o}C for less than 20 minutes. Also, note that the actual absorber areas (used in the heat transfer analysis) were measured with a caliper, and since the absorbers were not exact squares, the average side length was used to measure their areas. A similar approach was used to find the area of thermal paste by assuming that the paste's irregular shape was confined within a square which was used for the area

calculation. The experiment was repeated three times each for two absorbers: the metafilm and the black absorber (Acktar, Metal Velvet [80]).

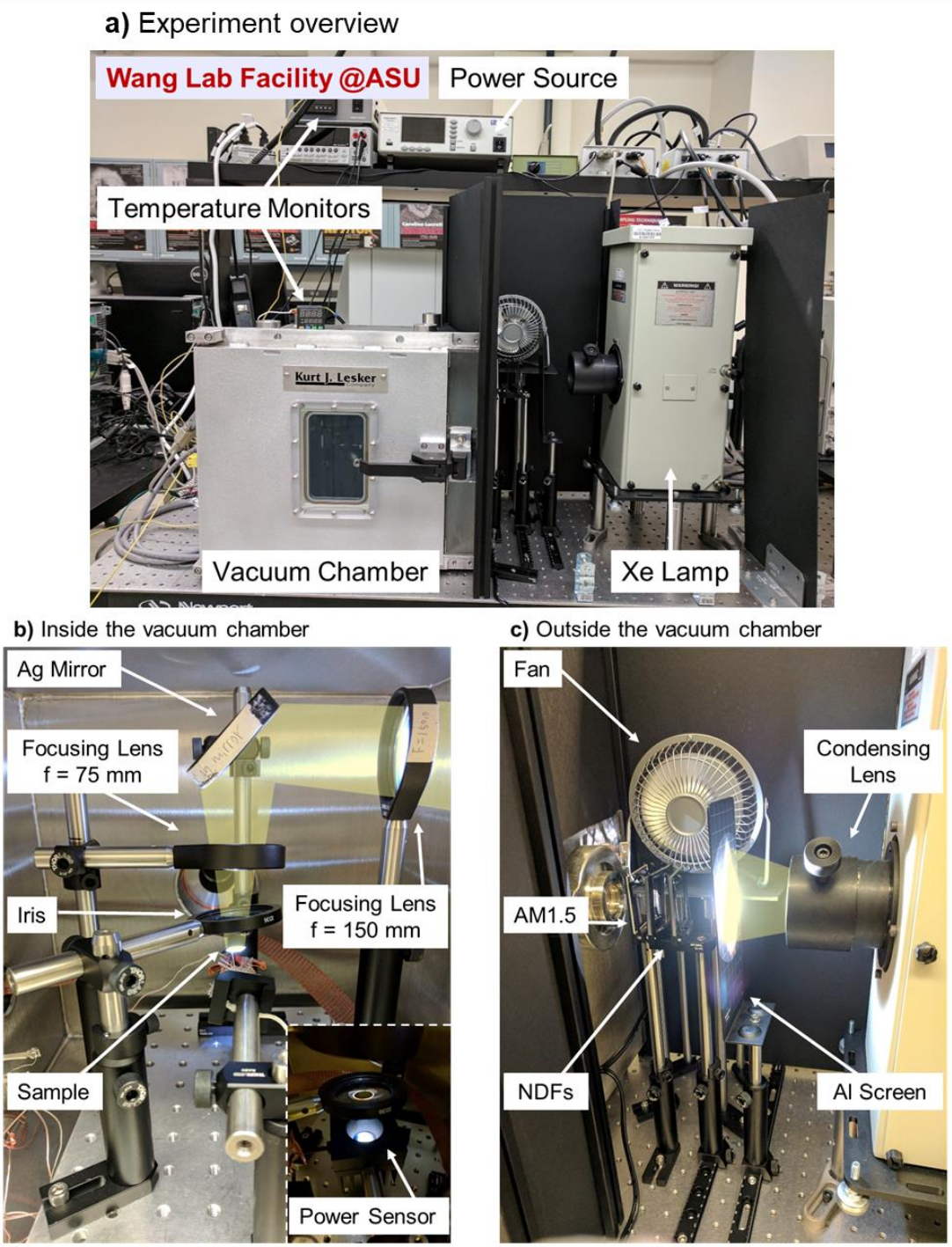

Figure 4.4. (a) Experiment setup overview of the solar thermal absorber steady-state measurement platform. (b) & (c) Detailed experiment setup of the platform.

A schematic of the experiment setup is shown in Figure 4.5(a). The setup can be used to test solar absorbers that are 0.5” × 0.5” in size under 1.5, 5.8, 10.0, and 20.3 suns. A xenon arc lamp along with an AM1.5 filter and multiple neutral density filters are used to simulate the different solar concentrations. Moreover, focusing lenses and an iris are used to achieve the small beam size. Finally, a resistance temperature detector (RTD) connected to a temperature controller is used to measure the absorber temperature. The results of the steady-state temperature experiment for 1.5 suns are shown in Figure 4.5(b) for the metafilm and the black absorber. The experiments were conducted under a vacuum pressure of $P \leq 4\times10^{-4}$ Torr to minimize thermal convection losses that would lead to reduced steady-state temperatures. The metafilm outperformed the black absorber, reaching a steady-state temperature of 123^{o}C, whereas the black absorber only achieved a steady-state temperature of 86.6^{o}C. Figure 4.5(c) shows the steady-state temperatures under different concentrations. The plot shows three measurements for each concentration factor and absorber which show very consistent results as can be seen from the error bars. It can be seen that the metafilm outperforms the black absorber at every concentration factor due to its low emittance in the infrared range, especially at high concentrations when the higher temperatures lead to higher radiation losses from the black absorber, which leads to lower steady-state temperatures. This is especially important since the most common commercial absorber for CSP systems is a black absorber called Pyromark 2500 which also exhibits high emittance in the infrared region. The metafilm, however, is low-emitting in the same region, which would result in higher temperatures for the same concentration. The metafilm reached a steady-state temperature of 500^{o}C at a concentration factor of 20.3 suns, while the black absorber reached a steady-state temperature of 375^{o}C at the same

concentration factor. The inset of Figure 4.5(c) shows images of the tested absorber samples.

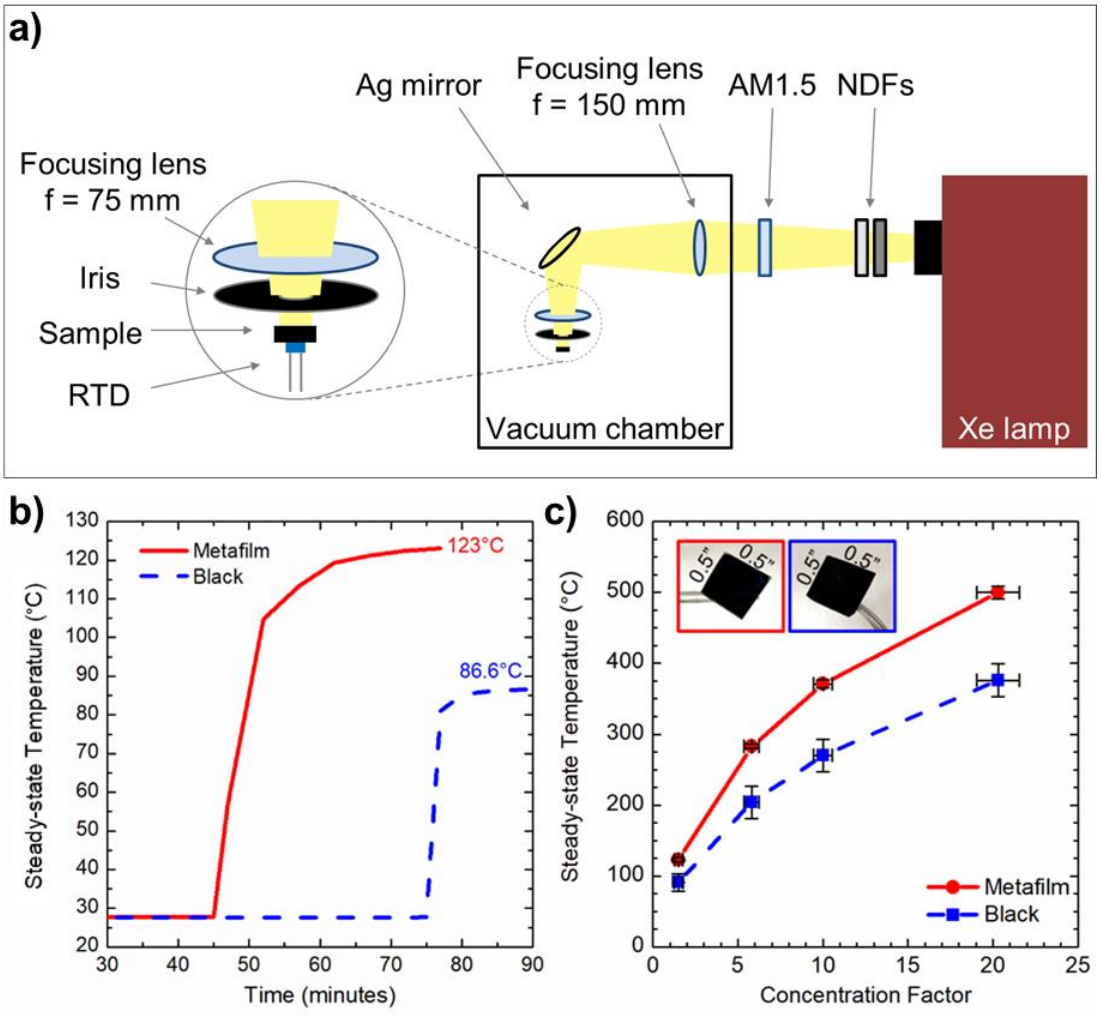

Figure 4.5. Schematic of the steady-state temperature experiment setup. b) Steady-state temperatures for the solar thermal experiments of the metafilm and black absorbers under 1.5 suns. c) Steady-state temperatures under multiple suns. The tested absorber samples are shown in the inset of panel c.

4.3 Heat Transfer Model and Solar-to-Thermal Efficiency Analysis

A heat transfer model was developed to verify the experimental results and help elucidate the heat transfer mechanisms involved in the solar thermal experiments. Incident radiation, Q_{inc}, strikes the absorber where most of this energy, Q_{abs}, is absorbed since the sample total absorptance, α_t, is very high in the solar spectrum. Equation (4.1) describes the absorbed energy where A is the surface area, C is the concentration factor, and G is the solar constant (1000 W/m^2). The absorbed energy is then converted to different heat transfer modes. These modes include radiation loss, Q_{rad}, from the top and bottom of the absorber, where A is the surface area, ε is the total emittance, radiation loss from the thermal paste, and conduction loss through the RTD pins, Q_{cond}, where R_{cond} is the conduction resistance. The equations expressing these quantities are listed below and the parameters used in this heat transfer analysis are listed in Table 4.1. Note that in this analysis, the steady-state absorber temperature is T_s, the ambient temperature, T_∞, is 20^{o}C, and the absorbers are approximately 0.5" × 0.5" in size.

$$Q_{abs} = A_t \alpha_t C G \tag{4.1}$$

$$Q_{rad} = A\varepsilon\sigma({T_s}^4 - {T_\infty}^4) \tag{4.2}$$

$$Q_{cond} = (T_s - T_\infty)/R_{cond} \tag{4.3}$$

To find the total emittance, ε, equation (4.4) was used, where $R^{\frown}$ is the hemispherical reflectance. The hemispherical data was obtained via the integrating sphere reflectance measurements. Note that the temperature-dependent emittance values of the tested solar absorbers are plotted in Figure 4.6. The heat transfer equations were then used

to find the heat transfer modes and the solar-to-thermal conversion efficiency of the metafilm as well as the black absorber for comparison.

$$\varepsilon'_{\lambda,N} = \alpha'_{\lambda,N} = 1 - R^{\frown}_{\lambda,N} \tag{4.4}$$

Table 4.1. Material properties used in heat transfer analysis, where α is absorptance and ε is total emittance.

Black Absorber	Area, A (cm^2)	α	ε 1.5 suns 91.3°C	ε 5.8 suns 203.8°C	ε 10.0 suns 270.3°C	ε 20.3 suns 375.5°C
Top, *t*	2.02	0.998	0.922	0.930	0.932	0.934
Thermal paste, *p*	1.14	NA	0.501	0.495	0.491	0.484
Bottom (aluminum), *b*	0.878	NA	0.548	0.507	0.488	0.464
Side (aluminum), *s*	0.061	NA	0.548	0.507	0.488	0.464

Metafilm Absorber	Area, A (cm^2)	α	ε 1.5 suns 123.2°C	ε 5.8 suns 283.2°C	ε 10.0 suns 370.5°C	ε 20.3 suns 499.5°C
Top, *t*	1.76	0.910	0.046	0.068	0.082	0.100
Thermal paste, *p*	0.626	NA	0.500	0.490	0.484	0.477
Bottom (stainless-steel), *b*	1.14	NA	0.104	0.118	0.126	0.135
Side (stainless-steel), *s*	0.454	NA	0.104	0.118	0.126	0.135

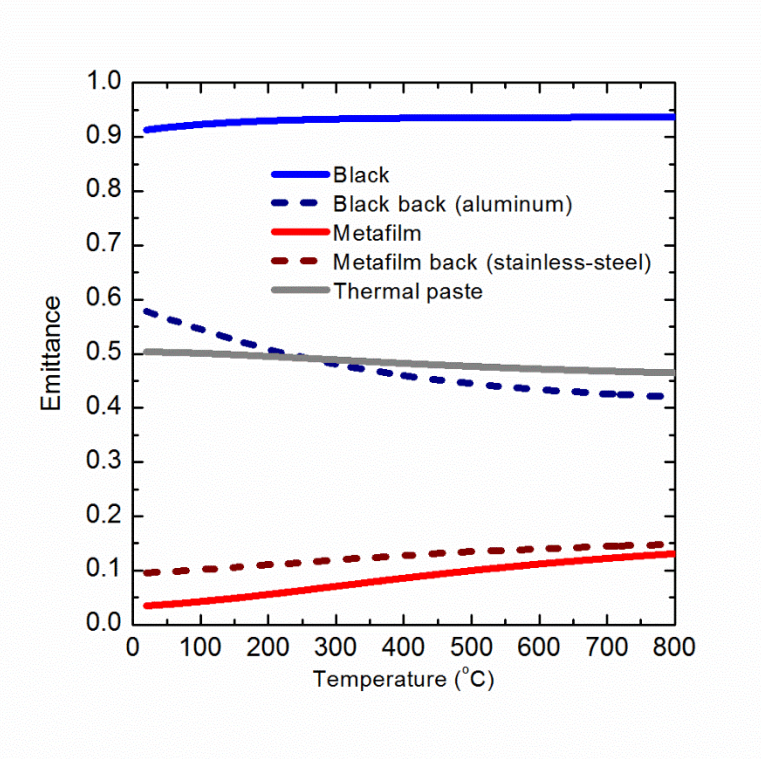

Figure 4.6. Temperature-dependent emittance of the thermally emitting surfaces of the tested absorbers.

The pie charts in Figure 4.7(a) show the percentage of the absorbed heat that is converted to wasted energy (radiation) or potentially useful energy (conduction). It can be seen that for the black absorber, most of the thermal loss is due to radiation from the top surface of the absorber. This is because the black absorber has extremely high emittance across the thermal range. However, for the metafilm, the top surface radiation loss is minimal in comparison due to the metafilm's extremely low total emittance. Note that in the case of the metafilm, the thermal paste radiation loss is significant (~25% of the absorbed energy). However, in a full-sized application of the absorber in a solar collector, radiation loss from thermal paste would be insignificant. Therefore, a heat transfer analysis of a projected application is conducted, where the thermal paste is removed along with the

temperature sensors. Instead, a thermally insulated tube filled with a high-temperature heat transfer fluid would be used. Figure 4.7(b) shows a schematic of the projected application. The pie charts of Figure 4.7(b) show the resulting heat transfer modes of this application. Note that the paste radiation loss is now eliminated and the potentially useful energy (conduction) is dominant, more significantly in the case of the metafilm, leading to a higher solar-to-thermal conversion efficiency, η.

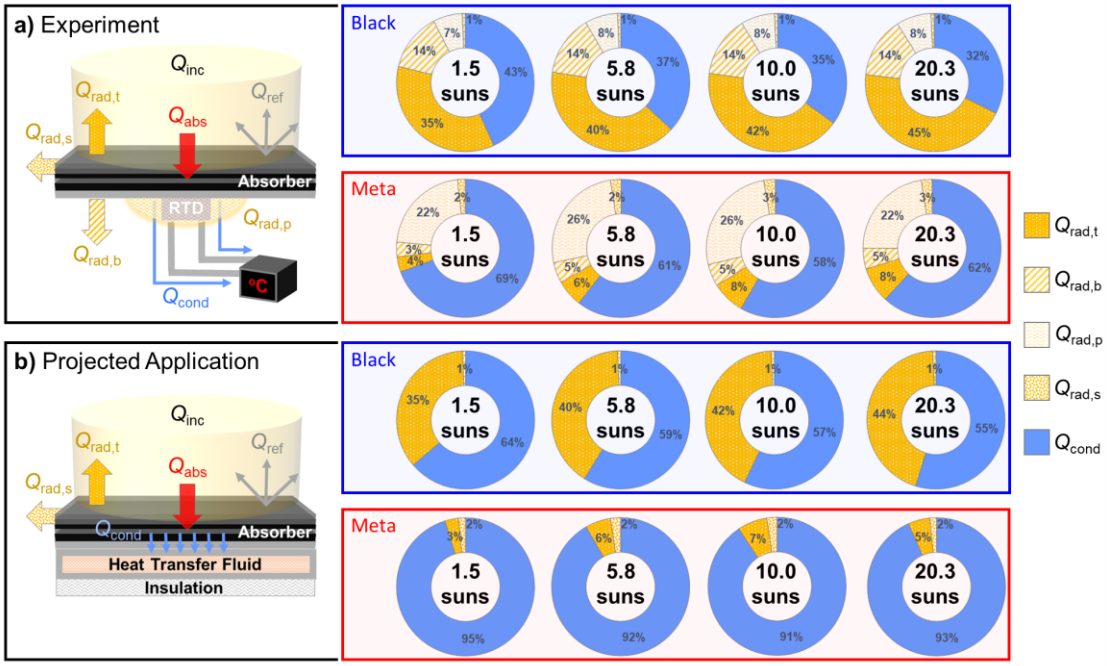

Figure 4.7. Heat transfer modes schematic and percentage of the absorbed heat converted to different heat transfer modes under different concentrations for the metafilm and the black absorber. Panel (a) refers to the experiment and panel (b) refers to a potential application of the absorber and how it would affect heat transfer.

The solar-to-thermal conversion efficiency, η, of the metafilm was calculated based on the previous heat transfer model using equation (4.5) and equation (4.6). Equation (4.5) is used to calculate the curves of Figure 4.8 which represent the theoretical solar-to-thermal

efficiencies, η_{theo} at different concentration factors, whereas, equation (4.6) is used to calculate the experimental solar-to-thermal efficiencies, η_{exp}, corresponding to the measured steady-state temperatures for different concentration factors. The experimental efficiencies represent the mean efficiency from three measurements and the appropriate error bars are plotted. Note that the absorptance and emittance values used for these calculations (shown in Table 4.1) are all based on measurements of unheated absorbers. Figure 4.8(a) is for the metafilm, Figure 4.8(b) is for the black absorber, and Figure 4.8(c) is for an ideal absorber. Note that the areas used for the top and bottom surfaces of the ideal absorber calculation are 0.5" × 0.5" where half the bottom side was assumed to be covered with thermal paste and the other half was assumed to have zero emittance. The thickness used for the side area calculation was the thickness of the metafilm (8 mm). Note that in this experiment, there is not a direct way of measuring conduction loss, and therefore, there is no way of directly calculating η_{exp} Therefore, the black absorber is used as a calibration absorber to calculate the η_{exp} for the metafilm. This is done by first assuming that for the black absorber, η_{theo} is equal to η_{exp}. Then, η_{exp} for the black absorber is used to calculate R_{cond} for each of its steady-state temperatures under different suns and a linear fit is obtained. The linear fit can be found in the supplemental material. Further, the linear fit is used to calculate R_{cond} for the metafilm measured steady-state temperatures. This is based on the assumption that R_{cond} is the same for both absorbers. Finally, equation (4.6) is used to calculate the η_{exp} of the metafilm. It can be seen that the heat transfer model is successful in predicting η of the absorbers, since there is reasonable agreement between the η_{exp} and the η_{theo}. It can also be seen that the metafilm has generally higher η compared to the black absorber and is closer in performance to the ideal absorber. From Figure 4.8, it can be seen

that under 10 suns, η_{exp} is 57.1% at 371°C whereas for the black absorber, it is 34.9% at 270°C. The black absorber only has higher η at lower temperatures, due to its low radiation losses and high absorptance in that range. Note that at 20.3 suns, the metafilm reaches the RTD temperature limit (500°C) and therefore, the temperature reading is inaccurate, leading to the divergence of the η_{exp} from the η_{theo}. The uncertainty analysis used to find the error bars is discussed next.

$$\eta_{\text{theo}} = \frac{Q_{\text{abs}} - \sum Q_{\text{rad}}}{Q_{\text{inc}}} \tag{4.5}$$

$$\eta_{\text{exp}} = \frac{Q_{\text{cond}}}{Q_{\text{inc}}} = \frac{T_s - T_\infty}{R_{\text{cond}} Q_{\text{inc}}} \tag{4.6}$$

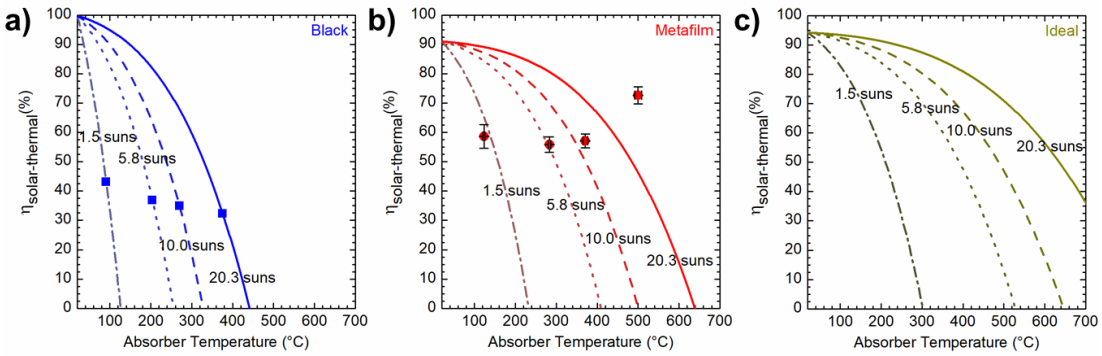

Figure 4.8. Solar-to-thermal conversion efficiencies of (a) black absorber, (b) metafilm, and (c) an ideal absorber. The curves represent the theoretical efficiencies and the points represent the experimental values for different concentration factors.

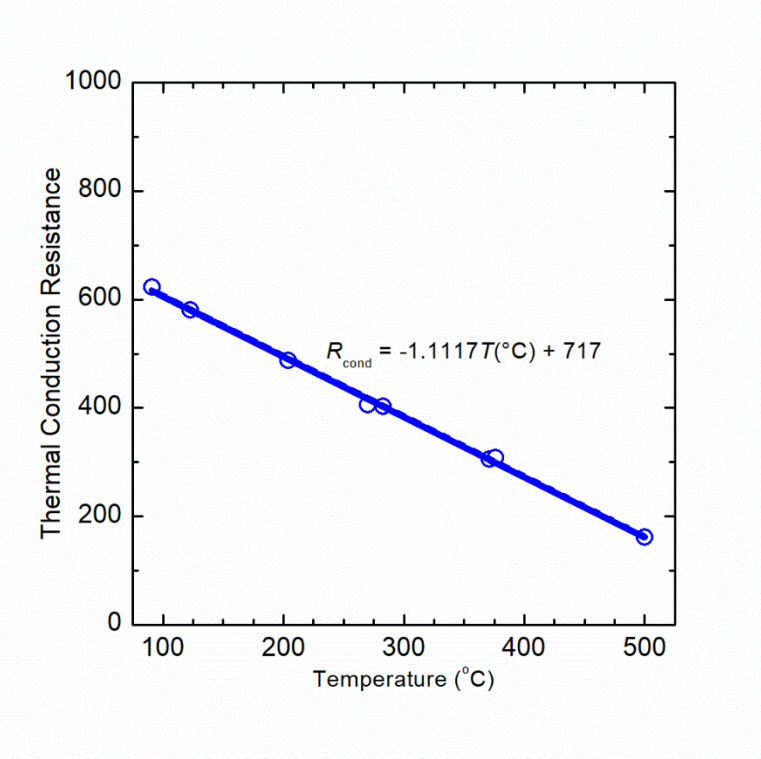

Figure 4.9. Temperature-dependent thermal conduction resistance (R_{cond}) found by using the experimental temperatures of the black absorber steady-state temperature test and using a linear fit to find R_{cond} for the metafilm.

The error bars in the experimental solar-to-thermal efficiency calculations were calculated by equations (4.7) through (4.15), where precision uncertainties as well as bias uncertainties come from the temperature and concentration factor (from the incident power) measurements. In equations (4.7) through (4.14), P_T is the precision uncertainty due to the temperature measurement, σ is the sample standard deviation, P_C is the precision uncertainty due to the concentration factor, B_T is the bias uncertainty due to the temperature measurement, T_{avg} is the average temperature in Celsius, B_C is the bias uncertainty due to the concentration factor, C_{avg} is the average concentration factor, B_η is the total bias uncertainty, and U is the combined uncertainty. Note that equation (4.13) was used for the

vertical error bars and equation (4.14) was used for the horizontal error bars. The error bars used for the calculation of the steady-state temperature vs concentration factor plot also uses the same equations below, but for the horizontal error bars, equation (4.15) is used.

$$P_{\mathrm{T}} = 3\sigma(T_{avg}) \tag{4.7}$$

$$P_{\mathrm{C}} = 3\sigma(C_{avg}) \tag{4.8}$$

$$P_{\eta} = \sqrt{(\frac{\partial_{\eta}}{\partial_{T}} P_{T})^{2} + (\frac{\partial_{\eta}}{\partial_{C}} P_{C})^{2}} \tag{4.9}$$

$$B_{\mathrm{T}} = 0.30 + 0.005(T_{avg} + 273) \tag{4.10}$$

$$B_{\mathrm{C}} = 0.05C_{avg} \tag{4.11}$$

$$B_{\eta} = \sqrt{(\frac{\partial_{\eta}}{\partial_{T}} B_{T})^{2} + (\frac{\partial_{\eta}}{\partial_{C}} B_{C})^{2}} \tag{4.12}$$

$$U_{\eta} = \sqrt{{P_{\eta}}^{2} + {B_{\eta}}^{2}} \tag{4.13}$$

$$U_{T} = \sqrt{{P_{T}}^{2} + {B_{T}}^{2}} \tag{4.14}$$

$$U_{C} = \sqrt{{P_{C}}^{2} + {B_{C}}^{2}} \tag{4.15}$$

4.4 Thermal Durability Test

Thermal cycling tests were performed on the metafilm to determine if it can handle the high temperatures that concentrating solar power applications require. Therefore, thermal cycling tests were performed in vacuum conditions at 600^{o}C and 700^{o}C for 5-hour

cycles. The current state-of-the art solar absorber for concentrating solar power parabolic troughs can handle a temperature of 580^{o}C [82]. A setup was built up inside a vacuum chamber to heat the metafilm in vacuum conditions. A Si_3N_4 heater was used. The heater can handle a temperature of 1000^{o}C and has a voltage rating of 110 V and a power rating of 150 W. Figure 4.10 shows a schematic and an image of the vacuum heating setup. The heater base was surrounded by thermally insulating material to minimize the conduction loss to the environment. The insulating material was covered with aluminum foil to minimize the radiation loss to the environment as the insulating material's temperature increased. A copper chip with a hole for a thermocouple was used to measure the temperature of the heated metafilm. Thermal paste was used between the copper chip and the heater to minimize contact resistance and increase the heat conducted to the copper chip and finally the metafilm. The metafilm was placed directly onto the copper chip and a piece of glass was placed on top of the metafilm. The purpose of the glass was to protect the surface of the metafilm coating from damage since the increased temperatures led to outgassing from the insulation material which coated some initial metafilm samples and altered their radiative properties.

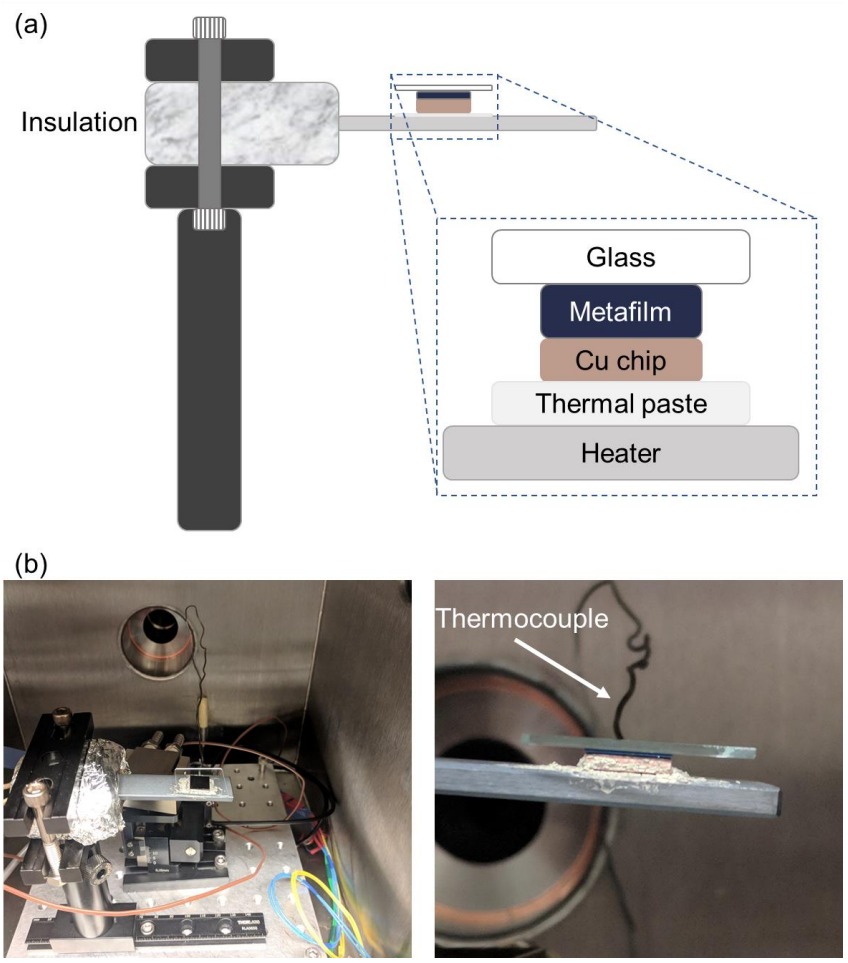

Figure 4.10. Vacuum thermal cycling testing setup.

Three heating and cooling cycles were conducted. The heating cycles lasted 5 hours each and the cooling cycles represent the time it took for the samples to return to room temperature, which was approximately a half hour. The thermal cycles were performed under a vacuum pressure lower than 5×10^{-4} hPa. After the heating cycle ends and the heater is turned off, the metafilm is left in the vacuum chamber to cool down until the temperature is less than 100^{o}C to avoid oxidation of the different parts of the setup. The vacuum pump is then turned off and the chamber is vented. After venting, the metafilm is removed and left to cool down to room temperature. Next, the reflectance of the metafilm was measured

in the visible, near-IR and the IR ranges using an FTIR. This was repeated for the second and third thermal cycling tests. The first set of thermal cycling tests were conducted at 600^{o}C and the reflectance of the metafilm after each of the tests is shown in Figure 4.11. To further test the temperature limit of the metafilm, another set of thermal cycling tests was conducted at 700^{o}C. The reflectance of the metafilm after this second round of tests is plotted in Figure 4.11. It can be seen from both figures that the reflectance of the metafilm does not significantly change which means that it can handle the high temperature demands of concentrating solar power in vacuum conditions. Figure 4.12 shows the experimental settings for the three 600^{o}C thermal cycling tests and Figure 4.13 shows the settings for the 700^{o}C ones. Note that additional thermal cycling tests at higher temperatures were not conducted since the heater was operating close to its limits and increasing the power input to the heater would lead to it getting damaged.

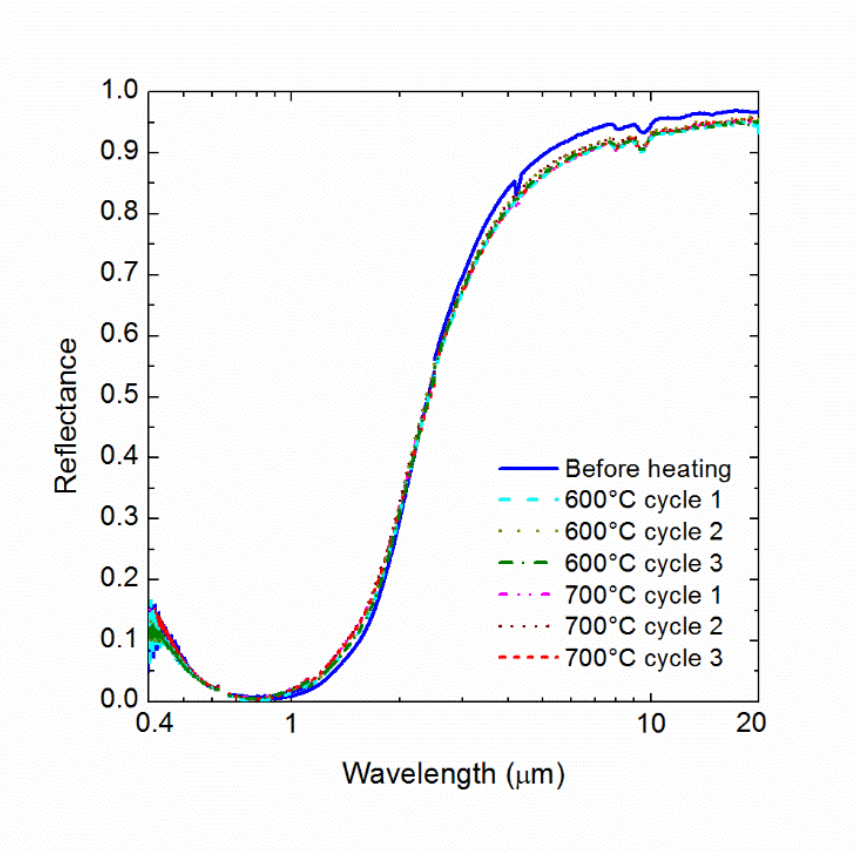

Figure 4.11. Reflectance of metafilm before and after thermal cycle tests at 600°C and 700°C.

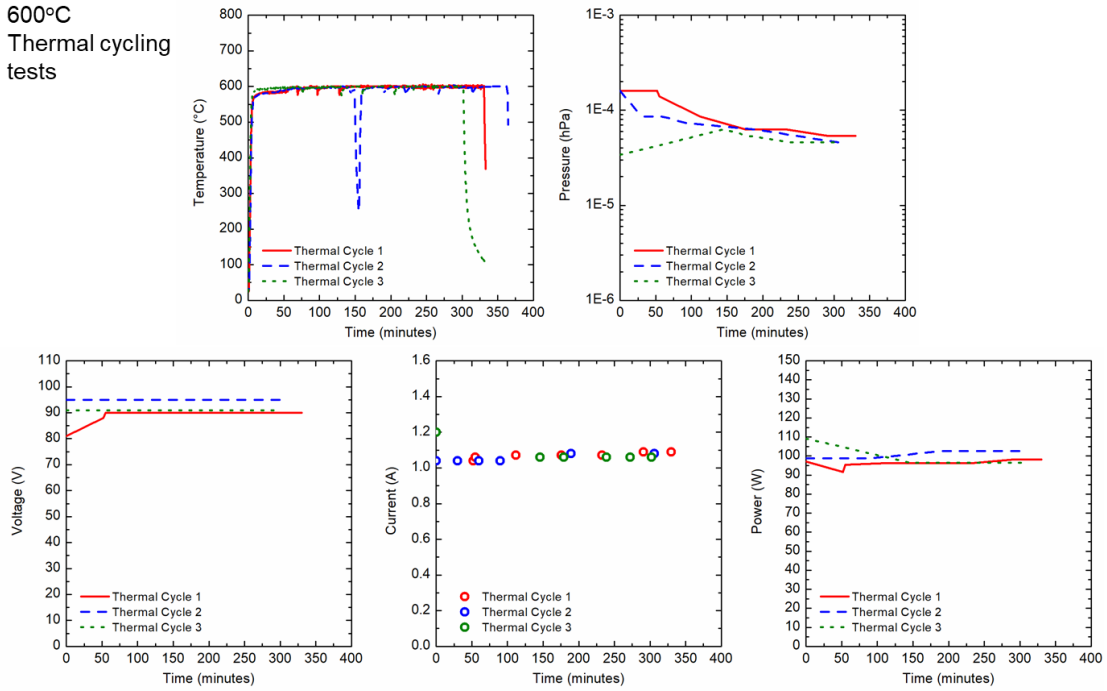

Figure 4.12. Experimental parameters used for vacuum 600ºC thermal cycling tests.

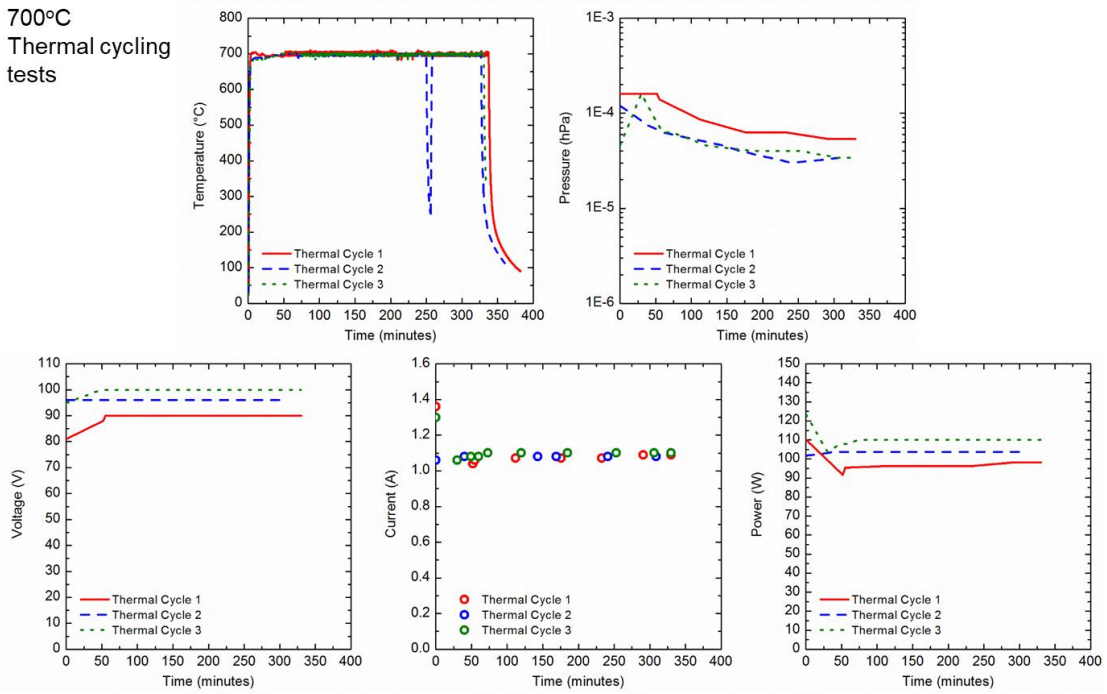

Figure 4.13. Experimental parameters used for vacuum 700ºC thermal cycling tests.

To test the durability of the metafilm in ambient conditions, a furnace was used. Thermal cycling tests were conducted at a temperature of 400°C and 500°C. The metafilm was placed in the furnace and the temperature of the furnace was set to 400°C and left to stabilize for a half hour. Then the metafilm was left for 12 hours at 400°C. Next, the furnace was turned off and the metafilm was left to cool for a minimum of two hours. The metafilm was then taken out of the furnace and its reflectance in the visible, near-IR, and IR ranges was measured using an FTIR. This was repeated for a total of three thermal cycles. Figure 4.14 shows the reflectance after each of the thermal cycles at 400°C. The metafilm reflectance did not significantly change after the tests. The tests were then repeated a higher temperature of 500°C. However, the metafilm was visibly damaged after the first cycle and its reflectance is plotted in Figure 4.14.

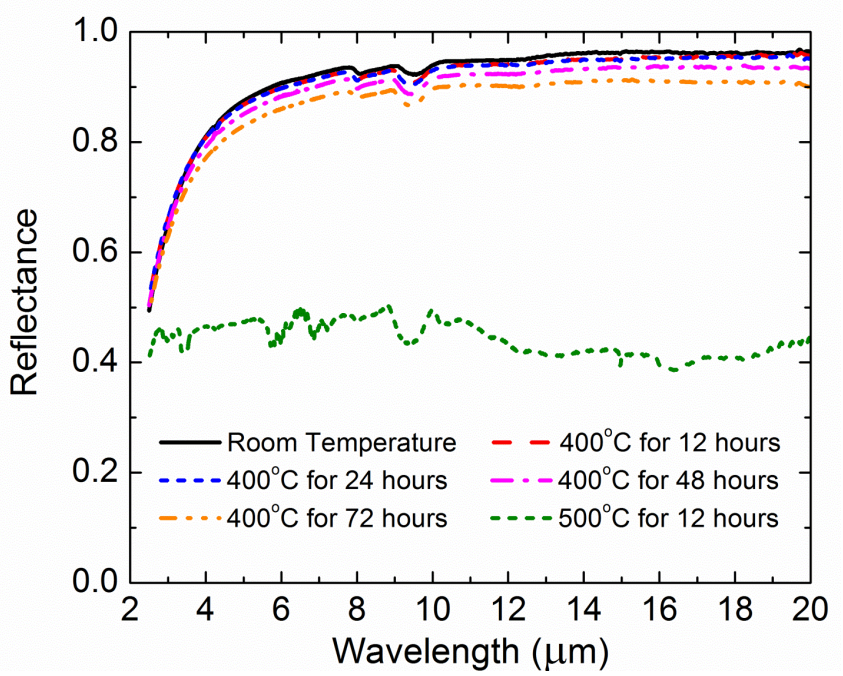

Figure 4.14. Reflectance before and after ambient 400°C and 500°C thermal cycling tests.

4.5 Cost Analysis

A cost analysis was conducted to compare the metafilm to other concentrating solar power coating materials. The metafilms that were developed were fabricated at ASU's facilities rather than commercial-scale setups. Therefore, a reasonable comparison of equipment costs as well as labor costs with commercial solar coatings cannot be made. Instead, an analysis of the metafilm's material costs was performed and the cost per unit area was compared to commercial concentrating solar power coatings. Table 4.2 shows a list of the metafilm's material costs. Note that for the top two layers of the metafilm, for which RPCVD was used, the cost was for a 4-inch wafer. However, since the metafilm's top two layers are ultrathin (73 nm for the SiO_2 layer and 50 nm for Si_3N_4 layer), the amount of gas needed to fabricate the top two layers is insignificant, as can be seen from Table 4.2. Therefore, we have assumed that the material cost per unit area for the top two layers to be effectively zero dollars ($\$4.85\times10^{-13}$ for the SiO_2 layer and $\$5.87\times10^{-13}$ for the Si_3N_4 layer). The cost of the bottom three layers, which were fabricated via sputtering was $2.22 per unit area. Therefore, the total materials cost of the metafilm is $2.22 per unit area. This is significantly less than the materials cost other solar coatings such as Pyromark, Co_3O_4, and LSM which cost $5.41, $50, and $100 per unit area, respectively [83, 84].

Table 4.2. Cost of materials of metafilm.

CVD							Sputtering			
Material	SiO2 (top)			Si3N4			Material	Tungsten thin film	SiO2 (cavity)	Tungsten substrate
Fabrication Technique	RPCVD			RPCVD			Fabrication Technique	DC Sputtering	RF Sputtering	DC Sputtering
Gas	He	SiH4	N2O	He	SiH4	NH3	Target Diameter (m)	0.1016	0.1524	0.1016
Thickness (m)	7.30E-08			5.00E-08			Target Thickness (m)	0.00635	0.00635	0.00635
Deposition Rate (Å/s)	1.1			0.7			Target Volume (m^3)	5.14815E-05	0.000115833	5.14815E-05
Deposition Time (s)	6.64E-09	6.64E-09	6.64E-09	7.14E-09	7.14E-09	7.14E-09	Target Cost ($)	$501.00	$295.00	$501.00
Flow Rate of Gas (m^3/s)	8.33E-06	2.50E-07	1.25E-06	1.67E-05	2.50E-07	1.22E-06	Cost per Pound ($/lb)	$228.71	$435.94	$228.71
Volume of Gas (m^3)	5.53E-14	1.66E-15	8.30E-15	1.19E-13	1.79E-15	8.69E-15	Density (lb/m^3)	42550	5842	42550
Density of Gas (kg/m^3)	0.18	1.34	1.98	0.18	1.34	0.73	Layer Thickness (m)	1.00E-08	7.10E-08	2.00E-07
Cost of Gas ($/kg)	$17.00	$40.00	$20.00	$17.00	$40.00	$4.00	Layer Area (m^2)	1	1	1
Total Cost of Gas (kg)	$0.00	$0.00	$0.00	$0.00	$0.00	$0.00	Layer Volume (m^3)	1.00E-08	7.10E-08	2.00E-07
Material Cost for a 4" Diameter Wafer($)	$0.00			$0.00			Material Cost for a 1 m^2 Absorber ($)	$0.10	$0.18	$1.95

CHAPTER 5 CONCLUSION AND RECOMMENDATIONS

The objective of this dissertation was to study the use and characterization of metamaterials as narrow-band and broadband selective absorbers for opto-thermal and solar thermal energy conversion. A theoretical study of film-coupled gold nanowire narrow-band selective metamaterial absorbers was studied and their application in plasmonic localized heating was investigated. The film-coupled gold nanoparticles exhibited tunable selective absorption based on the size of the nanoparticles. Moreover, aluminum nanodisc narrow-band metamaterial absorbers were fabricated by using anodized aluminum oxide templates. A platform to measure the reflectance and transmittance of micro-scale samples was also developed and used to measure the reflectance of the aluminum nanodisc absorbers at the microscale (down to a 220 μm diameter area). Changing the height of the nanodiscs led to a shift in the resonance wavelengths of these metamaterial absorbers. Utilizing this shift of resonance can lead to their use as solar thermal absorbers. Next, the steady-state temperature of a lab-scale multilayer solar thermal absorber (metafilm) was measured. The experimental setup measures lab-scale solar absorbers for rapid comparison of their performance. Under a concentration factor of 20.3 suns, a steady-state temperature of ~500^{o}C was achieved for the metafilm compared to 375^{o}C for a commercial black absorber under the same conditions. Thermal durability testing showed the metafilm's ability to withstand up to 700^{o}C in vacuum conditions and up to 400^{o}C in ambient conditions. Moreover, a material cost analysis of the metafilm was conducted and it was found to cost significantly less ($2.22 per m^{2}) than commercial solar coatings ($5.41-100 per m^{2}). Recommendations to further this research will be discussed next and some preliminary results will be presented.

This consists of using the selective metafilms as absorbers and emitters and using the aluminum nanodiscs on glass as selective filters for photovoltaic cells to enhance solar thermophotovoltaic (STPV) energy conversion.

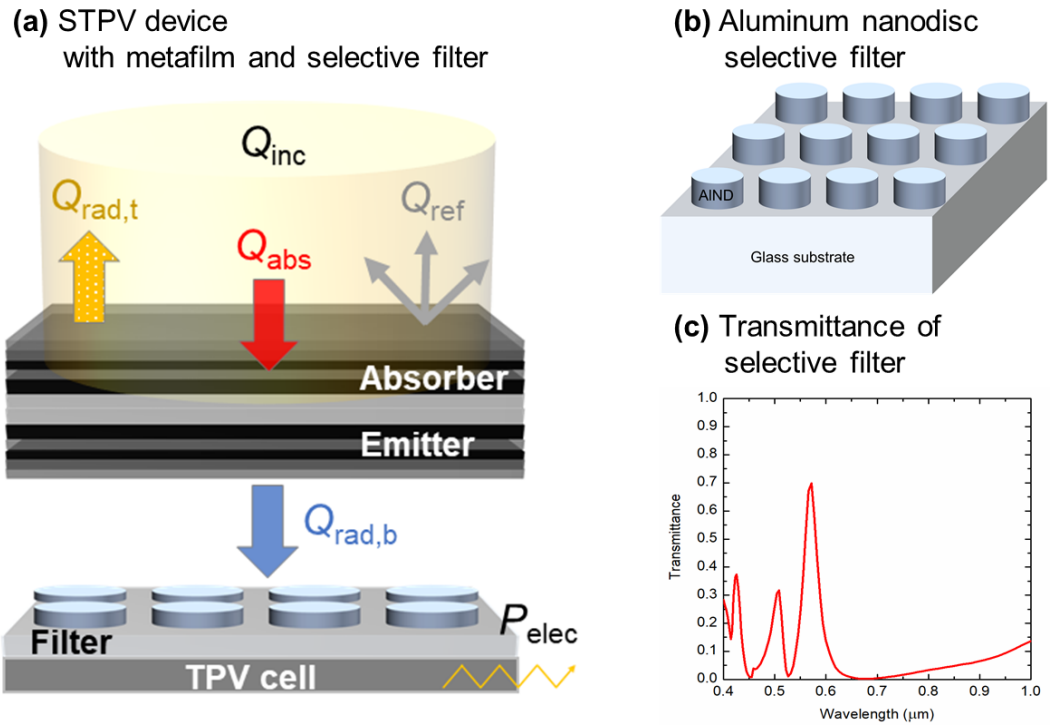

Figure 5.1. (a) Schematic of an STPV system with the metafilm as the absorber and emitter and an ideal optical filter. (b) Aluminum nanodisc selective filter. (c) Transmittance of the aluminum nanodisc selective filter.

Selective metamaterials can be employed as absorbers and emitters in STPV systems to significantly increase the conversion efficiency [85-87]. In an ideal STPV system, the incident solar energy is first absorbed by a surface that has near unity broadband solar absorptivity and near zero emissivity throughout the mid-infrared regime. The thermal energy absorbed by the absorber-emitter module is then emitted to the photovoltaic cell, as shown in Figure 5.1(a). To maximize the efficiency of the STPV system, an ideal emitter will have narrow-band emittance at the bandgap of the photovoltaic cell, thereby

minimizing losses due to mismatches between the cell bandgap and the energy of the photons being emitted. Using the fabricated metafilm as the absorber would lead to an increased temperature of the emitter. If the emitter is not designed to have a bandgap that matches the PV cell, a broadband emitter, such as the metafilm, can be used with a selective filter so that only energy that matches the PV cell would reach it. The AlNDs discussed in Chapter 3 can be fabricated on a glass substrate rather than an aluminum film. This would allow the AlNDs to be used as selective filters. A schematic of the AlND selective filter is shown in Figure 5.1(b). A preliminary simulation of such a filter was performed with 400 nm diameter and 50 nm thick AlNDs with a period of 450 nm and a glass substrate that is 200 nm thick. This resulted in a transmittance with multiple narrow-band peaks as shown in Figure 5.1Figure 5.1(c). By tuning the geometric parameters of the AlNDs of the structure, a selective filter that matches the narrow bandgap of a PV cell could be realized. This method of fabrication would be less expensive compared to buying commercial selective filters. Using the metafilm with the AlND selective filters would result in the enhancement of the energy conversion and efficiency of STPV systems. Equations (5.1 - 5.4) were used to find the STPV efficiency, η_{STPV}, of an STPV system using the metafilms as absorbers and emitters. When black absorbers and emitters were used and no selective filter was added to the system, η_{STPV} was 0.29% for an absorber temperature, T_a (= T_e, emitter temperature) of 588^{o}C. When the metafilm was used as the absorber and emitter and an ideal filter was used, η_{STPV} increased to 15.65% for a T_a (= T_e) of 1062^{o}C demonstrating the potential for further energy conversion enhancement if an AlND selective filter is used.

$$\eta_{\text{STPV}} = \eta_{\text{abs}} \eta_{\text{emit}} \eta_{\text{cell}} \tag{5.1}$$

$$\eta_{\text{abs}} = (Q_{\text{inc}} - Q_{\text{ref}} - Q_{\text{rad,losses}}) / Q_{\text{inc}} \tag{5.2}$$

$$\eta_{\text{emitter}} = \frac{Q_{\text{rad,b},E \geq E_g}}{Q_{\text{rad,b}} + Q_{\text{rad,losses}}} \tag{5.3}$$

$$\eta_{\text{cell}} = \frac{P_{\text{elec}}}{Q_{\text{rad,b},E \geq E_g}} \tag{5.4}$$

REFERENCES

[1] D. A. Baharoon, H. A. Rahman, W. Z. W. Omar, and S. O. Fadhl, "Historical development of concentrating solar power technologies to generate clean electricity efficiently – A review," *Renewable and Sustainable Energy Reviews,* vol. 41, pp. 996-1027, 2015/01/01/ 2015.

[2] C. K. Ho and B. D. Iverson, "Review of high-temperature central receiver designs for concentrating solar power," *Renewable and Sustainable Energy Reviews,* vol. 29, pp. 835-846, 2014/01/01/ 2014.

[3] M. Liu, N. H. Steven Tay, S. Bell, M. Belusko, R. Jacob, G. Will, *et al.*, "Review on concentrating solar power plants and new developments in high temperature thermal energy storage technologies," *Renewable and Sustainable Energy Reviews,* vol. 53, pp. 1411-1432, 2016/01/01/ 2016.

[4] H. L. Zhang, J. Baeyens, J. Degrève, and G. Cacères, "Concentrated solar power plants: Review and design methodology," *Renewable and Sustainable Energy Reviews,* vol. 22, pp. 466-481, 2013/06/01/ 2013.

[5] M. Persky, "Review of black surfaces for space-borne infrared systems," *Review of Scientific Instruments,* vol. 70, pp. 2193-2217, 1999.

[6] G. E. McDonald, "Spectral reflectance properties of black chrome for use as a solar selective coating," *Solar Energy,* vol. 17, pp. 119-122, 1975/05/01/ 1975.

[7] M. J. Persky and M. Szczesniak, "Infrared, spectral, directional-hemispherical reflectance of fused silica, Teflon polytetrafluoroethylene polymer, chrome oxide ceramic particle surface, Pyromark 2500 paint, Krylon 1602 paint, and Duraflect coating," *Applied optics,* vol. 47, pp. 1389-1396, 2008.

[8] K. Burlafinger, A. Vetter, and C. J. Brabec, "Maximizing concentrated solar power (CSP) plant overall efficiencies by using spectral selective absorbers at optimal operation temperatures," *Solar Energy,* vol. 120, pp. 428-438, 2015/10/01/ 2015.

[9] C. K. Ho, A. R. Mahoney, A. Ambrosini, M. Bencomo, A. Hall, and T. N. Lambert, "Characterization of Pyromark 2500 Paint for High-Temperature Solar Receivers," *Journal of Solar Energy Engineering,* vol. 136, pp. 014502-014502-4, 2013.

[10] D. Ding and W. Cai, "Self-assembled nanostructured composites for solar absorber," *Materials Letters,* vol. 93, pp. 269-271, 2013.

[11] A. Cuevas, L. Martínez, R. Romero, E. A. Dalchiele, R. Marotti, D. Leinen, *et al.*, "Electrochemically grown cobalt-alumina composite layer for solar thermal selective absorbers," *Solar Energy Materials and Solar Cells,* vol. 130, pp. 380-386, 2014/11/01/ 2014.

[12] A. Srinivasa Rao and S. Sakthivel, "A highly thermally stable Mn–Cu–Fe composite oxide based solar selective absorber layer with low thermal loss at high temperature," *Journal of Alloys and Compounds,* vol. 644, pp. 906-915, 2015/09/25/ 2015.

[13] F. Cao, L. Tang, Y. Li, A. P. Litvinchuk, J. Bao, and Z. Ren, "A high-temperature stable spectrally-selective solar absorber based on cermet of titanium nitride in SiO 2 deposited on lanthanum aluminate," *Solar Energy Materials and Solar Cells,* vol. 160, pp. 12-17, 2017.

[14] C. Wang, J. Shi, Z. Geng, and X. Ling, "Polychromic Al–AlN cermet solar absorber coating with high absorption efficiency and excellent durability," *Solar Energy Materials and Solar Cells,* vol. 144, pp. 14-22, 2016.

[15] Q. C. Zhang and D. R. Mills, "New cermet film structures with much improved selectivity for solar thermal applications," *Applied physics letters,* vol. 60, pp. 545-547, 1992.

[16] Q.-C. Zhang, K. Zhao, B.-C. Zhang, L.-F. Wang, Z.-L. Shen, Z.-J. Zhou, *et al.*, "New cermet solar coatings for solar thermal electricity applications," *Solar Energy,* vol. 64, pp. 109-114, 1998.

[17] F. Cao, D. Kraemer, T. Sun, Y. Lan, G. Chen, and Z. Ren, "Enhanced Thermal Stability of W-Ni-Al2O3 Cermet-Based Spectrally Selective Solar Absorbers with Tungsten Infrared Reflectors," *Advanced Energy Materials,* vol. 5, 2015.

[18] F. Cao, K. McEnaney, G. Chen, and Z. Ren, "A review of cermet-based spectrally selective solar absorbers," *Energy & Environmental Science,* vol. 7, pp. 1615-1627, 2014.

[19] B. J. Lee, Y.-B. Chen, S. Han, F.-C. Chiu, and H. J. Lee, "Wavelength-selective solar thermal absorber with two-dimensional nickel gratings," *Journal of Heat Transfer,* vol. 136, p. 072702, 2014.

[20] H. Sai, H. Yugami, Y. Kanamori, and K. Hane, "Solar selective absorbers based on two-dimensional W surface gratings with submicron periods for high-temperature photothermal conversion," *Solar energy materials and solar cells,* vol. 79, pp. 35-49, 2003.

[21] N. P. Sergeant, M. Agrawal, and P. Peumans, "High performance solar-selective absorbers using coated sub-wavelength gratings," *Optics express,* vol. 18, pp. 5525-5540, 2010.

[22] H. Wang and L. Wang, "Perfect selective metamaterial solar absorbers," *Opt Express,* vol. 21 Suppl 6, pp. A1078-93, Nov 4 2013.

[23] L. Wang and Z. Zhang, "Resonance transmission or absorption in deep gratings explained by magnetic polaritons," *Applied Physics Letters,* vol. 95, p. 111904, 2009.

[24] B. Zhao, L. Wang, Y. Shuai, and Z. M. Zhang, "Thermophotovoltaic emitters based on a two-dimensional grating/thin-film nanostructure," *International Journal of Heat and Mass Transfer,* vol. 67, pp. 637-645, 2013.

[25] N. Nguyen-Huu, M. Cada, and J. Pištora, "Investigation of optical absorptance of one-dimensionally periodic silicon gratings as solar absorbers for solar cells," *Optics Express,* vol. 22, pp. A68-A79, 2014/01/13 2014.

[26] H. Wang, K. O'Dea, and L. Wang, "Selective absorption of visible light in film-coupled nanoparticles by exciting magnetic resonance," *Optics letters*, vol. 39, pp. 1457-1460, 2014.

[27] M. Yan, J. Dai, and M. Qiu, "Lithography-free broadband visible light absorber based on a mono-layer of gold nanoparticles," *Journal of Optics*, vol. 16, p. 025002, 2014.

[28] K. Chi, L. Yang, Z. Liu, P. Gao, J. Ye, and S. He, "Large-scale nanostructured low-temperature solar selective absorber," *Optics letters*, vol. 42, pp. 1891-1894, 2017.

[29] K.-D. Song, T. J. Kempa, H.-G. Park, and S.-K. Kim, "Laterally assembled nanowires for ultrathin broadband solar absorbers," *Optics Express*, vol. 22, pp. A992-A1000, 2014/05/05 2014.

[30] L. Zhou, Y. Tan, D. Ji, B. Zhu, P. Zhang, J. Xu, *et al.*, "Self-assembly of highly efficient, broadband plasmonic absorbers for solar steam generation," *Science advances*, vol. 2, p. e1501227, 2016.

[31] I. Celanovic, N. Jovanovic, and J. Kassakian, "Two-dimensional tungsten photonic crystals as selective thermal emitters," *Applied Physics Letters*, vol. 92, p. 193101, 2008.

[32] V. Rinnerbauer, S. Ndao, Y. Xiang Yeng, J. J. Senkevich, K. F. Jensen, J. D. Joannopoulos, *et al.*, "Large-area fabrication of high aspect ratio tantalum photonic crystals for high-temperature selective emitters," *Journal of Vacuum Science & Technology B, Nanotechnology and Microelectronics: Materials, Processing, Measurement, and Phenomena*, vol. 31, p. 011802, 2013.

[33] G. Demésy and S. John, "Solar energy trapping with modulated silicon nanowire photonic crystals," *Journal of Applied Physics*, vol. 112, p. 074326, 2012.

[34] V. Rinnerbauer, Y. X. Yeng, W. R. Chan, J. J. Senkevich, J. D. Joannopoulos, M. Soljačić, *et al.*, "High-temperature stability and selective thermal emission of polycrystalline tantalum photonic crystals," *Optics express*, vol. 21, pp. 11482-11491, 2013.

[35] H. C. Barshilia, N. Selvakumar, K. Rajam, and A. Biswas, "Structure and optical properties of pulsed sputter deposited Cr x O y⁄ Cr⁄ Cr 2 O 3 solar selective coatings," *Journal of applied physics*, vol. 103, p. 023507, 2008.

[36] Z. Y. Nuru, C. Arendse, S. Khamlich, and M. Maaza, "Optimization of AlxOy/Pt/AlxOy multilayer spectrally selective coatings for solar–thermal applications," *Vacuum*, vol. 86, pp. 2129-2135, 2012.

[37] N. Selvakumar and H. C. Barshilia, "Review of physical vapor deposited (PVD) spectrally selective coatings for mid-and high-temperature solar thermal applications," *Solar Energy Materials and Solar Cells*, vol. 98, pp. 1-23, 2012.

[38] D. Hernández-Pinilla, A. Rodríguez-Palomo, L. Álvarez-Fraga, E. Céspedes, J. E. Prieto, A. Muñoz-Martín, *et al.*, "MoSi2–Si3N4 absorber for high temperature solar selective coating," *Solar Energy Materials and Solar Cells*, vol. 152, pp. 141-146, 2016/08/01/ 2016.

[39] F. Lenzmann, K. Li, A. Kitai, and H. Stover, "Thin-film micropatterning using polymer microspheres," *Chemistry of Materials*, vol. 6, pp. 156-159, 1994.

[40] N. Denkov, O. Velev, P. Kralchevski, I. Ivanov, H. Yoshimura, and K. Nagayama, "Mechanism of formation of two-dimensional crystals from latex particles on substrates," *Langmuir*, vol. 8, pp. 3183-3190, 1992.

[41] H. Deckman, J. Dunsmuir, S. Garoff, J. McHenry, and D. Peiffer, "Macromolecular self-organized assemblies," *Journal of Vacuum Science & Technology B*, vol. 6, pp. 333-336, 1988.

[42] Y. Xia, B. Gates, Y. Yin, and Y. Lu, "Monodispersed colloidal spheres: old materials with new applications," *Advanced Materials*, vol. 12, pp. 693-713, 2000.

[43] L. Wang, B. Lee, X. Wang, and Z. Zhang, "Spatial and temporal coherence of thermal radiation in asymmetric Fabry–Perot resonance cavities," *International Journal of Heat and Mass Transfer*, vol. 52, pp. 3024-3031, 2009.

[44] J. A. Duffie and W. A. Beckman, "Solar engineering of thermal processes," 1980.

[45] P. Kovacs, "Quality Assurance in Solar Heating and Cooling Technology: Report of project achievements," ed, 2012.

[46] P. Dupeyrat, C. Ménézo, M. Rommel, and H.-M. Henning, "Efficient single glazed flat plate photovoltaic–thermal hybrid collector for domestic hot water system," *Solar Energy*, vol. 85, pp. 1457-1468, 2011.

[47] S. Harrison and C. A. Cruickshank, "A review of strategies for the control of high temperature stagnation in solar collectors and systems," *Energy Procedia*, vol. 30, pp. 793-804, 2012.

[48] M. Köhl, M. Heck, S. Brunold, U. Frei, B. Carlsson, and K. Möller, "Advanced procedure for the assessment of the lifetime of solar absorber coatings," *Solar energy materials and solar cells*, vol. 84, pp. 275-289, 2004.

[49] H. Köhler, "On Abbe's theory of image formation in the microscope," *Journal of Modern Optics*, vol. 28, pp. 1691-1701, 1981.

[50] D. A. Boyd, L. Greengard, M. Brongersma, M. Y. El-Naggar, and D. G. Goodwin, "Plasmon-assisted chemical vapor deposition," *Nano letters*, vol. 6, pp. 2592-2597, 2006.

[51] X. Huang, P. K. Jain, I. H. El-Sayed, and M. A. El-Sayed, "Plasmonic photothermal therapy (PPTT) using gold nanoparticles," *Lasers in medical science*, vol. 23, pp. 217-228, 2008.

[52] S. Lal, S. E. Clare, and N. J. Halas, "Nanoshell-enabled photothermal cancer therapy: impending clinical impact," *Accounts of chemical research*, vol. 41, pp. 1842-1851, 2008.

[53] X. Huang, I. H. El-Sayed, W. Qian, and M. A. El-Sayed, "Cancer cell imaging and photothermal therapy in the near-infrared region by using gold nanorods," *Journal of the American Chemical Society*, vol. 128, pp. 2115-2120, 2006.

[54] M. H. Kryder, E. C. Gage, T. W. McDaniel, W. Challener, R. E. Rottmayer, G. Ju, *et al.*, "Heat assisted magnetic recording," *Proceedings of the IEEE,* vol. 96, pp. 1810-1835, 2008.

[55] R. E. Rottmayer, S. Batra, D. Buechel, W. Challener, J. Hohlfeld, Y. Kubota, *et al.*, "Heat-assisted magnetic recording," *Magnetics, IEEE Transactions on,* vol. 42, pp. 2417-2421, 2006.

[56] L. Cao, D. N. Barsic, A. R. Guichard, and M. L. Brongersma, "Plasmon-assisted local temperature control to pattern individual semiconductor nanowires and carbon nanotubes," *Nano letters,* vol. 7, pp. 3523-3527, 2007.

[57] G. A. Sotiriou, F. Starsich, A. Dasargyri, M. C. Wurnig, F. Krumeich, A. Boss, *et al.*, "Photothermal Killing of Cancer Cells by the Controlled Plasmonic Coupling of Silica-Coated Au/Fe2O3 Nanoaggregates," *Advanced Functional Materials,* vol. 24, pp. 2818-2827, 2014.

[58] W. Challener, C. Peng, A. Itagi, D. Karns, W. Peng, Y. Peng, *et al.*, "Heat-assisted magnetic recording by a near-field transducer with efficient optical energy transfer," *Nature photonics,* vol. 3, pp. 220-224, 2009.

[59] H. Wang and L. Wang, "Perfect selective metamaterial solar absorbers," *Optics express,* vol. 21, pp. A1078-A1093, 2013.

[60] H. Wang, V. P. Sivan, A. Mitchell, G. Rosengarten, P. Phelan, and L. Wang, "Highly efficient selective metamaterial absorber for high-temperature solar thermal energy harvesting," *Solar Energy Materials and Solar Cells,* vol. 137, pp. 235-242, 2015.

[61] J.-Y. Chang, H. Wang, and L. Wang, "Tungsten Nanowire Metamaterials as Selective Solar Thermal Absorbers by Excitation of Magnetic Polaritons," *Journal of Heat Transfer,* vol. 139, pp. 052401-052401-8, 2017.

[62] N. Liu, M. Mesch, T. Weiss, M. Hentschel, and H. Giessen, "Infrared perfect absorber and its application as plasmonic sensor," *Nano Lett,* vol. 10, pp. 2342-8, Jul 14 2010.

[63] B. Lee, L. Wang, and Z. Zhang, "Coherent thermal emission by excitation of magnetic polaritons between periodic strips and a metallic film," *Optics Express,* vol. 16, pp. 11328-11336, 2008.

[64] C.-J. Chen, J.-S. Chen, and Y.-B. Chen, "Optical responses from lossy metallic slit arrays under the excitation of a magnetic polariton," *JOSA B,* vol. 28, pp. 1798-1806, 2011.

[65] P. B. Johnson and R.-W. Christy, "Optical constants of the noble metals," *Physical Review B,* vol. 6, p. 4370, 1972.

[66] E. D. Palik, *Handbook of optical constants of solids* vol. 3: Academic press, 1998.

[67] J.-M. Cariou, J. Dugas, L. Martin, and P. Michel, "Refractive-index variations with temperature of PMMA and polycarbonate," *Applied optics,* vol. 25, pp. 334-336, 1986.

[68] Q. Li, W. Zhang, D. Zhao, and M. Qiu, "Photothermal enhancement in core-shell structured plasmonic nanoparticles," *Plasmonics*, vol. 9, pp. 623-630, 2014.

[69] L. Wang and Z. Zhang, "Wavelength-selective and diffuse emitter enhanced by magnetic polaritons for thermophotovoltaics," *Applied Physics Letters*, vol. 100, p. 063902, 2012.

[70] J. Zhou, E. N. Economon, T. Koschny, and C. M. Soukoulis, "Unifying approach to left-handed material design," *Optics letters*, vol. 31, pp. 3620-3622, 2006.

[71] J. A. Dean, "Lange's handbook of chemistry," 1985.

[72] R. Montgomery, "Viscosity and thermal conductivity of air and diffusivity of water vapor in air," *Journal of Meteorology*, vol. 4, pp. 193-196, 1947.

[73] D. G. Cahill and R. O. Pohl, "Thermal conductivity of amorphous solids above the plateau," *Physical review B*, vol. 35, p. 4067, 1987.

[74] Z. M. Zhang, *Nano/microscale heat transfer*, 2007.

[75] W. Lee and S.-J. Park, "Porous Anodic Aluminum Oxide: Anodization and Templated Synthesis of Functional Nanostructures," *Chemical Reviews*, vol. 114, pp. 7487-7556, 2014/08/13 2014.

[76] Y. Lei, W. Cai, and G. Wilde, "Highly ordered nanostructures with tunable size, shape and properties: A new way to surface nano-patterning using ultra-thin alumina masks," *Progress in Materials Science*, vol. 52, pp. 465-539, 2007/05/01/ 2007.

[77] Y. Lei and W.-K. Chim, "Shape and Size Control of Regularly Arrayed Nanodots Fabricated Using Ultrathin Alumina Masks," *Chemistry of Materials*, vol. 17, pp. 580-585, 2005/02/01 2005.

[78] G. Kenanakis, C. P. Mavidis, E. Vasilaki, N. Katsarakis, M. Kafesaki, E. Economou, *et al.*, "Perfect absorbers based on metal–insulator–metal structures in the visible region: a simple approach for practical applications," *Applied Physics A*, vol. 123, p. 77, 2017.

[79] Z. Zhang, Z. Yu, Y. Liang, and T. Xu, "Dual-band nearly perfect absorber at visible frequencies," *Optical Materials Express*, vol. 8, pp. 463-468, 2018/02/01 2018.

[80] *Ultra-Diffusive Light-Absorbing Foil UV, VIS and IR*. Available: http://www.acktar.com/category/products/lights-absorbing-foils/ultra-diffusive

[81] "ASTM G-173-03. Terrestrial Reference Spectra for Photovoltaic Performance Evaluation (American Society for Testing Materials (ASTM) International, West Conshohocken).".

[82] A. Stollo, T. Chiarappa, A. D'Angelo, A. Maccari, and F. Matino, "LCOE reduction for parabolic trough CSP: Innovative solar receiver with improved performance at medium temperature," in *AIP Conference Proceedings*, 2016, p. 030034.

[83] A. Boubault, C. K. Ho, A. Hall, T. N. Lambert, and A. Ambrosini, "Durability of solar absorber coatings and their cost-effectiveness," *Solar Energy Materials and Solar Cells,* vol. 166, pp. 176-184, 2017/07/01/ 2017.

[84] C. K. Ho and J. E. Pacheco, "Levelized Cost of Coating (LCOC) for selective absorber materials," *Solar Energy,* vol. 108, pp. 315-321, 2014/10/01/ 2014.

[85] S. Fan, "Photovoltaics: An alternative'Sun'for solar cells," *Nature nanotechnology,* vol. 9, pp. 92-93, 2014.

[86] N.-P. Harder and P. Würfel, "Theoretical limits of thermophotovoltaic solar energy conversion," *Semiconductor Science and Technology,* vol. 18, p. S151, 2003.

[87] A. Lenert, D. M. Bierman, Y. Nam, W. R. Chan, I. Celanović, M. Soljačić, *et al.*, "A nanophotonic solar thermophotovoltaic device," *Nature Nanotechnology,* vol. 9, p. 126, 01/19/online 2014.

APPENDIX A

LIST OF PUBLICATIONS

Journal Publications:

1. **Alshehri, H**., Ying, X., Wang, H., and Wang, L.P., 2016, "Plasmonic localized heating beyond the diffraction limit via magnetic polariton excitation," *Journal of Applied Physics*, 120(10), 103101.
2. **Alshehri, H**., Ni, Q., Wang, H., Taylor, S., and Wang, L.P., 2018, "Solar Thermal Characterization of a Multilayer Solar Thermal Absorber's (Metafilm) under Multiple Suns for Concentrating Solar Power Applications," to be submitted.
3. **Alshehri, H**., Taylor, S., Ni, Q., and Wang, L.P., 2018, "Characterization of Aluminum Nanodisc Metamaterials via a Microscale Optical Reflectance and Transmittance Microscope" to be submitted.
4. Yang, Y., Taylor, S., **Alshehri, H**., and Wang, L.P., 2017, "Wavelength-selective and diffuse infrared thermal emission mediated by magnetic polaritons from silicon carbide metasurfaces," *Applied Physics Letters*, 111(5), 051904.
5. Wang, H., **Alshehri, H**., Hang, S., and Wang, L.P., 2018, "Design, fabrication and optical characterizations of large-area lithography-free ultrathin multilayer selective solar coatings with excellent thermal stability in air," *Solar Energy Materials and Solar Cells*, 174C, 445-452.
6. Ni, Q., **Alshehri, H**., Yang, Y., Ye, H., and Wang, L.P., 2018, "Plasmonic light trapping for enhanced light absorption in film-coupled ultrathin metamaterial thermophotovoltaic cells," *Frontiers in Energy*, 12(1), 185-194.

Conference Presentations:

1. **Alshehri, H**., Wang, H., and Wang, L.P., 2015, "Plasmonic Local Heating beyond Diffraction Limit by the Excitation of Magnetic Polariton," *SPIE*. (Poster)
2. **Alshehri, H**., Ni, Q., Wang, H., Taylor, S., and Wang, L.P., 2017, "Optical and Thermal Characterizations of an Ultrathin Metafilm Selective Solar Thermal Absorber with Excellent High Temperature Stability," *MRS*. (Talk)

Projects	Publications
Plasmonic Localized Heating of Film-Coupled Gold Nanowires through Magnetic Polariton Excitation	**Alshehri** et al., *SPIE* (2015) **Alshehri** et al., *J. Appl. Phys.* (2016)
Characterization of Aluminum Nanodisc Metamaterials via a Microscale Optical Reflectance and Transmittance Microscope	Yang, Taylor, **Alshehri**, and Wang *Appl. Phys. Lett.* (2017) **Alshehri** et al., to be submitted, (2018)
Solar Thermal Characterization of a Multilayer Solar Thermal Absorber's (Metafilm) under Multiple Suns for Concentrating Solar Power Applications	Wang, **Alshehri**, Hang, and Wang *Sol. Energ. Mat. Cells*, (2018) **Alshehri** et al., to be submitted, (2018)

APPENDIX B

SEM IMAGES OF ALUMINUM NANODISC ABSORBERS

50 nm AlND on Al (Sample 1)

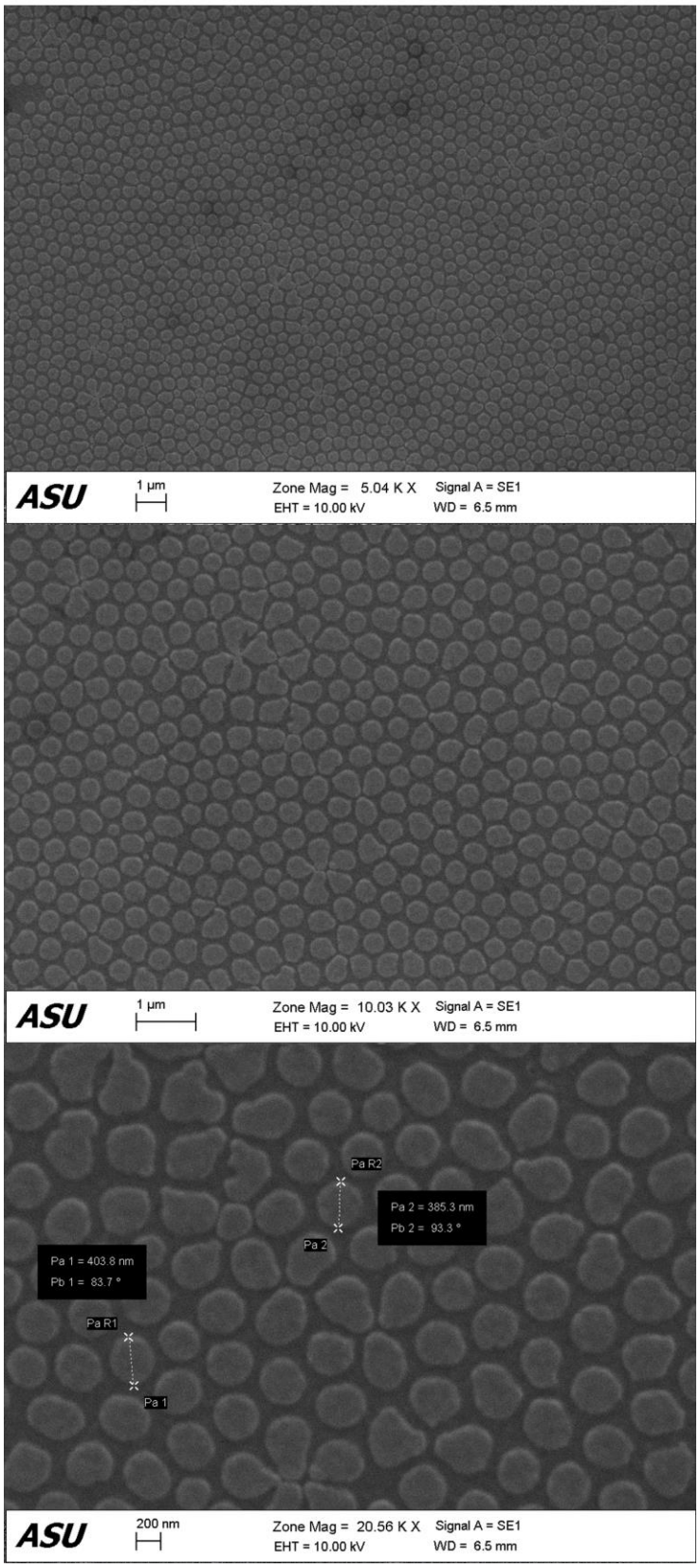

50 nm AlND on Al (Sample 2)

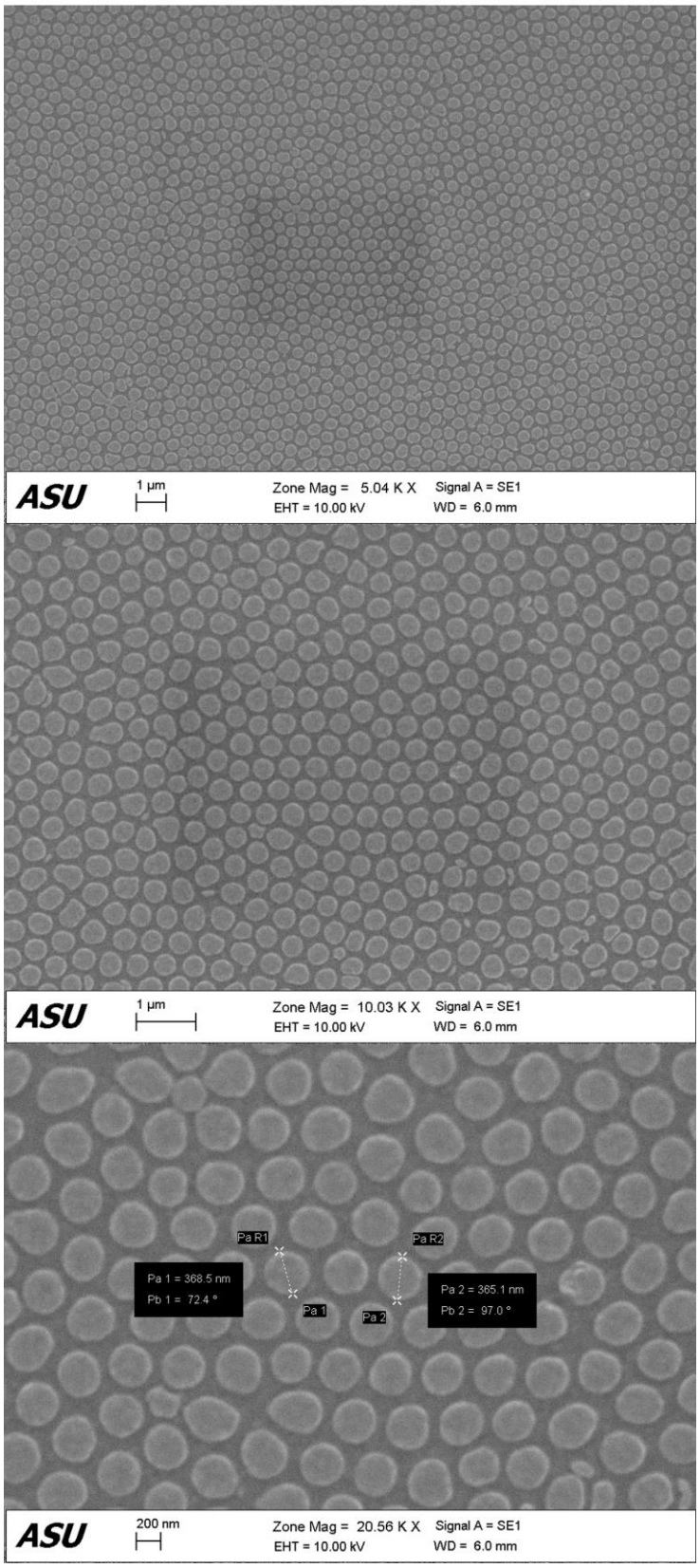

87 nm AlND on Al

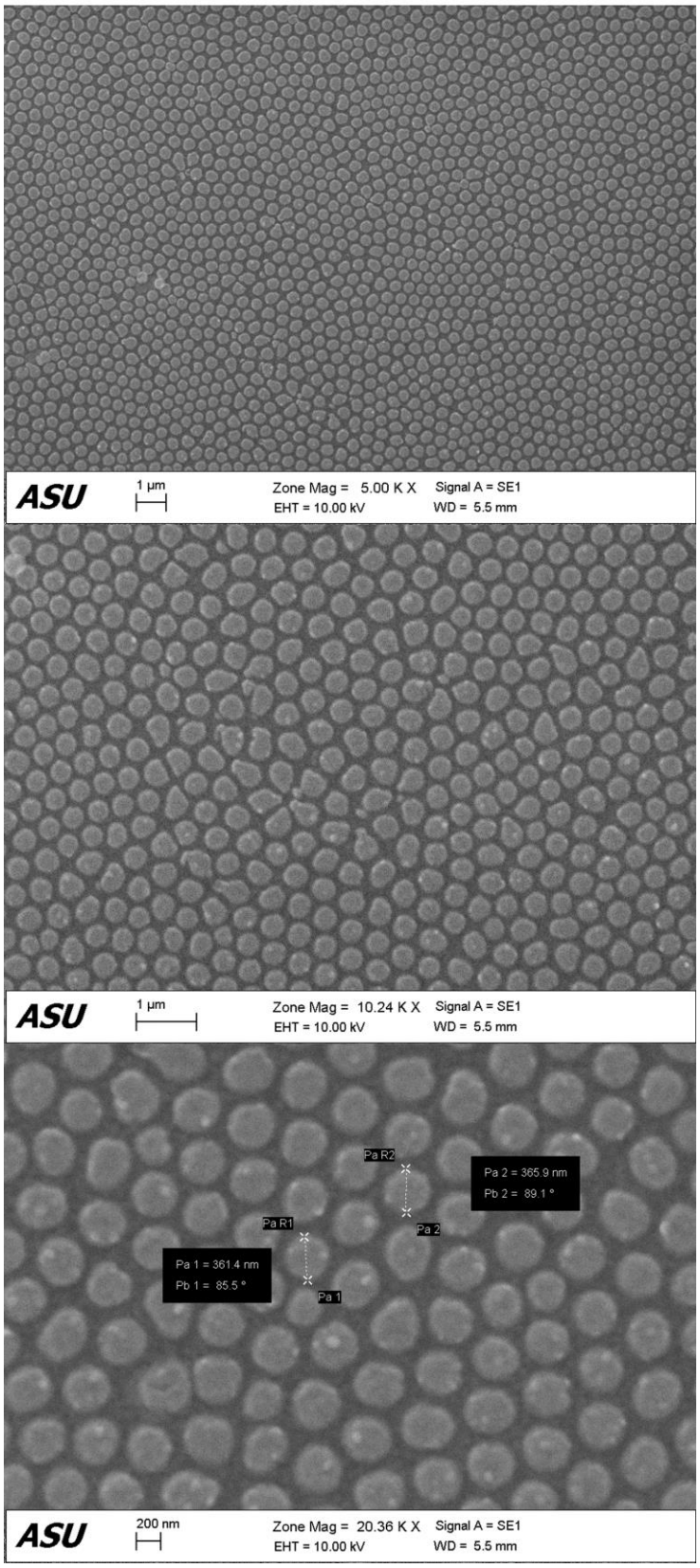

130 nm AlND on Al

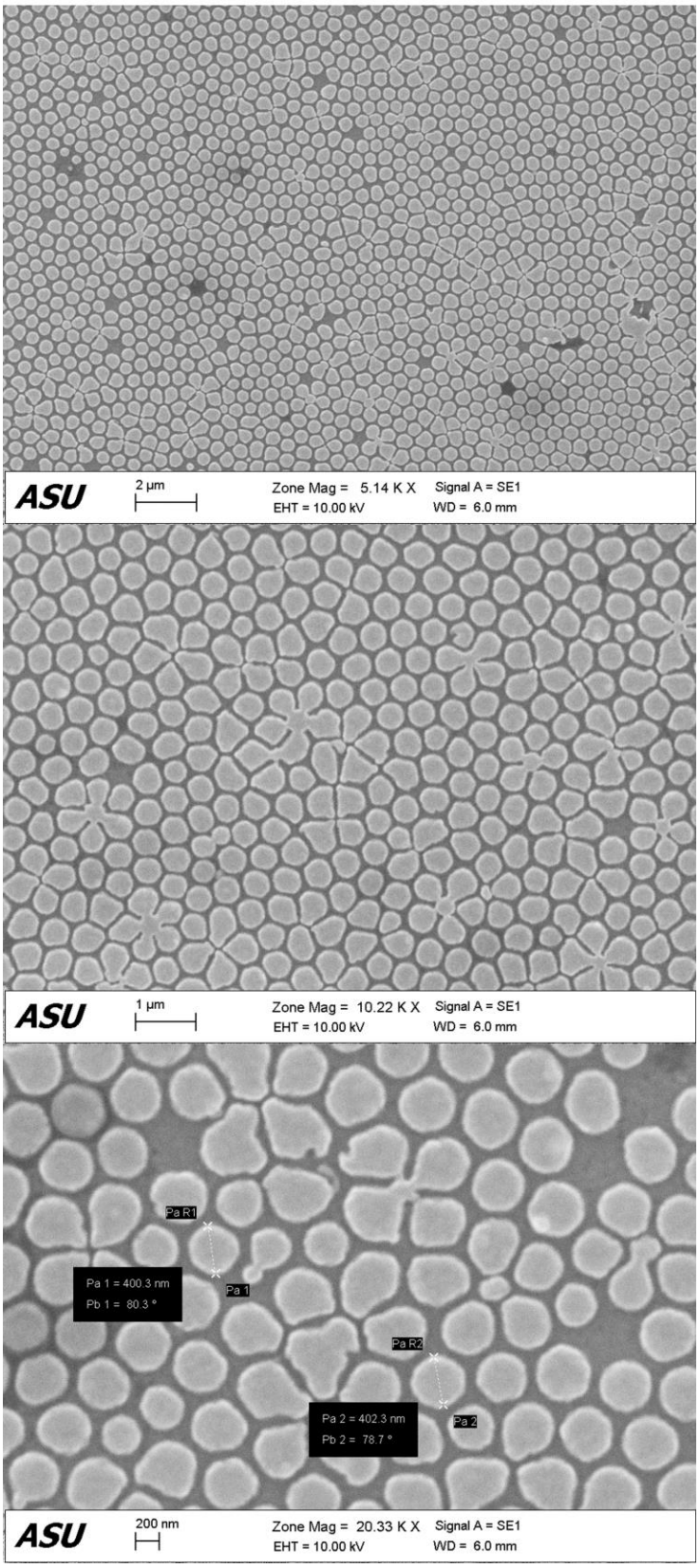

50 nm AlND on 100 nm SiO2 on Al (Sample 1)

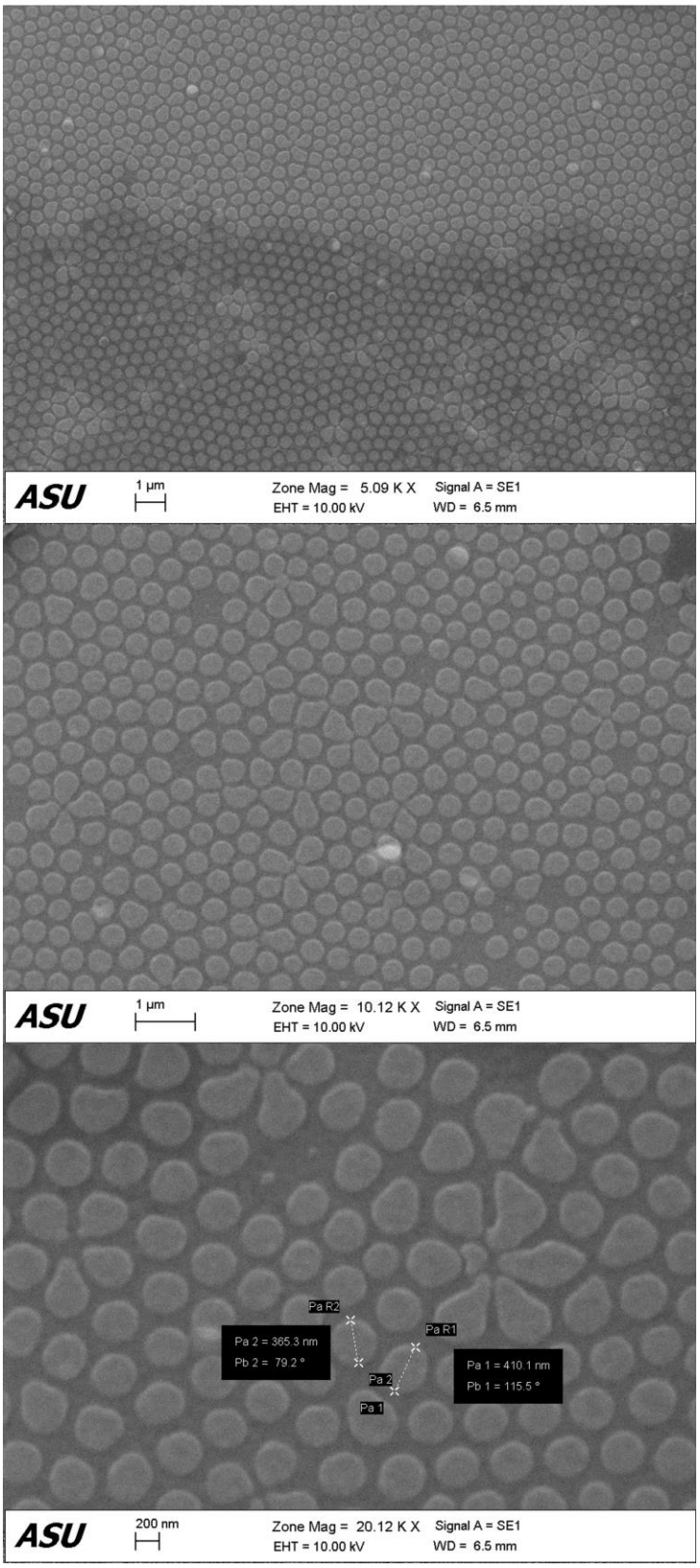

50 nm AlND on 100 nm SiO2 on Al (Sample 2)

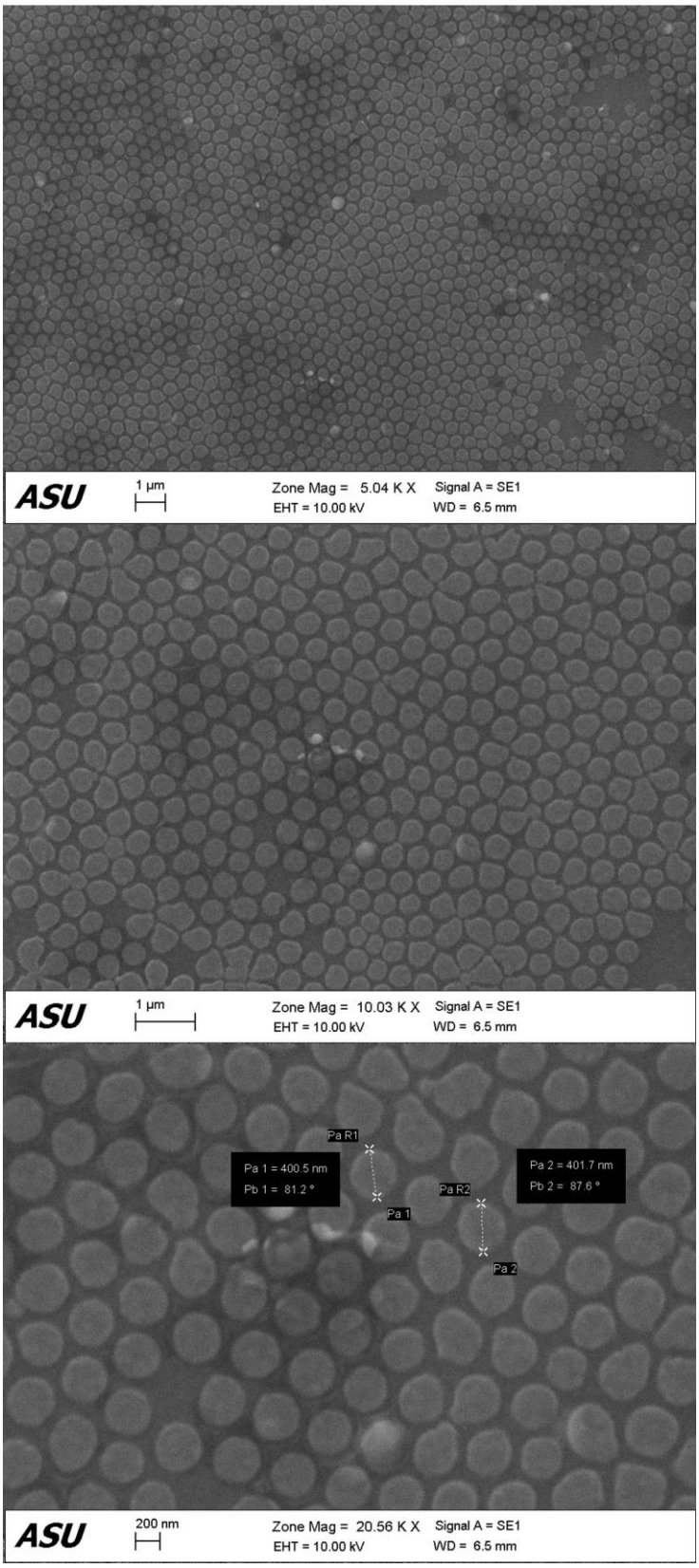

APPENDIX C

AFM RESULTS OF ALUMINUM NANODISC ABSORBERS

50 nm AlND on Al (sample 1, location 1):

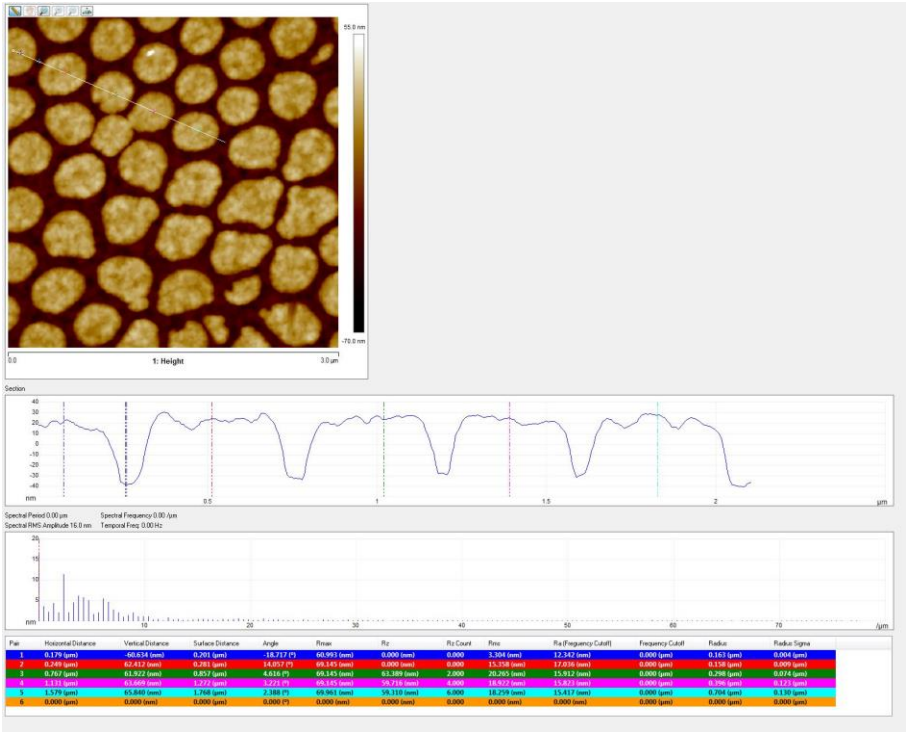

50 nm AlND on Al (sample 1, location 2):

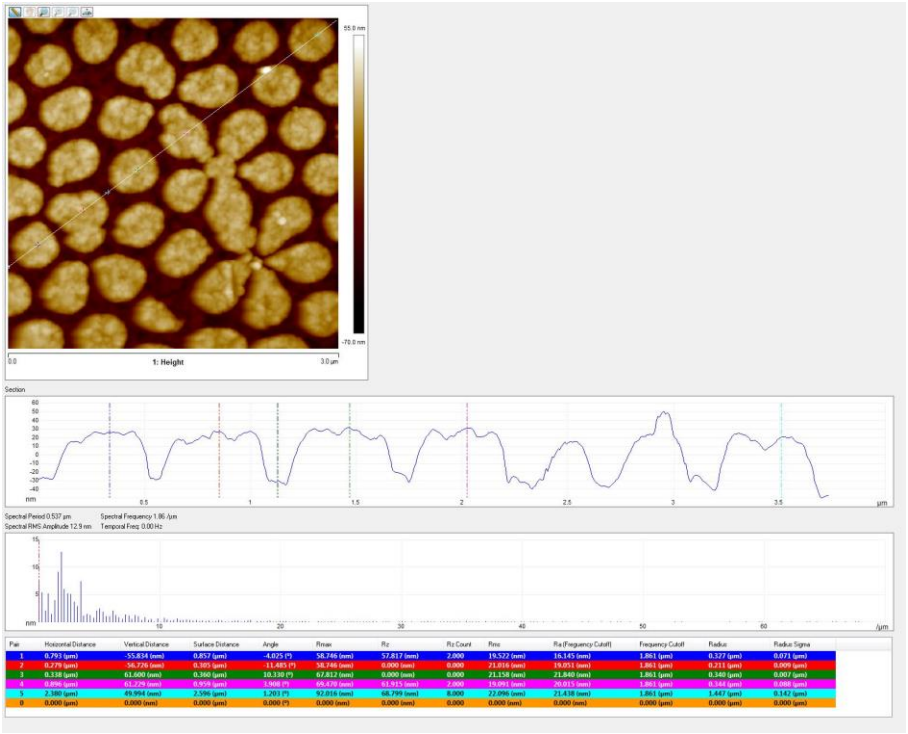

50 nm AlND on Al (sample 2, location 1):

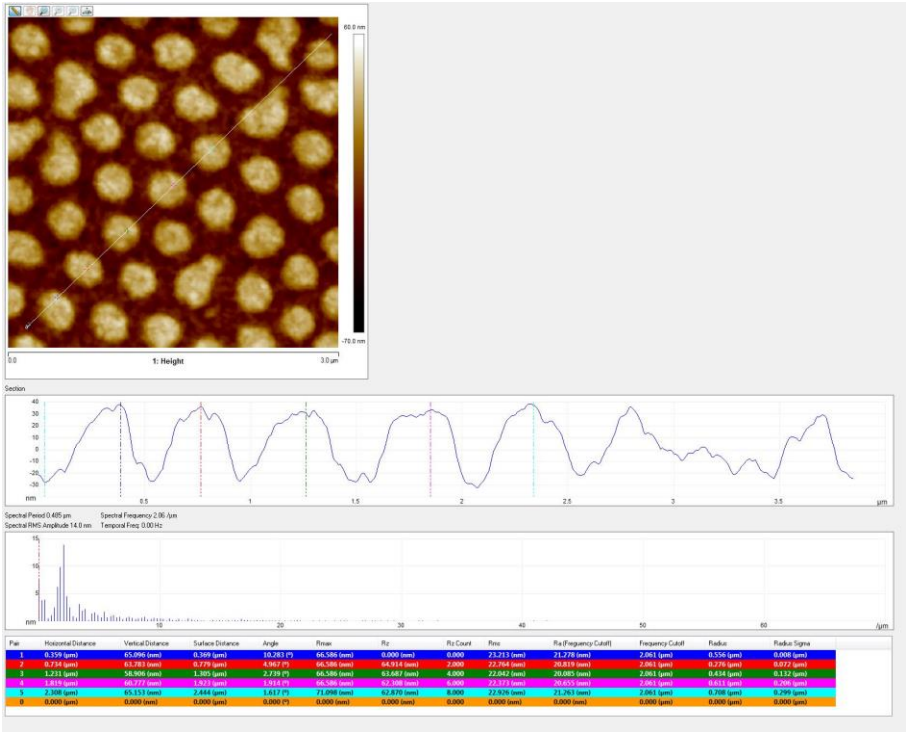

50 nm AlND on Al (sample 2, location 2):

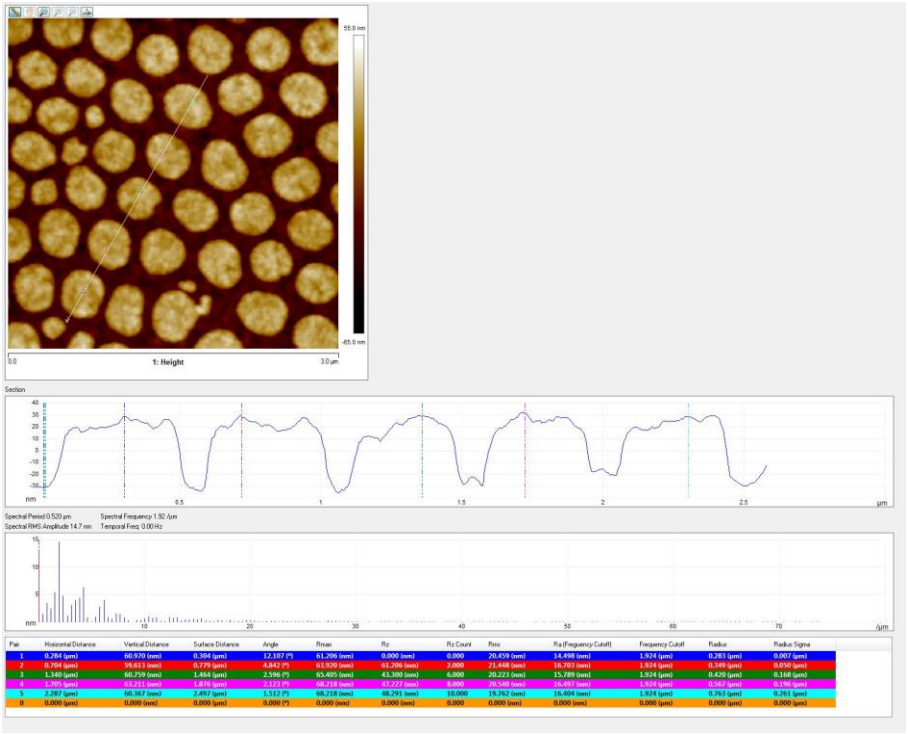

87 nm AlND on Al (location 1):

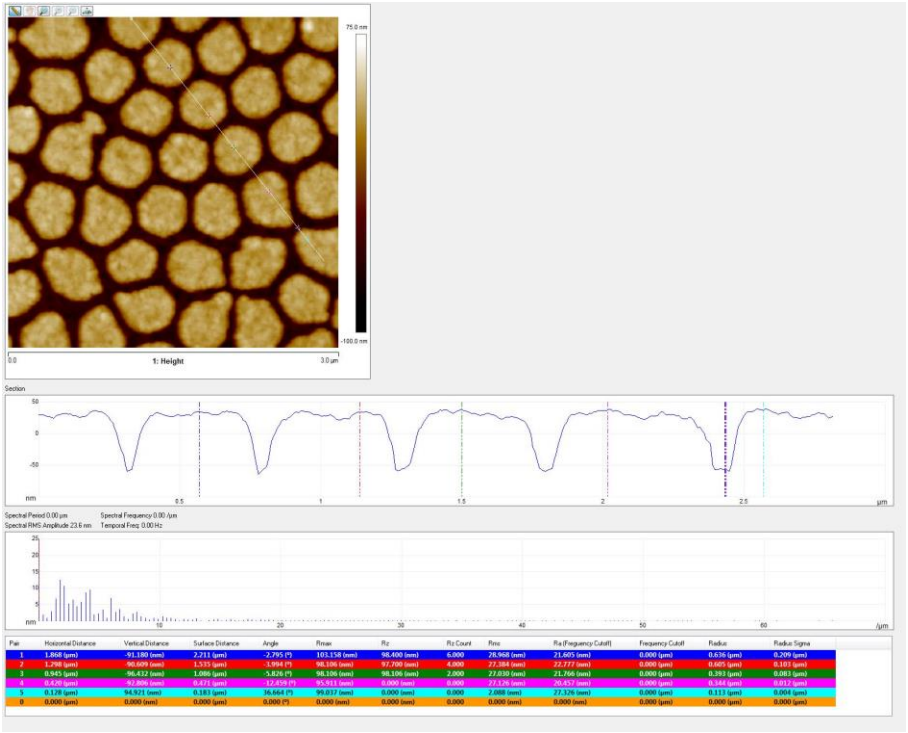

87 nm AlND on Al (location 2):

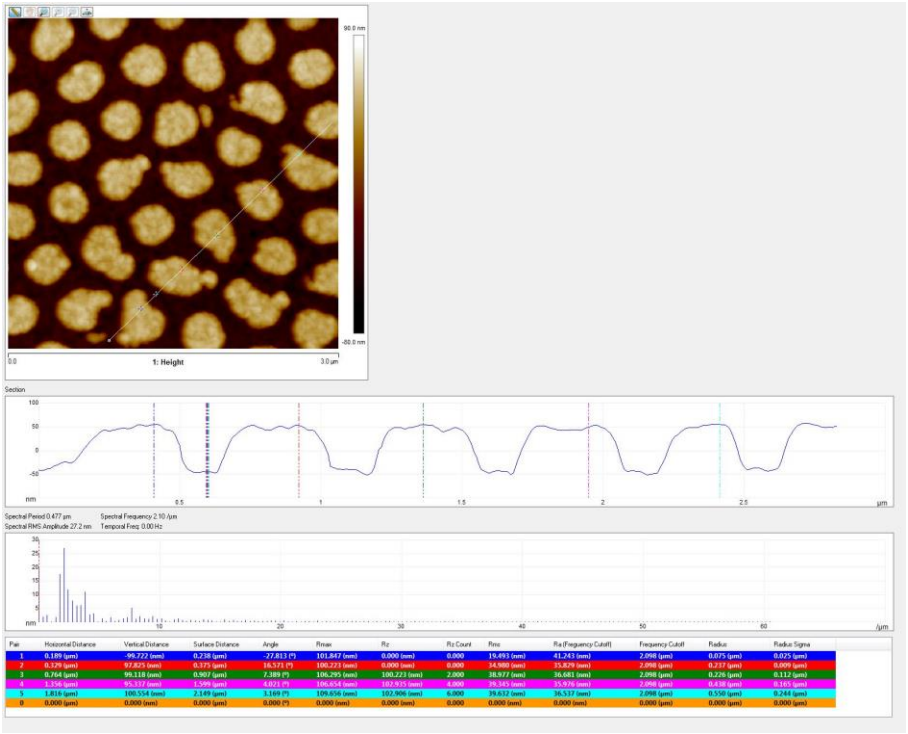

130 nm AlND on Al (location 1):

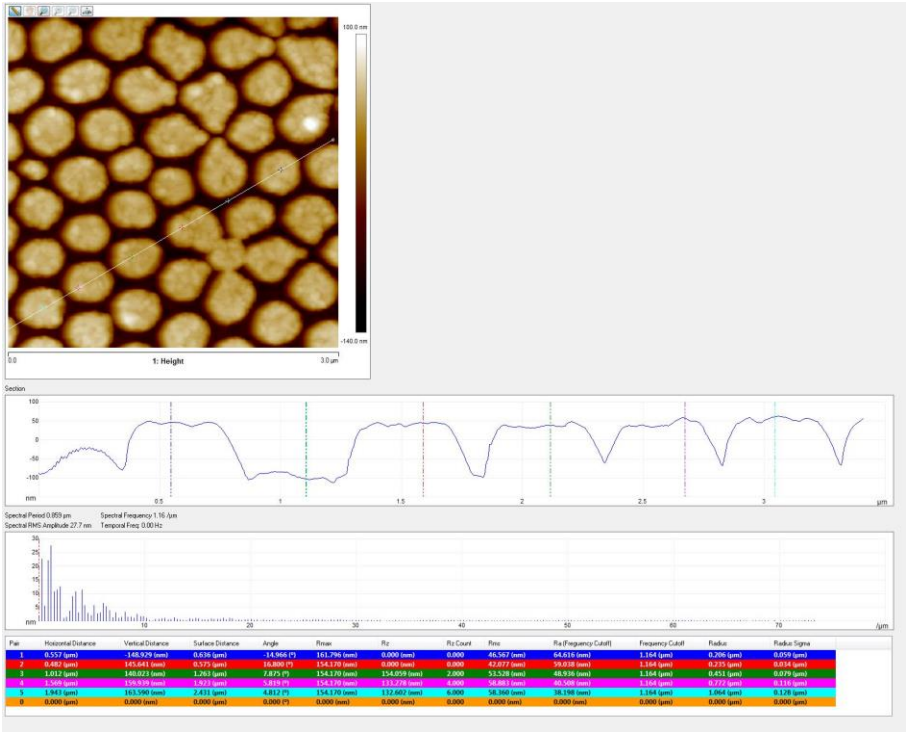

130 nm AlND on Al (location 2):

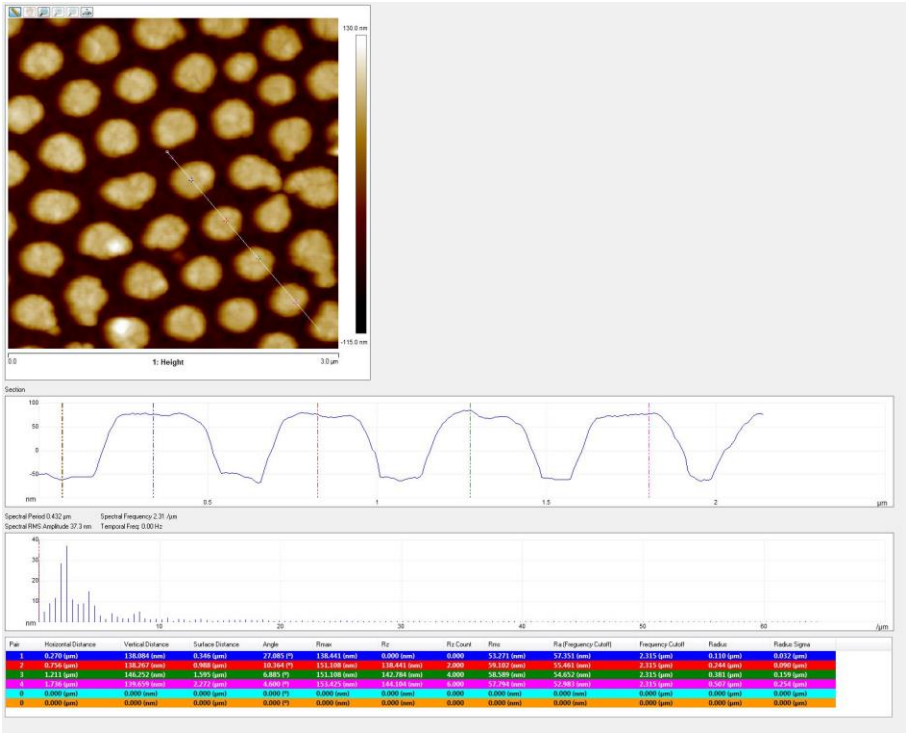

50 nm AlND on 100 nm SiO2 on Al (sample 1, location 1):

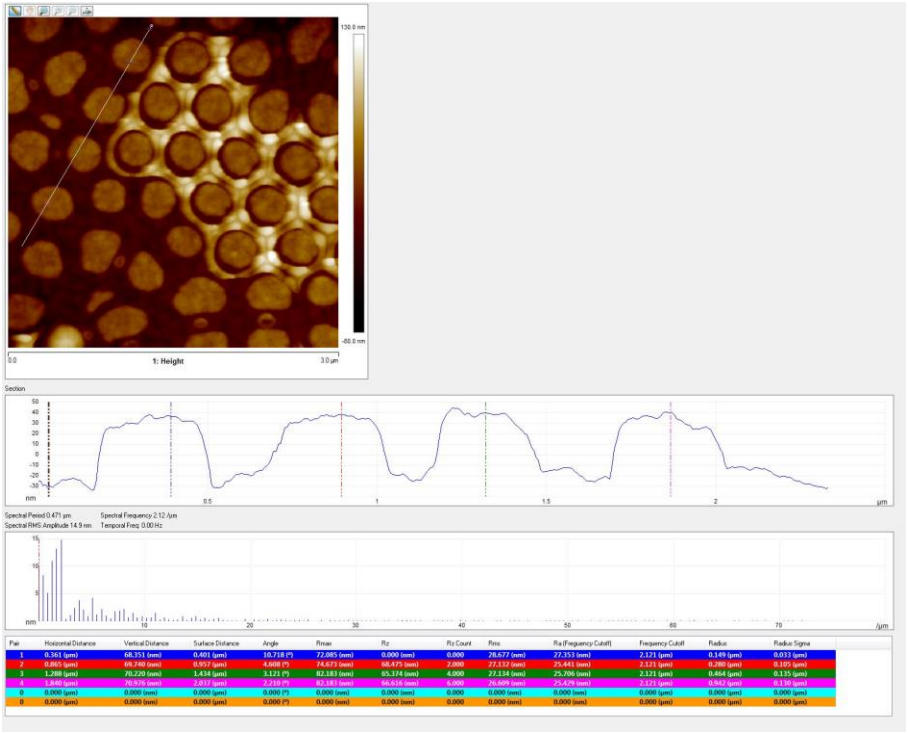

50 nm AlND on 100 nm SiO2 on Al (sample 1, location 2):

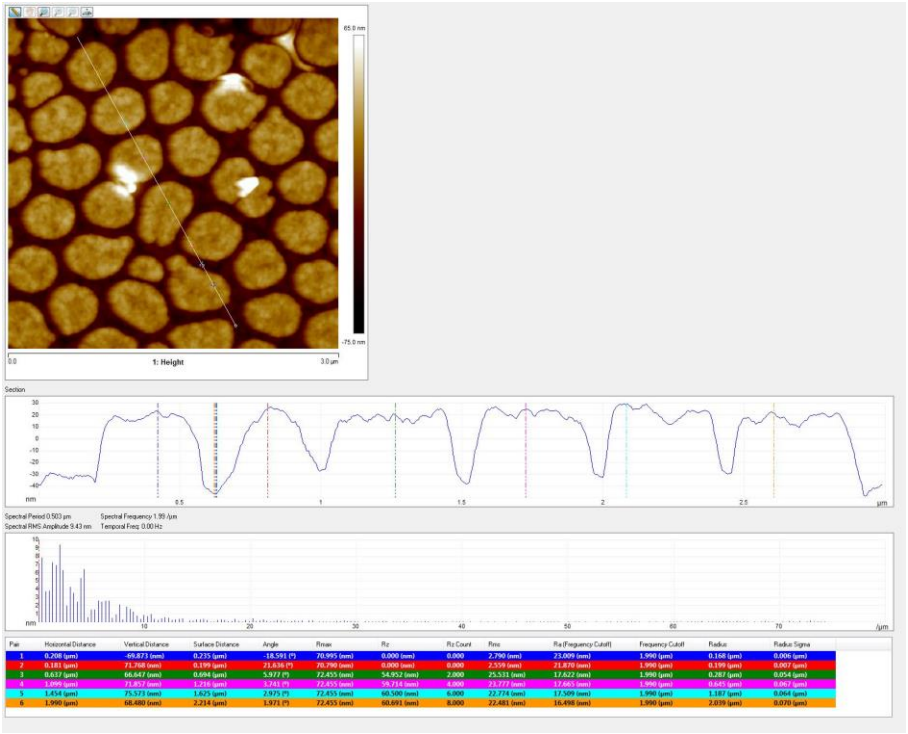

50 nm AlND on 100 nm SiO2 on Al (sample 2, location 1):

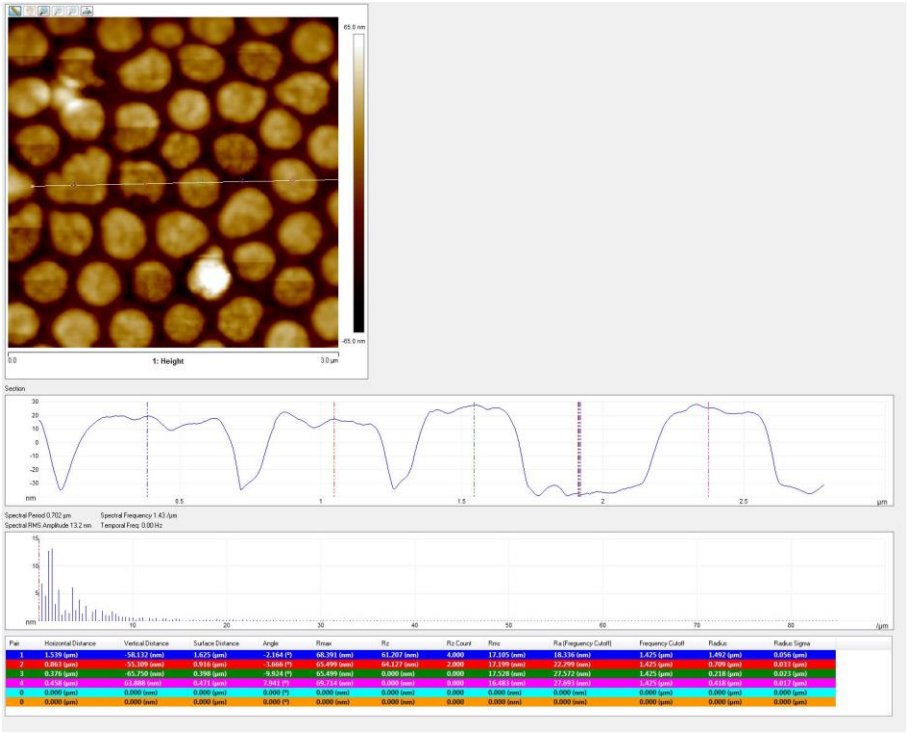

50 nm AlND on 100 nm SiO2 on Al (sample 2, location 2):